# On the Origin of Photons: Understanding Excitons and Multiexcitons in Colloidal Semiconductor Nanocrystals

by

Thomas Stanley Bischof

Submitted to the Department of Chemistry
in partial fulfillment of the requirements for the degree of

Doctor of Philosophy in Chemistry

at the

MASSACHUSETTS INSTITUTE OF TECHNOLOGY

September 2015



Author .....
Department of Chemistry
July 24, 2015

Certified by .....
Moungi G. Bawendi
Lester Wolfe Professor of Chemistry
Thesis Supervisor

Accepted by .....
Robert W. Field
Chairman, Department Committee on Graduate Students

This doctoral thesis has been examined by a Committee of the Department of Chemistry as follows:

Professor Keith A. Nelson .....
Thesis Committee Chairman
Haslam and Dewey Professor of Chemistry

Professor Moungi G. Bawendi .....
Thesis Supervisor
Lester Wolfe Professor of Chemistry

Professor Gabriela Schlau-Cohen .....
Thesis Committee Member
Assistant Professor of Chemistry

# On the Origin of Photons: Understanding Excitons and Multiexcitons in Colloidal Semiconductor Nanocrystals

by

Thomas Stanley Bischof

Submitted to the Department of Chemistry
on July 24, 2015, in partial fulfillment of the
requirements for the degree of
Doctor of Philosophy in Chemistry

## Abstract

This thesis focuses on studies of exciton and multiexciton dynamics in colloidal semiconductor nanocrystals. I concentrated primarily on the development of correlation spectroscopies for the measurement of the statistics and dynamics of multiexciton emission.

Under most conditions, the emission properties of nanocrystals are dominated by the photophysics of the single-exciton state. However, due to high density of states nanocrystals can readily undergo several successive excitations, leading to multiexcitonic states with distinct dynamics. As nanocrystals are more frequently used under conditions of high excitation flux for light-emitting applications, the often destructive nature of multiexcitons are increasingly relevant. Prior work on multiexcitons has largely focused on the biexciton, and here we develop tools to directly study triexciton emission.

First, we develop the theoretical and analytical apparatus for studying multiexciton emission. The model and software are general to arbitrary numbers of excitons and provide the framework for further correlation-based methods. The software is general and may be used in any photon-timing application.

InAs is a promising candidate material as an infrared emitter for down-shifting and biological applications. In one study, we characterize the excitonic dynamics of individual InAs nanocrystals. We find that the nanocrystals qualitatively behave like CdSe nanocrystals, in that they exhibit blinking, monoexponential radiative dynamics, and (generally) low biexciton quantum yield. In a separate set of experiments, we study the temperature-dependent exciton emission dynamics of InAs quantum dots and find that their emission is well-described by existing excitonic fine-structure models.

CdSe is the classical colloidal quantum dot material, and is the ideal testing ground for methods development. We apply new high-order correlation methods to study the emission statistics and dynamics of the triexciton, biexciton, and monoexciton

at the single-molecule level. We find that multiexcitonic states have no memory: the relaxation of a biexciton yields a monoexciton which behaves identically to one formed by a single-photon excitation. We discuss a few examples of materials which may exhibit exotic biexcitonic states.

Next, we explore the use of infrared-emitting nanocrystals for deep-tissue imaging in biological research. Earlier work on the subject involved the use of emitters with significantly lower quantum yield, and we demonstrated a variety of applications which make use of the high quantum yield and chemical functionality of colloidal nanocrystals. We used the unique combination of chemical functionality and high emission quantum yield to perform studies in mice: non-invasive measurement of vital signs in awake mice; real-time metabolic imaging of lipoproteins in an intact mouse; vascular imaging and blood velocimetry in a mouse with a cranial window model.

Finally we discuss a few project ideas which arose during the work on this thesis, but were not successfully completed.

Thesis Supervisor: Moungi G. Bawendi
Title: Lester Wolfe Professor of Chemistry

# Acknowledgments

The work in this thesis ended up being the culmination of many collaborations and discussions with an astounding variety of wonderful people.

Andrew! You have been my closest friend and collaborator through all of these years, and I am incredibly sad that we will not be working and living together any more.

I would like to thank Andrew Beyler, Phill Milner, and Sam Teitelbaum for being faithful roommates for the past four years, and for the great times we have had together.

The spectroscopy subgroup is a wonderful close-knit group of people, and I am glad to have worked with you all: Andrew Beyler, Justin Caram, Igor Coropceanu, Raoul Correa, Jian Cui, Leigh Heathcote, Russ Jensen, Sophie Betram, Katie Shulenberger, Dave Strasfeld, Hendrik Utzat, Mark Wilson, and Jing Zhao. Our weekly meetings, regular discussions, and collaborative research have enriched my scientific life.

Andrew Beyler, Jian Cui, and Mark Wilson: writing that review paper was a great experience, even if we did have to lock ourselves in a room for a week to get it done.

To my many collaborators in the group, thank you for providing me with numerous samples of all shapes and sizes! Dan Harris, I am particularly glad to have worked with you, and appreciate your perspective on the scientific process.

Oliver Bruns, thank you for teaching me much of what I know about biology. The infrared imaging project has broadened my perspective dramatically, and I am excited to see where things go from here.

My time at Lincoln Laboratory was some of the best-spent of my research. In particular the Integrated Photonics Initiative (IPI)/Integrated Quantum Initiative (IQI) has been an extremely valuable opportunity to learn about photonics, optical communications, quantum information, and a variety of other topics which I would otherwise never had cause to explore. I am grateful to Group 67 for hosting me for five years, and to the folks who helped run the SNSPDs: Raoul Correa, Eric Dauler, Ben Dixon, Matt Grein, Jamie Kerman, Ryan Murphy, Athena Pan, Danna Rosenberg, and Greg Steinbrecher. Our many hours working together have been extremely enjoyable, and I will miss you all.

I am eternally grateful for the guidance I received as an undergraduate from the members of the Alivisatos group at U.C. Berkeley. Gordana Dukovic, Trevor Ewers, Prashant Jain, Jon Owen, and everyone else, I would not be where I am today without your help.

The MIT sailing pavilion is host to a wonderful group of people, and one of the greatest assets at MIT. My many hours spent out on the Charles have been a great escape from the stresses of everyday life, and the trips out to Boston harbor have been some of the most exciting and enlightening experiences of my life. Bill, Stew, Gerard, Wally, and everyone else, thanks for everything, in particular for always erring on the side of permissiveness. I did plenty of stupid things when I was learning (and sometimes still do), but without those mistakes I would not have learned as quickly

or to the same depth.

Thanks to my family for their support all these years. Mom, Dad, Vicky, and everyone else, thanks for providing a solid foundation for my life.

Finally, thank you Moungi for providing the resources to enable me to pursue my ideas. The unique combination of resources, people, and research projects you have cultivated gives us the opportunity to study an incredibly diverse assortment of topics, and much of the most interesting work in our group has arisen from our strong collaborative culture. Your commitment to quality and willingness to see things through is unparalleled and invaluable, and I am glad to have been able to spend these years working with you.

# Contents

# List of Figures

# List of Tables

# Listings

# Chapter 1

# Introduction

Colloidal semicondutor nanocrystals are, as the name would suggest, crystalline particles composed of semiconducting materials with length scales on the order of nanometers. For many semiconducting materials these dimensions are on the order of the exciton Bohr radius, such that the excited electronic state is spatially confined. This confinement effect gives rise to size-dependent optical properties, which are often visualized as the change in the visible absorption and emission spectrum for CdSe.[1] This effect is not limited to visible-emitting materials, an in fact a whole variety of semiconducting materials have been used to make nanocrystals with optical features in the ultraviolet, visible, near-infrared, shortwave infrared, and mid infrared.[2,3]

In addition to classical semiconducting materials, a variety of materials which are metallic in their bulk form can be induced to emit light. For example, small clusters of a few gold and silver atoms show a "confinement" effect,[4–11] though at this scale the confinement is more akin to the particle-in-a-box description of a polyene such as $\beta$-carotene than to a classical semiconductor. This highlights some of the difficulty in understanding these nanoscale materials: while it is useful to consider only the core of the nanocrystal when describing optical properties, the surface ligands are an essential part of the particle. Without proper ligation[12,13] or surface termination by an epitaxial shell[14] nanoparticles do not emit light efficiently. Yet despite the incredible importance of the nanocrystal surface, as a field we do not yet have a complete vocabulary and associated experimental tools for understanding this chemistry, though

many great strides have been made to understand the reactivity and stoichiometry of the nanocrystal surface.[12,13,15–22]

This suite of materials are generally produced through a hot-injection colloidal synthesis, in which a hot solvent solution is prepared with some precursors, and the remaining precursors are injected rapidly to supersaturate the solution, which gives rise to a narrow distribution of nanocrystal size. The kinetics of the process were originally described for the formation of sulfurous colloids,[23,24] and this model has proven descriptive for a variety of material systems where some monomeric species is stable. For more reactive species the model is not as descriptive,[25,26] which has caused considerable synthetic challenges.

An astounding variety of nanoscale materials can be formed through chemical methods.[27–33] These synthetic possibilities are themselves a fascinating avenue of inquiry, but in this thesis we will focus primarily on the optical phenomena of light-emitting nanocrystals.

## 1.1 Optical Phenemona of Colloidal Semiconductor Nanocrystals

Nanaocrystals exhibit a variety of phenomena which manifest in various ways at the ensemble and single-molecule level, including: intensity blinking,[34–45] lifetime blinking,[41,42,46–50] spectral diffusion,[51] multiexcitons,[45,52–55] photothermal recovery[56–581], and excitonic fine strcture.[53,59–62] All of these effects give rise to some changes in the emission lifetime, quantum yield, and spectrum, and ultimately our goal as single-molecule spectroscopists is to design experiments which correctly control for the parameters of interest. Jian Cui, Andrew Beyler, Mark Wilson and I wrote a review of these ideas as they manifest in single-molecule emission spectroscopy,[63] and I suggest that the interested reader read that review for further information.

Even though the field of single-molecule emission spectroscopy is relatively ma-

[1]This phenomenon is extremely baffling: what photochemical process occurs on the timescale of minutes, happens instantly, and can take hours to reverse?

ture, we have hardly begun to understand how these optical phenonema affect the absorptivity of nanocrystals. This is primarily a result of the technical difficulty of such studies, though a few key results have been obtained.[64–68]

## 1.2 Overview of this Thesis

In this thesis, we discuss several investigations of the photoluminescence properties of various colloidal semiconductor nanocrystal materials. The chapters are roughly divided into three meta-sections: methods and theory (Chapters 2 and 3), development and application of single-molecule spectroscopies (Chapters 4 to 6), and applications of nanocrystals for biology (Chapter 7).

First, we discuss the details of developing photophysical theories (Chapter 2) and of working with photon arrival time data (Chapter 3). These are perhaps the most useful chapters for a first-year student or someone else interested in performing optical studies of nanocrystals. These may be safely skipped by a reader who is primarily interested in the experimental results, as the relevant ideas are reiterated where necessary.

After establishing the methods, we discuss two studies on the photophysics of InAs (Chapters 4 and 5). In the first study, we explore the emission dynamics of individual nanocrystals at room temperature and find that their behavior is largely similar to that found for CdSe nanocrystals: the nanocrystals blink, have distinct emission lifetimes, and have various biexciton quantum yields. In the latter study, we examine the time-resolved emission from an ensemble of InAs nanocrystals at various temperatures, and find that their emission dynamics may be described well by a two-state band-edge excitonic model.

Next, we discuss a study of high-order multiexcitons in CdSe nanocrystals (Chapter 6). We develop and use high-order correlation spectroscopies to distinctly isolate the emission of the triexciton, biexciton, and monoexciton. For the first time, we measure the quantum yield of the triexciton of CdSe quantum dots.

In a change of pace, we next discuss a series of studies on the use of infared-

emitting nanocrystals as labels for deep-tissue biological imaging (Chapter 7). We describe a few proof-of-concept studies which demonstrate the unique capabilities of nanocrystals as biological labels, particularly their high quantum yield and chemical functionality.

Lastly, we discuss a few potential studies of interest (Chapter 8). These ideas are most likely entirely feasible and follow directly from the work described in the rest of this thesis, but have not yet been experimentally realized.

# Chapter 2

# Modeling the Photoluminescence of Nanocrystals

As spectroscopists, we study the interaction of light with matter in order to develop an understanding of the physics which gives rise to such interactions. Colloidal semiconductor nanocrystals in particular exhibit a variety of optical phenomena, including photoluminescence intermittency (blinking), emission lifetime fluctuations, multiexciton emission and multiexciton generation (a.k.a. exciton fission, quantum cutting, etc.). Over the years various tools have been developed to understand how particular physics manifests in a particular experiment.[63]

In this chapter we discuss some of the fundamental ideas governing the statistics and dynamics of nanocrystal emission, and how these behaviors manifest experimentally. We describe methods for modeling Poissonian and non-Poissonian emitters. Finally, we develop an analytical model for $g^{(n)}$, including the effects of multiexciton excitation and emission, experimental losses, and imperfect photon number resolution.

## 2.1 Poissonian Emission

Before discussing nanocrystal physics, it is necessary to develop some vocabulary and intuition for thinking about the relationship between an ensemble of emitters and

the individual emitters themselves. We will begin by thinking about the classical depiction of signals as real-valued intensities and transition to thinking in terms of the individual emission events of which these actually-discrete signals are composed.

Consider a laser. In such a device, a lasing medium is prepared a state conducive to stimulated emission, the process in which a single photon interacts with an excited state of matter to produce a second identical photon. The lasing cavity is designed to provide a path for light to reflect repeatedly through the lasing medium, such that any spontaneous or stimulated emission along this path has the opportunity to interact with the lasing medium and produce more stimulated emission. An outcoupling device at one end of the cavity enables the extraction of some fraction of the photons produced – the laser emission.

For a continuous-wave laser the cavity is configured to consistently emit some fraction of the light produced, such that a steady flux of photons is produced. But what does this steady flux of photons look like? In the laboratory we might describe the beam by its average power, but really this is merely an approximation of the average number of photons which are emitted per second. If instead we describe the beam by this number, we can begin to notice some subtlety in the nature of the emission.

Take as an example a typical HeNe laser. Such a device might emit 1 mW of 633 nm photons, which corresponds to about $3.2 \times 10^{15}$ photons per second. Repeatedly measuring for one second at a time, we might expect to measure $3.2 \times 10^{15}$ photons each time, but in reality the emission is probabilistic and we only measure approximately this number in each experiment. The actual distribution of photon number we measure is governed by Poisson statistics.

The Poisson distribution describes the probability of the observation of any given number of events, given the average number of events expected. For a number of events $n$ and an average $\langle n \rangle$, this is:

$$p\left(n|\langle n\rangle\right) = \frac{\langle n\rangle^n \, e^{-\langle n\rangle}}{n!} \tag{2.1}$$

Using our laser as an example, if the beam were attenuated to 1 pW we would expect to measure $3.2 \cdot 10^6$ photons per second, which is still reasonably large. But if we now measure the intensity every 1 µs (1 MHz acquisition), we find 3.2 photons each period. A fractional photon is not a physical value, and thus we may actually measure 3 or 4 photons in a period, but we are also quite likely to measure 2, 5, or even 0; averaging over many events will yield $\langle n \rangle = 3.2$. This Poissonian or "shot" noise is the fundamental limit to counting experiments: the precise determination of an average intensity requires the collection of sufficient number of photons over a sufficient number of integration periods to either be able to fit to a Poisson distribution, or to the collection of a sufficient number of photons to have an acceptably small uncertainty.

### 2.1.1 Modeling a Poissonian Source

To demonstrate these principles, we can numerically model the emission from a Poissonian source in one of two ways: by subdivision of time into fixed intervals and determining the events which occurred in each period, or by determination of the emission time of each photon and later grouping them into time intervals.

In the time-binning method, we use the average number of events expected for given time interval to draw a number from the Poisson distribution, and repeat the process for every time interval in the simulation. Most modern programming environments provide an interface to the Poisson distribution,[70] and generating an intensity in this fashion is achieved by drawing values from this distribution for each time interval. This method is most effective when studying signals without the need to resolve individual events, and scales primarily with the number of time intervals simulated.

In the generator method, for an average detection rate $\langle n \rangle$ the waiting time distribution is an exponential:

$$p(\tau) = \langle n \rangle \, e^{-\langle n \rangle \tau} \tag{2.2}$$

To generate events in this fashion, define some starting time $t$. Draw $\tau$ according to Equation (2.2), and emit the event as having occurred at $t + \tau$. Set $t \leftarrow t + \tau$,

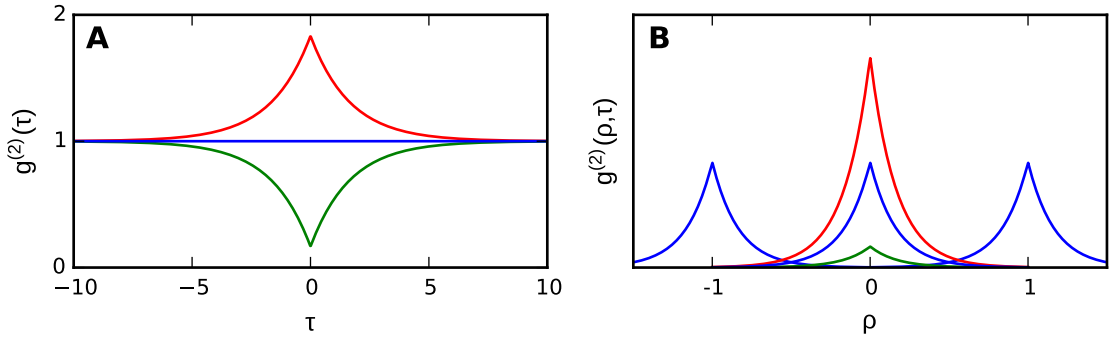


Figure 2-1: An illustration of photon statistics, as measured using $g^{(2)}$. **A** Bunched (red), Poissonian (blue) and antibunched (green) emission, as measured through $g^{(2)}(\tau)$. For larger time delays, all three sources shown are Poissonian. **B** Equivalent bunched (red), Poissonian (blue), and antibunched (green) emission, as measured under pulsed excitation. Because the excitation is no longer Poissonian, the relative areas of the peaks corresponding pairs of photons arriving after the same ($\rho = 0$) or different ($\rho \neq 0$) provide the measure of the statistics.

and repeat as necessary. This method scales primarily with the number of events simulated, and is most useful when the resolution of individual events is necessary.

## 2.2 Non-Poissonian Emission

The canonical method for determining whether an emission source is the pair correlation function $g^{(2)}$, in which we compare the probability of observing a pair of photons separated in time by $\tau$ with the probability of observing the same pair of photons if all photons are distributed uniformly in time. In the field representation, this is:

$$g^{(2)}(\tau) = \frac{\langle E^*(t)\, E^*(t+\tau)\, E(t)\, E(t+\tau)\rangle}{\langle |E(t)|^2\rangle \langle |E(t+\tau)|^2\rangle} \tag{2.3}$$

This is also commonly expressed as the cross-correlation of two single-photon detectors:

$$g^{(2)}_{(a,b)}(\tau) = \frac{\langle I_a(t)\, I_b(t+\tau)\rangle}{\langle I_a(t)\rangle \langle I_b(t+\tau)\rangle} \tag{2.4}$$

The use of a pair of distinct detectors ensures that all detected pairs are composed of two distinct photons.

We can also measure $g^{(2)}$ as the number of photon pairs in a discrete measurement:

$$g^{(2)}(\tau) = \frac{\left|\left\{(\gamma_0,\gamma_1)\middle|\begin{array}{r}\gamma_0,\gamma_1\in\Gamma\\ \gamma_0\neq\gamma_1\\ \mathcal{T}(\gamma_1)-\mathcal{T}(\gamma_0)=\tau\end{array}\right\}\right|}{\left|\left\{\gamma\middle|\begin{array}{r}\gamma\in\Gamma\\ \mathcal{T}(\gamma)\in[0,T)\end{array}\right\}\right|\left|\left\{\gamma\middle|\begin{array}{r}\gamma\in\Gamma\\ \mathcal{T}(\gamma)\in[\tau,T)\end{array}\right\}\right|} \tag{2.5}$$

Here, the numerator is the size of the set formed by taking all pairs of distinct photons $(\gamma_0, \gamma_1)$ from the set of all photons $\Gamma$, where the two photons arrive $\tau$ time apart ($\mathcal{T}(\gamma)$ returns the arrival time of the photon). Likewise, the denominator contains the number of photons arriving in the experiment and those arriving no less than $\tau$ after the start of the experiment, respectively (integration time $T$). This notation is the most accurate representation of how the correlation function is actually measured for photon arrival data, and is readily extended to higher orders of correlation.

However it is measured, the intuition of $g^{(2)}$ is the same, and the three regimes are illustrated in Figure 2-1. For a Poissonian source, $g^{(2)}(\tau) = 1$, that is, the detection of a photon at some time $t$ does not indicate an increased or decreased probability of observing a photon at some other time. For some emitters, we measure $g^{(2)}(\tau) > 1$, which is denoted "bunching": the detection of a photon signals that a second photon is more likely to be detected $\tau$ later than would be predicted by a uniform distribution of photons. This phenomenon arises in thermal emission,[71] pulsed laser sources, stimulated emission,[72] excitonic fine-structure "shelving",[53] excitonic quenching,[55] and spontaneous parametric downconversion,[73] in which pairs are more likely to be found with no time separation than with a finite time delay. Photon bunching also arises in fluorescence correlation spectroscopy (FCS), in which the residence of an individual emitter in the focal volume increases the relative probability of detecting pairs of photons.[74,75] Bunching may also arise due to photoluminescence intermittency

("blinking"), in which emission arrives in bursts of some finite duration.

The inverse phenomenon is known as "antibunching", where $g^{(2)}(\tau) < 0$. For antibunched emission, the arrival of a photon indicates the improbability of detecting a second photon some time $\tau$ later. This typically arises for emission from a single two-level system, in which the generation of a photon indicates the bleaching of the excited state. For such a system the shape of $g^{(2)}(\tau)$ results from the finite lifetime of the excited state: even with instantaneous re-excitation, the second photon can only be generated as quickly as the excited state relaxes. Antibunched emission has been found in individual organic dyes,[76,77] colloidal quantum dots,[43,45,46,78–80] epitaxial quantum dots,[81,82] atomic vacancy centers,[83,84] and atoms,[85] though ensembles of these emitters are effectively Poissonian sources (see Section 2.2.1).

### 2.2.1 Modeling Non-Poissonian Emission

To develop an intuition for why a single emitter may exhibit antibunching while an ensemble of single emitters does not, we can study the emission dynamics of a two-level system. Let us assume that our emitter has a ground state and one excited state, and that the excited state spontaneously radiatively relaxes to the ground state with rate $k_r$. Under continuous excitation there is some rate $k_{ex}$ at which the emitter can be excited from the ground state to the excited state, yielding the following transition rules:

$$\mathrm{G} \xrightarrow{k_{ex}} \mathrm{E} \tag{2.6}$$

$$\mathrm{E} \xrightarrow{k_r} \mathrm{G} + \gamma \tag{2.7}$$

These equations of motion can be simulated effectively using the Gillespie algorithm:[86]

1. Set populations $[G] \leftarrow [G]_0$ and $[E] \leftarrow [E]_0$. Set time $t \leftarrow 0$.

2. Determine the rate $k$ of any transition according to $k = k_{ex}[G] + k_r[E]$. Draw $\tau$ from $p(\tau) = ke^{-k\tau}$, and advance time $t \leftarrow t + \tau$.

3. Determine which transition occurred by drawing a uniform $r$ from the range $[0, k_r[E] + k_{ex}[G])$.

   (a) If $r < k_r[E]$, relaxation occurred. Emit a photon with time $t$ ($[\gamma] \leftarrow [\gamma]+1$), and set $[G] \leftarrow [G]+1$, $[E] \leftarrow [E]-1$.

   (b) Otherwise, excitation occurred. Set $[G] \leftarrow [G]-1$, $[E] \leftarrow [E]+1$.

4. Repeat from step 2 as necessary.

For a single emitter in the ground state, emission is not possible until the emitter has been re-excited. Even in the limit of arbitrarily rapid excitation ($k_{ex} \to \infty$), once a photon has been emitted the next photon can be detected only after some exponential waiting time with constant $k_r$. For continuous-wave (CW) antibunching measurements, this manifests as an exponential dip in $g^{(2)}(\tau)$,[43,78,87–89] which tends toward $g^{(2)}(0) = 0$ in the ideal case.

Suppose we instead have two emitters. Individually the two emitters will both exhibit antibunching, but together there is now some probability of both emitters relaxing simultaneously, decreasing the overall extent of antibunching to $g^{(2)}(0) = \frac{1}{2}$. For $n$ emitters, this becomes $g^{(2)}(0) = \frac{n-1}{n}$, which becomes experimentally indistinguishable from 1 for large values of $n$. Intuitively this is sensible: there are $n$ possible emitters for the first photon but only $n-1$ for a second photon ($n(n-1)$), but at arbitrary time delay either photon could be generated by any of the $n$ emitters ($n^2$). Working out the intermediate dynamics can be non-trivial, particularly when the system under study is not strictly a two-level system (e.g. nanocrystals), but this transition-based intuition carries over.

## 2.3 The Statistics of Emission from Nanocrystals

Experimentally, the use of CW excitation and detection for measuring $g^{(2)}(\tau)$ is expensive because there are many possible times at which excitation and emission events may occur and thus there are many histogram bins into which pairs may be assigned. While antibunching may be measured in this fashion, analysis of a CW $g^{(2)}$ can

be complicated by several factors related to nanocrystal photophysics, particularly the presence of multiexcitons (multiply-excited states).[78] As a result, the primary paradigm for correlation measurements requiring resolution of antibunching is that of pulsed excitation,[42,44,45,54] in which we can directly resolve the number of photon pairs arriving after the same or different excitation events. In such an experiment we measure $g^{(2)}(\rho, \tau)$, where $\rho$ is the difference in the index of the excitation pulse between two photons, and $\tau$ is the difference in the arrival times of those photons relative to their proximal excitation events. For measuring the extent of antibunching we are often interested only in the ratio of the areas of the "center" and "side" peaks,[54] which is:

$$g_0^{(2)} = \frac{\int_{-T_{\text{rep}}}^{T_{\text{rep}}} g^{(2)}(0, \tau)\, d\tau}{\int_{-T_{\text{rep}}}^{T_{\text{rep}}} g^{(2)}(1, \tau)\, d\tau} \tag{2.8}$$

In Nair et al.[54] the authors derived a model for $g_0^{(2)}$ by considering the joint probability of detecting one photon each on two detectors. Here, we will perform the inverse derivation, in which we model the excitation, emission, detection, and correlation of nanocrystal emission sequentially (see also Bischof et al.[45]). The goal of this derivation is to consider all possible sequences of excitation, emission, and detection, and to group these events by the number of detected photons for ease of calculating $g^{(n)}$.

We will model all nanocrystal excitation as the instantaneous generation of some excitonic state $m$X (a whole number $m$ excitons). After excitation, the state relaxes to produce some number of photons, which are subsequently collected, transmitted, and detected with some probability by the microscope. For now, we neglect the chromatic effects of the microscope. We also neglect emission during excitation, as would be observed due to the finite duration of the excitation pulse. We assume that the nanocrystal returns to the ground state (0X) between excitation pulses.

First, we consider the excitation of a nanocrystal. For a given excitation pulse, the probability of generating $m$X is denoted as $\chi_m$. By conservation of number, we have $\sum_{m=0}^{\infty} \chi_m = 1$. For optical excitation well above the band gap (into the "continuum"

of states), $\chi_m$ is well-modeled as a Poisson distribution for small values of $m$,[45,54] given the average probability $\langle n \rangle$ of a single absorption event. This expression may be modified as needed to include effects such as exciton fission (see Section 8.1).

Next, we consider emission. For a given $m$X, there is a probability $\gamma_{m,m}$ of the relaxation of that state yielding a photon and a corresponding probability $(1 - \gamma_{m,m})$ of that relaxation not producing a photon. The subsequent state $(m-1)$X has a probability $\gamma_{m,m-1}$ of yielding a photon, and so on for each subsequent relaxation until the nanocrystal reaches the ground state. Thus the generation of $m$X can yield anywhere from 0 to $m$ photons, depending on the quantum yield of each intermediate state. We will assume that these subsequent multiexciton states $m$X have the same quantum yield as the state produced by direct excitation, such that $\gamma_{m,p} = \gamma_{n,p}$ (we demonstrate this principle in Chapter 6). This gives the following probability distribution of generating $p$ photons during the relaxation of $m$X:

$$\eta_{m,p} = \sum \left\{ \prod_{q=1}^{m} \gamma_q^{v_q} \left(1 - \gamma_q\right)^{(1-v_q)} \middle| \begin{array}{l} \boldsymbol{v} \in \mathbb{Z}_2^m; \\ |\boldsymbol{v}|^2 = p \end{array} \right\} \tag{2.9}$$

This expression is shorthand for the sum over the set of all possible choices of emission or non-emission at each step of relaxation from $m$X, given the generation of $p$ photons. The vector $\boldsymbol{v}$ contains the choice of emission (1) or non-emission (0) as its elements, of which exactly $p$ are equal to 1.

This partitioning preserves the overall probability, since we have accounted for all possible relaxation pathways:

$$\sum_{q=0}^{m} \eta_{m,q} = 1 \tag{2.10}$$

Expanding Equation (2.9) for the biexciton (2X) we have:

$$\eta_{2,2} = \gamma_2 \gamma_1 \tag{2.11}$$

$$\eta_{2,1} = \gamma_2 (1 - \gamma_1) + (1 - \gamma_2) \gamma_1 \tag{2.12}$$

$$\eta_{2,0} = (1 - \gamma_2)(1 - \gamma_1) \tag{2.13}$$

Thus we see that, in order to yield two photons, the biexciton and subsequent monoexciton must emit. A single photon is produced if only one of these states emits a photon, and no photons are produced if neither state emits.

Combining all excitonic states, we obtain the probability of a pulse of excitation producing $n$ photons:

$$\Gamma_n = \sum_{m=n}^{\infty} \chi_m \eta_{m,n} \tag{2.14}$$

Experimentally, measuring $\Gamma_n$ is non-trivial due to the imperfections of the microscope and other apparatus, which can modify the effective distribution dramatically (see Section 2.3.2). As a result, we often measure correlations of photons, which consists of counting events in which one, two, three, or more photons are detected. These multi-photon events are found at a rate per excitation pulse which results from $\Gamma_n$:

$$\mathrm{G}_n = \sum_{m=n}^{\infty} \frac{m!}{(m-n)!} \Gamma_m \tag{2.15}$$

The permutation prefactor arises due to the fact that any ordering of photons will be counted in the correlation measurement: the detection of two photons produces two one-photon correlation and two two-photon correlations; the detection of three photons produces six three-photon correlations, six two-photon correlations, and three one-photon correlations.

### 2.3.1 The Manifestation of $G_n$ in $g^{(n)}$

For each order of $g^{(n)}$ under pulsed excitation, there are a few distinct types of events. In $g^{(2)}(\rho)$, the "center" peak ($g^{(2)}(0)$) corresponds to the events in which pairs of photons are detected after a single excitation pulse. This is precisely $G_2$. The other unique peak is the "side" peak ($g^{(2)}(\rho \neq 0)$), which corresponds to two photons arriving after two different pulses. This is $(G_1)^2$, since $G_1$ is the rate at which one-photon events are measured. Thus the measurement of the extent of antibunching yields:

$$g_0^{(2)} = \frac{G_2}{(G_1)^2} \tag{2.16}$$

This expression is general to any model for $\Gamma$. For Poissonian excitation and the limit of low excitation flux, we obtain as a time-averaged result:

$$\lim_{\langle n \rangle \to 0} g_0^{(2)} = \frac{\langle \gamma_2 \gamma_1 \rangle_t}{\langle \gamma_1 \rangle_t^2} \tag{2.17}$$

which is the same result as Nair et al.[54].

This idea is extensible to larger orders of correlation. For example, in $g^{(3)}$ there are three types of photon triplets arising from one, two, or three excitation pulses. These correspond to $G_3$, $G_2G_1$, and $G_1^3$, respectively, and inform on triexciton emission (see Chapter 6).

### 2.3.2 Introduction of Loss

In a true experiment, there will be some losses in the microscope. For example, the microscope objective has a finite probability of collecting emission, the mirrors have finite probability of reflection, and the detectors have a finite probability of detection. Furthermore, single-photon detectors may only detect a single photon at a time, and thus each of the various schemes for multi-photon detection yield some modified probability of detecting each number of photons.[89,90] We can introduce each of these effects into our measurement model.

The uniform loss of photons (transmission probability $\xi$) manifests as a decrease

in the number of photons detected:

$$\Gamma_n^{(\xi)} = \xi^n \sum_{m=n}^{\infty} \frac{m!}{n!\,(m-n)!} (1-\xi)^{m-n} \Gamma_m \tag{2.18}$$

While uniform loss does does affect the correlation rates $G_n$ it does not affect measurements of antibunching ($g_0^{(n)}$).[45] Thus the measurement of antibunching is immune to microscope drift so long as the changes in excitation do not yield significantly different $\Gamma_n$.

The loss of photons emitted from specific states results in a modified probability of yielding a photon from that state. For example, the filtration of triexciton emission sets $\gamma_3 = 0$, eliminating all photon generation pathways which rely on the production of a photon from this state.

Imperfect detection is somewhat more complicated to introduce, but ultimately manifests as a geometric correction for a given number of photons. For example, in a microscope capable of measuring a single photon per pulse of excitation, we have:

$$\Gamma_n = \begin{cases} \Gamma_0; & n = 0 \\ 1 - \Gamma_0; & n = 1 \\ 0; & n \geq 2 \end{cases} \tag{2.19}$$

Thus we measure photon if at least one is produced, and zero otherwise. For a microscope with two single-photon detectors in the Hanbury Brown-Twiss configuration:[71]

$$\Gamma_n = \begin{cases} \Gamma_0; & n = 0 \\ \sum_{m=1}^{\infty} \left(\frac{1}{2}\right)^{m-1} \Gamma_m; & n = 1 \\ \sum_{m=2}^{\infty} \left(1 - \left(\frac{1}{2}\right)^{m-1}\right) \Gamma_m; & n = 2 \\ 0; & n \geq 3 \end{cases} \tag{2.20}$$

For such a scheme, one photon is detected if one photon is produced, or if all photons arrive at the same detector. Two photons are detected if at least two photons are

produced, and at least one photon arrives at each detector.

## 2.4 Conclusions

In this chapter, we have discussed a general method for modeling the statistics of multiexciton emission. We began by describing the statistics of excitation by a pulsed source, which leads to a distribution of the number of excitons produced. Each multiexciton then relaxes by recombination of individual carriers, leading to cascades which produce some number of photons. These effects were combined to form a general model for the rates at which various correlation events are detected, which was used to model $g_0^{(n)}$. We discussed how these models may be extended to account for experimental artifacts, spectral resolution, or non-linear excitation.

# Chapter 3

# Analysis of a Photon Stream

For all of the single-molecule studies contained in this thesis, the analysis was performed using custom C and Python code[1]. In this chapter, we discuss the fundamental algorithms used for these calculations, and how they are combined to perform useful analyses of photon arrival time data. This is intended as a guide for the reader interested in understanding the high-level ideas behind the correlation code before using or modifying it. The Python code listings in this chapter contain equivalent implementations of the algorithms used in the C code, for ease of understanding.

The code is hosted in two git repositories at `http://github.com/tsbischof`, called `libpicoquant` and `photon_correlation`. `libpicoquant` contains the C code necessary to translate raw binary data from PicoQuant hardware into standardized ascii formats, and `photon_correlation` contains the C code necessary to perform the manipulation and measurements of such photon data, the results of which are output in various csv-based ascii formats. `photon_correlation` also contains a Python module which provides interfaces to the various data formats produced by the C code. This Python code has been written for version 3.4, but is largely portable to earlier versions.

The overall workflow of the code is to first obtain photon records, then to transform those records into correlations or other records, and finally to measure the statistics

[1]The C code is written in the C99 dialect, and has been tested most extensively on 64-bit GNU/Linux platforms using the clang compiler.

of these transformed records. This process is accomplished through a variety of standalone executables which may be joined through pipes or related idioms. These individual programs are described in Section 3.5, and the technical details of their implementation are discussed in Sections 3.1 and 3.2.

## 3.1 Transforming Raw Data Into Photon Records

The package `libpicoquant` is designed to convert the raw binary data produced by one of several PicoQuant time-correlated single-photon counting modules (TCSPC; TimeHarp, PicoHarp, HydraHarp) into text data in one of several common formats. These measurements fall into three main categories: histogramming, t2, and t3.

Histogramming mode refers to the measurement of emission lifetime by correlation of excitation and emission events. The data in this format consist of an array of histogram bins and counts, representing the number of photons which arrived at various times after an excitation pulse on a given detection channel. The hardware modules have fixed numbers of histogram bins, e.g. $2^{16}$ for the HydraHarp, and the effective range of detectable times is set by defining the temporal width of each bin. When processed using `libpicoquant`, the data is output in the following format:

curve number, time bin (left), time bin (right), counts

The other modes of data known to `libpicoquant` are t2 and t3. These are photon arrival time formats (time-tagged time-resolved data (TTTR)), which produce a record of every detection event and the information known about that event. These are recorded in order, and thus can be processed to yield a stream of detection events sorted in time.

In t2 mode, photon arrivals are recorded with the detection channel and the arrival time relative to an absolute experimental clock. This mode is most appropriate for CW experiments, in which there is no direct experimental clock and thus events may be timed relative to an arbitrary start. To overcome the time resolution limitations of TCSPC hardware it is also feasible to use t2 mode to explicitly record the arrival

of every excitation pulse in a pulsed experiment, by performing the correlation of excitation and emission events in software. Data in t2 mode are output in the following format:

detection channel (indexed from 0), arrival time (in ps)

In t3 mode, photon arrivals are recorded with the detection channel, the index of the most recent excitation pulse, and the arrival time relative to that excitation pulse. This mode is appropriate when an experimental clock is present, such as a pulsed laser. The hardware tends to limit the temporal resolution of these events, for the same reasons as in histogramming mode. Data in this mode are output in the following format:

detection channel (indexed from 0), arrival pulse, arrival time (in ps)

### 3.1.1 Structure of PicoQuant data

A PicoQuant data file contains four distinct sections: a header specifying the hardware type and version, a header specifying the measurement mode and general options, a header specifying options specific to the measurement mode, and the data corresponding to the measurement. In `picoquant`, a given input file is translated into the appropriate text format automatically: the three headers are decoded sequentially to determine the correct decoder and settings for the data, and then the data are generated as a text stream.

For histogram measurements, the data are a linear array of unsigned integer counts. These are read into memory, and used to produce the definition and counts for each histogram bin.

For TTTR measurements, the data are an array of records of two types: time overflow records, and photon arrival events. Time overflow records are used to implement a protocol in which finite bit-width records may be used to represent arbitrary arrival times. By emitting a record at fixed intervals of time and keeping track of the number of these overflows, the effective experimental clock may be reproduced. For

t2 mode the overflows are recorded for the arrival time dimension, and for t3 mode the overflows are recorded for the pulse number.

Photon arrival events contain information about the detection channel and arrival time for a detection event. In t2 mode the arrival time specified is relative to the absolute clock as implemented using overflow records. In t3 mode the arrival pulse is specified in the same way, but the arrival time relative to the excitation is specified as the index of the effective histogram bin: to produce the arrival time, the index is multiplied by the bin width. In `picoquant`, detection channels are stored as 32-bit integers, and the arrival pulse and time are stored as 64-bit integers. These bit widths are sufficient for most practical purposes; the use of 64-bit integers to represent time in picoseconds limits experiments to approximately 213 years.

## 3.2 Fundamental Photon Stream Measurements

Analysis of the photon stream typically involves some combination of a few fundamental methods, such as intensity calculation or photon correlation.[63] In this section, we discuss these methods and describe the algorithms implemented in `photon_correlation`.

All of the algorithms used in `photon_correlation` follow a common paradigm of an input iterator. The goal of a such an iterator is to take as input some number of records, and provide as output the transformed version of those records upon request, producing the result only at the time it is needed. For example, an iterator for a text file might accept the filename as input, then provide an interface necessary to read a single line from the file at a time. These methods are effective if the input is already sorted.

The purpose of iteration is to minimize memory use, and to eliminate the front-loaded overhead of reading the set of photon records into memory. This memory overhead can be considerable – an experiment can readily produce 1 GB of data – and this form enables the the early termination of a calculation at little to no computation expense. These benefits come at the expense of algorithmic complexity, because the

iterator must explicitly track its state within a series of decisions. For small, well-defined problems it can be significantly simpler to use a less general algorithm, but for `photon_correlation` the goal is to perform calculations in a correct, general, and reusable fashion.

For all of the methods presented, we assume an input photon stream which is sorted in time. For the purposes of the sample code, we will treat t2 photons as objects with channel (photon.channel) and time (photon.time) information. T3 photons are objects with channel (photon.channel), pulse index (photon.pulse), and time (photon.time) information.

### 3.2.1 Intensity Calculation

For studies of photoluminescence intermittency ("blinking"), we must characterize the fluctuations of emission intensity over time. In hardware this is achieved using a boxcar integrator, which measures the integrated current or voltage for each fixed interval of time. For discrete signals such as photon arrival times, this signal represents the number of counting events seen during each interval.

To measure the intensity of emission, we define an origin in time $t_0$ and a window width $\Delta t$. Under this definition each time window may be defined as the range of times $[t_0 + j\Delta t, t_0 + (j+1)\,\Delta t)$ for some integer $j$, where "[" indicates inclusion of the bound and ")" indicates exclusion. This convention ensures that time values falling on the edge of a histogram bin are deterministically assigned.

An intensity stream may be generated as shown in Listing 3.1. This method is optimal in memory, in the sense that each photon is processed for exactly as long as needed to increment the counts for the correct time window, and each time window is only processed as long as it is possible to find another photon within it. It is best-suited for high count rates (many photons per bin), and in this regime scales linearly with the number of photons. For low count rates it is still memory-efficient but must produce many empty intensity bins, such that processing time scales inversely with the bin width.

In `photon_correlation`, `photon_intensity` is the interface to intensity calcula-

Listing 3.1: Implementation of an intensity stream. Here, photon.window_dim represents the dimension used to represent the passage of time. For t2 data, this is the photon arrival time (photon.time), and for t3 data the pulse index is used instead (photon.pulse).

```
def intensity(photons, bin_width):
    window = Window(bin_width)
    counts = 0

    for photon in photons:
        while True:
            if photon.window_dim in window:
                counts += 1
                break
            else:
                yield(window, counts)
                counts = 0
                window.next()

    yield(window, counts)
```

tions. This code implements the iterator algorithm of Listing 3.1.

### 3.2.2 Correlation

To study the temporal statistics of emission, we calculate the $n$th-order correlation function $g^{(n)}$, which measures the relative probability of detecting $n$ photons with some specified spacing in time, compared to the probability of randomly finding the $n$ photons with that spacing in time. The most common experimental form of this function is the second-order $g^{(2)}$, as measured by two different detectors:

$$g^{(2)}_{(a,b)}(\tau) = \frac{\langle I_a(t)\, I_b(t+\tau)\rangle_t}{\langle I_a(t)\rangle_t \langle I_b(t+\tau)\rangle_t} \tag{3.1}$$

In Equation (3.1), the numerator is the joint probability of finding a photon at time $t$, and another at time $t+\tau$, averaged over all possible arrival times. The denominator represents the probability of finding *any* pair of photons. This leads to the ideas of photon bunching, antibunching, and Poissonian emission which are extensively discussed in Chapters 2, 4 and 6.

Experimentally, $g^{(2)}$ can be measured using either of two paradigms: photon cor-

relation,[91,92] or intensity correlation.[91,93] In photon correlation, we find all pairs of photons and histogram these events to obtain a measurement of $g^{(2)}(\tau)$. This retains the time resolution of the photons themselves, and is the best method to use when there are few photons per effective time bin in the $g^{(2)}$ (the intensity stream is sparse). The intensity correlation consists of creating the intensity vector $I(t)$, and performing the products $I(t)\,I(t+\Delta t)$ individually (this can also be implemented efficiently with an FFT). This is the best method to use if there are several photons per time bin (the intensity stream is dense). As with most sparse methods, hybrid algorithms exist to optimally join the regimes of low and high count rates.[94,95]

### Photon Correlation

Before discussing a general $n$th order algorithm, we will study how to effective generate all pairs of photons. First, we typically limit our search to a particular range of time delays $\tau$, such that there is maximum separation $\tau_{\max}$. Next, we note that the time-sorted nature of the photon stream enables us to search ahead for all potential pairings of photons with a particular starting photon, and to truncate the search as soon as we find a photon with a time separation greater than $\tau_{\max}$. This can be accomplished as shown in Listing 3.2. The central loop here adds photons to a running queue one at a time. As the photons are added, if the first and last photons in the queue are too distant to correlate, all of the photon pairs associated with the first photon are emitted. This process continues until the end of the photon stream, at which point all remaining pairs are emitted.

Extending this idea to arbitrary order, we obtain the method of Listing 3.3.

The computational expense of the correlation grows as the number of correlations produced. For $N$ total photons spanning an integration time of $T$, this is on the order of $N^n$ tuples. By limiting the search to a finite time span $\tau_{\max}$, this reduces the output to order $N^{n-1}\left(\frac{\tau_{\max}}{T}\right)$. Practically speaking, for small $\tau_{\max}$, the cost is decreased by a factor of $N$. For larger $\tau_{\max}$ it is necessary to account for the finite integration time for proper normalization, as this limits the effective range of possible arrival times.

In `photon_correlation`, `photon_correlate` contains an implementation of an

Listing 3.2: Efficient generation of all photon pairs with no more than the specified difference in arrival time.

```
def correlate_g2(photons, max_time_distance):
    def emit(queue):
        src = queue.pop()
        for dst in queue:
            yield(src, dst)
            yield(dst, src)

    queue = list()

    for photon in photons:
        if len(queue) < 2:
            pass
        elif photon.time - queue[0].time < max_time_distance:
            pass
        else:
            for pair in emit(queue):
                yield(corr)

        queue.append(photon)

    while len(queue) > 1:
        for pair in emit(queue):
            yield(corr)
```

efficient algorithm which performs the correlation to arbitrary order. These correlations are typically fed into `photon_histogram`, which performs the histogramming to arbitrary order. This combination of correlation and histogramming steps can be performed most simply with `photon_gn`.

### Intensity Correlation

If our signal contains several photons per unit of time resolution, an intensity correlation can be a more efficient calculation.

For linear-spaced bins, the correlation may be calculated as the series of inner products produced by the intensity vector shifted for various delays in time, as shown in Listing 3.4. Note that the normalization term explicitly accounts for the effects of finite integration time.

This inner-product method becomes memory-intensive if we need to calculate $g^{(2)}$

Listing 3.3: Efficient generation of all photon n-tuples with no more than the specified difference in arrival time.

```
def correlate_gn(photons, order, max_time_distance):
    def emit(queue):
        src = queue.pop()
        for dst in itertools.combinations(queue, r=order-1):
            for corr in itertools.permutations([src] + list(dst),
                                               r=order):
                yield(corr)

    queue = list()

    for photon in photons:
        if len(queue) < order:
            pass
        elif photon.time - queue[0].time < max_time_distance:
            pass
        else:
            for corr in emit(queue):
                yield(corr)

        queue.append(photon)

    while len(queue) >= order:
        for corr in emit(queue):
            yield(corr)
```

over a large span of time with fine resolution. To span a range of time delays, we can instead calculate a series of linear intensity correlations with a logarithmically-increasing effective time resolution. This is known as the multi-tau method,[93] as shown in Listing 3.5. The essential idea of the algorithm is to calculate the intensity for linear-spaced bins with some fine fundamental time resolution, and then to recombine these bins as possible for increasingly coarse resolution. For each depth of binning, we use some number of registers to record the intensity at that effective resolution. A full inner-product correlation is equivalent to having binning greater than or equal to the number of time bins in the measurement.

Multi-tau algorithms can be implemented efficiently in hardware,[96] and commercial FCS/DLS systems tend to use such hardware. Software implementations can be quite effective, particularly if used in conjunction with photon pair correlation for small time delays.[94,95]

Listing 3.4: Calculation of the intensity autocorrelation as a series of vector inner products.

```
def g2_intensity(intensity):
    intensity = numpy.array(intensity)
    for tau in range(1, len(intensity)):
        src = intensity[tau:]
        dst = intensity[:-tau]
        yield(tau, numpy.dot(src, dst)/(sum(src)*sum(dst)))
```

In `photon_correlation`, `intensity_correlate` is the interface to the multi-tau algorithm, and accepts as input a stream of linear-spaced bins. For photon arrival data, `photon_intensity_correlate` performs the intensity calculation and multi-tau correlation.

### 3.2.3 Photon Number Resolution

To study the dynamics of multiexciton emission, we can measure the lifetimes of photons emitted in pairs, triplets, or higher-order tuples. The idea here is that, if we form a biexciton or two-exciton state, there is some probability of emitting zero, one, or two photons, since each exciton can either emit or not emit. This is the same principle used in understanding the structure of the $g^{(2)}$,[45,54] but now instead of counting the relative probabilities of seeing biexciton/monoexciton pairs versus monoexciton/monoexciton pairs, we want to isolate the photons counted as part of the biexciton/monoexciton pairs (see Chapter 6). In these pairs, the first photon has a high probability of being the one emitted by the biexciton, and the second photon corresponds to the monoexciton photon.

To do this, we require a pulsed excitation source, which allows us to assume that all excitations are created effectively at the same time, such that any subsequent dynamics are associated with normal relaxation processes. This also requires that the repetition time between excitation pulses be sufficiently large to permit relaxation to occur. Under these conditions, we can isolate tuples of photons by counting the number of photons which arise after a single pulse of excitation. Thus our task is to transform all $n$-photon events in such a way that enables us to identify the number

Listing 3.5: Calculation of the intensity autocorrelation using the multi-tau method.

```
def g2_multi_tau(intensity, binning=2, registers=16, depth=20):
    signal = numpy.zeros(depth, registers)
    g2 = numpy.zeros(depth, registers)
    total = numpy.zeros(depth, registers)
    pushes = numpy.zeros(depth)

    for counts in intensity:
        for level in range(depth):
            pushes[level] += 1
            signal[level, 1:] = signal[level,:-1]

            if level == 0:
                signal[level, 0] = counts
            else:
                signal[level, 0] = sum(signal[level-1, 0:binning])

            if pushes[level] % binning != 0:
                break
            else:
                g2[level, :] += signal[level, 0] * signal[level, :]
                total[level, :] += signal[level, :]

    return(g2_multi_tau_norm(g2, total, pushes))
```

of photons and their ordering. One option is to map this metadata onto the photon detection channel, such that $d$ physical channels can be represented by $d(d+1)/2$ logical channels. For the $m$th photon of an $n$-photon event, indexed from 0:

$$\text{channel} = \frac{n\,(n-1)}{2} + (m-1) \tag{3.2}$$

This assignment can be implemented as shown in Listing 3.6.

Note that only the first photon found on a particular physical channel may be used. This is required because a subsequent detection event is, at least for single-photon avalanche photodiodes (SPADs), not a true photon but electronic afterpulsing (see Appendix A.2.1). The exact rate at which afterpulsing occurs is a function of several parameters, including excitation fluence and wavelength, but it is often significantly more probable than any true detection event. This temporal filter does effectively remove the afterpulsing events (see Figure A-6), and for some purposes the storage

Listing 3.6: Transformation of an incoming stream of photons into logical events, with channels assigned to indicate the number of photons and order of arrival after a single excitation pulse. For an excitation pulse yielding one photon, the photon arrives on logical channel 0. For a pair of photons, the first arrives on logical channel 1, and the second on channel 2. Higher-order tuples are assigned according to Equation (3.2).

```
def photon_number_to_channels(photons, filter_afterpulsing=True):
    def emit_queue(queue):
        n_photons = len(queue)
        base_channel = n_photons*(n_photons-1)//2
        for channel, photon in enumerate(queue, start=base_channel):
            photon.channel = channel
            yield(photon)

    queue = list()

    for photon in photons:
        if len(queue) == 0:
            queue.append(photon)
        elif photon.pulse == queue[0].pulse:
            if filter_afterpulsing and \
               any(map(lambda other: photon.channel == other.channel,
                   queue)):
                continue
            else:
                queue.append(photon)
        else:
            for result in emit_queue(queue):
                yield(result)

            queue.clear()
            queue.append(photon)
```

overhead of t3 data (relative to histogramming data) is acceptable.

In `photon_correlation`, `photon_number_to_channels` is the interface to number resolution. The output photons are typically used for lifetime calculations, which are performed with `photon_gn`.

## 3.3 Characterizing Dynamics

For many purposes, the measurement of a lifetime ($g^{(1)}$) or other $g^{(n)}$ over the course of an experiment is sufficient, but in many cases there is additional information encoded in the photon stream. For example, as a quantum dot blinks, the lifetime

Listing 3.7: A method for calculating $g^{(n)}$ for every fixed interval of time.

```
def gn_td(photons, window_width, **gn_params):
    window = Window(window_width)
    gn = GN(gn_params)

    for photon in photons:
        while True:
            if photon in window:
                gn.push(photon)
                break
            elif photon < window:
                break
            else:
                gn.flush()
                yield(gn)
                gn.clear()
                window.next()

    gn.flush()
    yield(gn)
```

of its emission may or may not vary.[42,45,46,55,97] In order to capture these dynamics, researchers have developed a variety of methods which attempt to characterize the dynamics of emission.[63] In this section, we discuss some of these methods, and how these analyses are implemented in `photon_correlation`.

### 3.3.1 Time-Dependent Analysis

In a time-dependent analysis we calculate $g^{(n)}$ for each window of some width $\Delta t$ (see Listing 3.7). This is expensive in disk space or memory, since we must emit the entire array associated with $g^{(n)}$ for each time window. In principle this array is sparse and could be implemented as such, but `photon_correlation` does not do so.

In `photon_gn`, use the `--window-width` argument to calculate $g^{(n)}$ for each interval.

### 3.3.2 Intensity-Dependent Analysis

In many cases, there is a clear association between an emission state and its intensity.[45,46] As such, by characterizing the maximum and minimum emission intensities,

Listing 3.8: A method for calculating $g^{(n)}$ for photons arriving during intervals of various intensities.

```
def idgn(photons, window_width, intensity_bins, **gn_params):
    gns = [GN(gn_params) for _ in intensity_bins]

    window = Window(window_width)
    queue = list()

    for photons in photons:
        while True:
            if photon in window:
                queue.append(photon)
                break
            elif photon < window:
                break
            else:
                intensity = intensity_bins.index(len(queue))
                for photon in photons:
                    gns[intensity].push(photon)
                window.next()


    for gn in gns:
        gn.flush()

    return(gns)
```

we can define a range of intensity bins and keep track of the time-integrated $g^{(n)}$ for intervals of each intensity (see Listing 3.8).

In `photon_correlation`, intensity-dependent $g^{(n)}$ calculations are performed with `photon_intensity_dependent_gn`.

### 3.3.3 Fluorescence Lifetime and Intensity Distribution

Some quantum dots, particularly thick-shelled CdSe/CdS,[42] exhibit emission states of equivalent intensity but distinct lifetime. To characterize these dynamics, we can measure the mean arrival time for photons found within an interval, and correlate with the number of photons found in that interval to form what is known as a fluorescence lifetime and intensity distribution (FLID; see Listing 3.9).

FLID are calculated using `photon_flid`.

Listing 3.9: A method for calculating FLID for t3 photons.

```
def flid(photons, window_width,
         intensity_bins, lifetime_bins):
    hist = numpy.zeros(len(intensity_bins),
                       len(lifetime_bins))

    window = Window()
    time = 0
    counts = 0

    for photon in photons:
        while True:
            if photon in window:
                counts += 1
                time += photon.time
                break
            elif photon < window:
                break
            else:
                intensity = intensity_bins.index(counts)
                lifetime = lifetime_bins.index(time/counts)
                hist[intensity, lifetime] += 1
                time = 0
                counts = 0
                window.next()

    return(hist)
```

## 3.4 Examples of Usage

Each program in `photon_correlation` performs a specialized task, and any useful analysis is typically the result of some combination of operations. For example, to calculate the lifetime of data taken on a HydraHarp with 16 ps time resolution, use the following command:

```
picoquant --file-in data.ht3 | \
photon_gn --mode t3 --order 1 --channels 4 \
          --time 0,32768,524288 \
          --file-out data.ht3
```

The $2^{15}$ bins are set by the hardware, and the $2^{19}$ upper time limit is the product of 16 ps and $2^{15}$. This even division of time bins prevents aliasing of the integer arrival times (multiples of 16 ps).

To measure the $g^{(2)}$ of t3 data, up to 10 pulse separation:

```
picoquant --file-in data.ht3 | \
photon_gn --mode t3 --order 2 --channels 4 \
          --pulse -10.5,21,10.5 --time -400500,801,400500 \
          --file-out data.ht3
```

Measuring a number-resolved lifetime (see Chapter 6) is a matter of including a number-to-channels conversion:

```
picoquant --file-in data.ht3 | \
photon_number_to_channels | \
photon_gn --mode t3 --order 1 --channels 10 \
          --time 0,32768,524288 \
          --file-out data.ht3.number
```

These are only a few of the many analyses possible with `photon_correlation`. See Section 3.5 for a fuller description of the various tools, and how they may be used together.

## 3.5 Listing of Programs in `photon_correlation`

In the previous sections, we described the basic algorithms used to perform measurements of the photon stream. Here, we list the programs which serve as interfaces to these algorithms, and briefly describe their purpose. The output $g^{(n)}$ are all non-normalized (raw numbers of counts), unless otherwise specified. Normalization of these values must be performed externally.

**intensity_correlate** Input: intensity. Output: $g^{(2)}$ (normalized). See also: `photon_intensity_correlate`.

Performs the multi-tau correlation of the input intensity data to produce a normalized $g^{(2)}(\tau)$. This method works for any number of channels, and the parameters of the multi-tau algorithm (binning, registers, depth) may be modified. The default settings are chosen to match those found in an ALV-7004,[96] which is the correlation hardware used in our lab for PCFS.

**photon_bin_intensity** Input: t2, t3 records. Output: intensity

Calculates the effective intensity seen for each bin of a histogram, based on the bin definitions and the finite integration time. This is used for the explicit normalization of $g^{(n)}$ counts, accounting for the finite integration time and the true arrival times of the photons.

For t2 records these are determined for the time dimension, and for t3 records the pulse dimension is used. The output format is nearly equivalent to that of an intensity: the first two columns contain the bin definition and the remaining columns contain the counts found on each channel. Unlike intensity data the bin definitions may be floating-point numbers, representing the histogram bins defined for $g^{(n)}$.

**photon_correlate** Input: t2, t3 records. Output: correlation records. See also: `photon_histogram`.

Generates all permutations of $n$ photons for the input records. Optionally, specified limits of time (t2, t3) or pulse (t3) separation are used to suppress the generation of irrelevant correlations.

For t2 records, the output format is:

channel of photon 0, channel of photon 1, time delay of 1 and 0,
channel of photon 2, time delay of 2 and 0, ...

For t3 records, the output format is:

channel of photon 0, channel of photon 1, pulse delay, time delay
channel of photon 2, pulse delay, time delay ...

See Listing 3.3 for more details.

**photon_flid** Input: t3 records. Output: flid histogram

Generates a two-dimensional histogram of instantaneous intensity and mean arrival time for an input stream of t3 records. The output format contains the definitions of the arrival time and intensity histogram bins, as well as the width of the window (in number of pulses) used to measure these values. See Listing 3.9 for more details.

**photon_gn** Input: t2, t3 records. Output: folder containing $g^{(n)}$, intensity, number (t3), total counts, binned intensity (optional), list of options. See also: `photon_bin_intensity`, `photon_correlate`, `photon_histogram`, `photon_intensity`, `photon_intensity_dependent_gn`, `photon_number`.

This program combines many of the other programs into a convenient single-access point. Its primary function is to calculate the $g^{(n)}$ (non-normalized), and in addition to this it produces the intensity, photon number statistics (t3 only), the total number of records seen on each channel, the effective intensity needed for exact normalization (see `photon_bin_intensity`; not calculated by default), and an INI-style file containing the options used to generate these measurements.

Optionally, by passing a value to `--window-width`, the $g^{(n)}$ and number statistics are calculated for every fixed interval of time (t2) or pulse (t3). For example, to measure a lifetime ($g^{(1)}$) every 10 ms for a 1 MHz repetition rate, use 10000 (1 pulse per µs). For a time-dependent $g^{(n)}$, the first few rows of the output file contain the histogram bin definitions, and subsequent rows contain the window definition and the number of counts seen in each window.

**photon_histogram** Input: correlation records, t3 records. Output: $g^{(n)}$. See also: `photon_correlate`, `photon_gn`, `photon_intensity_dependent_gn`.

For specified time (t2, t3) and pulse (t3) bin definitions, this populates the histogram for the input records. If a record falls outside the specified limits or contains a photon outside the specified number of channels, an error is reported but the remaining records are processed.

For t2 records the $g^{(n)}$ is defined for $n \geq 2$, with output mimicking the correlation format:

channel of photon 0, channel of photon 1,
time delay (lower limit), time delay (upper limit),
channel of photon 2, ...
counts

For t3 records the $g^{(n)}$ is defined for $n \geq 1$. The $g^{(1)}$ is a lifetime, and t3 records

may be passed directly into `photon_histogram` with corresponding time bin definitions to produce output of the following format:

channel, time delay (lower limit), time delay (upper limit), counts

For $g^{(n\geq 2)}$, it is necessary to specify the histogram bins for pulse and time differences. The output mimics the correlation format:

channel of photon 0, channel of photon 1,
pulse delay (lower limit), time delay (upper limit),
time delay (lower limit), time delay (upper limit),
channel of photon 2, ...
counts

**photon_intensity** Input: t2, t3 records. Output: intensity. See also: `intensity_correlate`, `photon_bin_intensity`.

Given a definition for the window interval, determines the number of records which arrived in each window, on each channel. The output format is:

window (lower limit), window (upper limit), channel 0 counts, channel 1 counts, ...

**photon_intensity_correlate** Input: t2, t3 records. Output: $g^{(2)}$. See also: `intensity_correlate`, `photon_intensity`.

Combines the steps of intensity calculation and correlation, as would be accomplished separately by `photon_intensity` and `intensity_correlate`, respectively.

**photon_intensity_dependent_gn** Input: t2, t3 records. Output: $g^{(n)}$-like. See also: `photon_gn`.

Given a definition for a $g^{(n)}$ histogram, a window width, and intensity bins specified as the number of photons arriving in each window, this program produces the $g^{(n)}$ for photons associated with windows of various intensities. See Listing 3.8 for more details.

The output format is similar to a time-dependent $g^{(n)}$. The first few rows contain the histogram bin definitions, and subsequent rows contain the intensity bin definitions, the window width, the number of time windows associated with that intensity, and the number of histogram counts for those records.

**photon_number** Input: t3 records. Output: number/count pairs. See also: `photon_number_to_channels`

For t3 records, counts the number of pulses for which $n$ photons arrived, including pulses in which no photons arrived. The output is a series of pairs indicating the number of photons and the number of pulses after which that many photons arrived. This program does not suppress afterpulsing, as `photon_number_to_channels` does.

**photon_number_to_channels** Input: t3 records. Output: t3 records. See also: `photon_number`

For t3 records, this program counts the number of photons arriving after each given excitation pulse, and assigns those photons to virtual channels based on the number of photons and their order (see Section 3.2.3). This program limits each channel to a single photon per pulse. By default only the channel of each photon is modified, leaving the arrival pulse and time intact, but the relative time delay between photons may be produced by passing `--correlate-successive`. This is useful for revealing the dynamics of successive events (see Chapter 6).

**photons** Input: t2, t3 records. Output: t2, t3 records. See also: `photon_t3_offsets`, `photon_temper`

This auxilliary program implements mode conversions for photon records, typically as part of some time-shifting operation. For example, by providing an origin in time and a repetition rate, t3 records can be converted to their equivalent t2 records, and vice versa. Optionally, all photon events may be copied to a specified channel, which can be useful when calculating the total autocorrelation of a photon stream.

**photon_synced_t2** Input: t2 records. Output: t3 records

Given an input of t2 records, this program treats a specified channel as the sync channel, and outputs the equivalent t3 records. This is typically used to overcome the time resolution limitations of the t3 mode of hardware by using the higher-resolution t2 mode, explicitly recording the arrival time of every sync event. This program may also be used to simulate the start-stop mode (histogramming mode) of correlation hardware, by treating a true signal channel as the sync channel.

**photon_t3_offsets** Input: t3 records. Output: t3 records. See also: `photons`, `photon_temper`

When combining t3 data across several detection channels, it is vital to ensure that the relative timing of each channel is consistent. Typically this is handled during experimental alignment, but sometimes it is necessary to perform this adjustment in post-processing. This program combines the t3-to-t2, time offsetting, and t2-to-t3 conversion steps which would otherwise be performed with separate calls to `photons` and `photon_temper`.

**photon_temper** Input: t2, t3 records. Output: t2, t3 records. See also: `photons`, `photon_t3_offsets`.

This auxilliary program modifies individual TTTR records. For example, a particular detection channel may be removed, or a fixed offset of arrival time (t2, t3) or pulse (t3) may be applied for particular channels. For t3 records, afterpulsing may be removed by removing all but the first photon pulse channel, per pulse. Also for t3 records, a time gating may be applied to suppress photons arriving before a certain time, as needed for the method of Mangum et al.[98].

**photon_threshold** Input: t2, t3 records. Output: t2, t3 records.

Given a window width and minimum number of photons per window, emits only the records arriving during intervals with at least the specified intensity.

**photon_time_threshold** Input: t3 records. Output: t3 records. See also: `photon_number_to_channels`

In studying the number-resolved lifetime of nanocrystal emission, there are sometimes several timescales for the arrival time of the first photons (see Chapter 6). In order to determine whether the arrival statistics of the second photon are identical for early and late first-photons, this program divides photon pairs into four distinct channels. Channels 0 and 1 are the first and second photons, respectively, for pairs where the first photon arrived before the threshold time. Channels 2 and 3 are the first and second photons, respectively, for pairs where the first photon arrived after the threshold time.

## 3.6 Potential Improvements

As written, `photon_correlation` consists of a number of independent programs which perform the minimal operations necessary for a particular measurement. These are piped together to perform some more complex measurement, enabling the user to simply and visibly adjust the options for each step, and to introduce custom operations with ease. This is generally efficient for the user but is not always computationally efficient. For example, if `photon_t3_offsets` is used as part of a calculation, the cost of string-to-binary and binary-to-string conversions is actually a majority of the cost for the whole operation, and could more efficiently operate as a direct binary-to-binary conversion. Including all of these possible options in a single binary program is complex from a programmer's perspective but can save signficant computational time. This is actually why `photon_gn` exists: the cost of using `photon_correlate` and `photon_histogram` in succession is only a few percent, but for long calculations this is significant.

Each operation in `photon_correlation` is designed for maximal generality, to ensure that correlation, histogramming, and other routines will always work for the user. As a consequence, simple operations such as the measurement of $g^{(1)}$ and $g^{(2)}$ may have excessive overhead and the calculation may be greatly simplified by incorporating specialized routines. For example, the correlator iterates over all permutations for each tuple of $n$ photons, but specialized lookup tables for each order of correlation

could speed up the calculation significantly.

Similarly, while the various comma-separated value formats used in `photon_correlation` are reasonably human-readable and simple to parse, they are quite space-inefficient. For example, linearly-spaced histogram bins may be defined by their limits and the number of bins (as is used on the command line), and inclusion of these definitions in the output is sufficient to reproduce the bin definitions. Originally these formats were chosen for their ease of use, but in the future it would be wise to specify a number of efficient formats and write a corresponding programming interface which can be used for both calculations and analysis.

# Chapter 4

# Single-Molecule Photoluminescence Measurements of InAs/CdZnS Core/Shell Quantum Dots

## 4.1 Contributions

The nanocrystal sample was provided by QD Vision. The optical experiments were carried out by Raoul Correa and Thomas Bischof. The SNSPD system was built and maintained by Eric Dauler, Danna Rosenberg, and coworkers. The data were analyzed by Thomas Bischof and Raoul Correa.

The results described in this chapter are reported in Bischof et al. [45] and Correa [99].

## 4.2 Introduction

Colloidal semiconductor nanocrystals have attracted considerable attention due to their size-tunable optical properties, high emission quantum yield, and long-term stability.[100] A variety of materials have been successfully synthesized as nanocrystals with emission ranging from 400–5000 nm,[2,3] stoking interest in their use in a vari-

ety of applications, including light-emitting devices,[101–103] biological labeling,[50,104–108] and photovoltaics.[109,110] In particular, nanocrystals represent an orders-of-magnitude improvement in emission quantum yield over existing organic dyes as emitters of shortwave-infrared light[111] (SWIR; roughly 1000–3000 nm). Synthetic control over the exciton dynamics in SWIR-active nanocrystal materials such as PbS and InAs is not yet as thoroughly developed as it is for CdSe.

The understanding of the photophysics of CdSe nanocrystals has been aided by insights obtained using single-molecule spectroscopy, in which the effects of ensemble averaging are removed to extract knowledge of the dynamics of individual nanocrystals.[63] This understanding has also driven improvements in the quality of these materials.[107] Single-molecule methods to study effects such as blinking, multiexciton dynamics,[54] and spectral diffusion[51,112] have been implemented for visible-emitting nanocrystals using silicon single-photon avalanche photodiodes (SPAD). These detectors are insensitive to light below the band gap of silicon, such that only relatively blue-emitting nanocrystals of SWIR-active materials can be studied with conventional detectors.[113] Considerable effort has been put into developing new technologies for direct single-photon SWIR detection.

Presently, the best-performing technology for direct detection of SWIR photons is the superconducting nanowire single-photon detector (SNSPD).[114] In our previous report we described the first study of SWIR emission from individual nanocrystals of InAs/CdSe and PbS/CdS,[43] and noted several qualitative similarites to the photoemission dynamics of CdSe nanocrystals: the nanocrystals exhibited photoluminescence intermittency, and the autocorrelation of their emission yielded antibunching indicative of partial single-photon emission. These experiments demonstrated the potential of this technology for performing such sophisticated single-molecule studies of SWIR-emitting nanocrystals. We have now worked to extend the methods to study other aspects of the exciton lifecycle.

Here, we report a study of individual SWIR-emitting InAs/CdZnS nanocrystals from a single synthetic batch. We discuss the relationship between fluctuations in nanocrystal emission intensity and lifetime, and how different mechanisms of blinking

may give rise to such dynamics. We then use this intensity-dependent analysis to measure the intrinsic radiative lifetime of several nanocrystals. Finally, we use an improved photon correlation method to study multiexciton emission dynamics in these nanocrystals under moderate excitation flux.

## 4.3 Methods

The experimental apparatus used in this study is similar to the one described previously.[43] A 633 nm pulsed laser (PicoQuant, $\approx 100$ ps pulse duration, 1 MHz repetition rate) is used to excite a nanocrystal sample through a 100x oil-immersion objective (Nikon, NA 1.25). The emitted light is spectrally filtered (Thor Labs, 700 nm long-pass) and coupled into a single-mode optical fiber (SMF-28). Once in the fiber, the light is directed to a superconducting nanowire single-photon detector (SNSPD) composed of NbN on a silicon substrate. The SNSPD is illuminated through the silicon substrate, which acts as an additional long-pass filter in the optical path (at the 3 K operating temperature the silicon bandgap is 1.17 eV, or 1060 nm[115]). The four elements of the detector are read out in parallel using the time-tagged time-resolved (TTTR) mode of a PicoQuant HydraHarp. The overall detection system has $\approx 60$ ps timing jitter, 50 % detection efficiency, and registers 500 dark counts per second.

The sample of InAs nanocrystals was provided by QD Vision (InAs-016), and the synthetic details are described in the associated patent.[116] The nanocrystals in this sample consist of InAs cores with a CdZnS shell layer (90 % Cd, 10 % Zn). TEM images and an ensemble emission spectrum of the sample are available in Section 4.6.

Samples for optical microscopy were prepared by first diluting the concentrated nanocrystal solution with a 9:1 hexane:octane mixture, and then drop-casting the dilute solution onto No. 1 glass coverslips, in air.

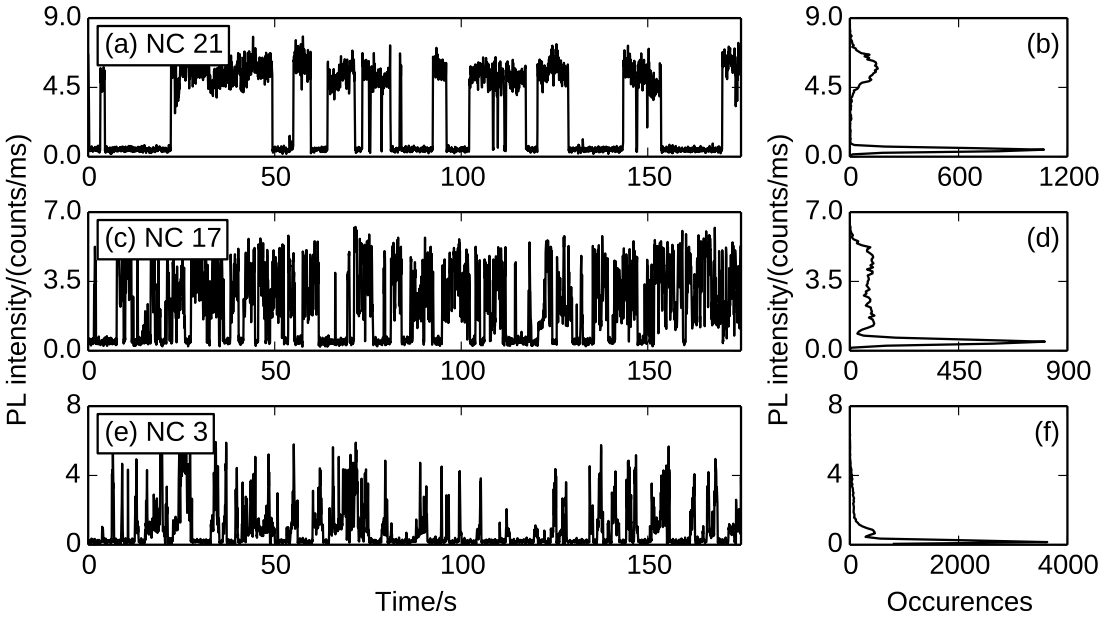


Figure 4-1: Representative emission dynamics from individual InAs/CdZnS nanocrystals, measured by integration over intervals of 50000 excitation pulses (50 ms). Each row presents the emission intensity of a single nanocrystal over time (**A**, **C**, **E**), as well as a histogram indicating the number of time bins during which each intensity was observed (**B**, **D**, **F**). The high-probability peak around 0.5 counts/ms in each histogram represents the dark counts of the SNSPD, and can be fit well with a Poisson distribution.

## 4.4 Results

Our previous study used CW excitation to study blinking dynamics and antibunching in the $g^{(2)}(\tau)$ of individual PbS/CdS nanocrystals, and the blinking dynamics of individual InAs/CdSe nanocrystals.[43] Here we use a pulsed excitation source, which allows us to correlate emission events with excitation events and enables the simultaneous study of emission intensity, emission lifetime, and antibunching.[63]

We studied the fluctuations in photoluminescence (PL) intensity from 24 individual InAs/CdZnS nanocrystals and found that all exhibited intermittency in some form (see Figure 4-1). Figure 4-1 shows three examples of blinking traces and intensity histograms that capture the breadth of behaviors observed. Some nanocrystals, such as NC 21 in Figure 4-1A–B, switched between states of high intensity ("on") and low intensity limited by the dark counts of the detector ("off"), akin to the binary blinking behavior studied extensively in CdSe.[117] Other nanocrystals, such as NC 17 in Figure 4-1C–D, exhibited well-defined states of intermediate intensity, often called "grey" states.[41,118,119] Still others, such as NC 3 in Figure 4-1E–F, fluctuated over a broad range of intensities.

We further characterized the blinking dynamics by correlating emission lifetime and intensity. Previous work on visible-emitting CdSe nanocrystals has demonstrated a range of emission lifetime dynamics. In some cases, researchers have observed stable grey states with a shorter emission lifetime, attributed to trion emission.[118,119] In another study, Galland et al.[41] identified two major classes of blinking mechanisms, which they denoted type A and type B. Type A blinking is characterized by a positive correlation of emission intensity and lifetime, and can arise, for example, when a time-varying non-radiative relaxation pathway competes for band-edge excitons. Type B blinking is characterized by a lifetime which is invariant with respect to emission intensity, and can arise if there is a time-varying non-radiative relaxation pathway that competes for the hot exciton, such that all excitons that reach the band edge emit with the same lifetime.

In our experiments here we observe both type A and type B blinking in InAs

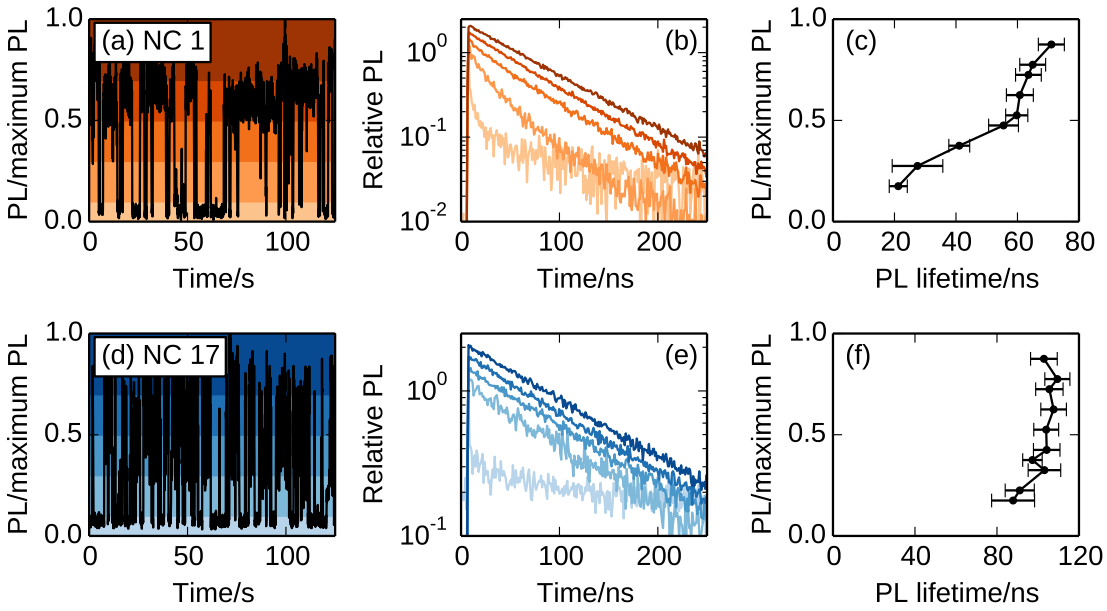


Figure 4-2: **A** The photons emitted by a nanocrystal can be identified as having been emitted during a period of a particular emission intensity. **B** Using intensity bounds meant to reveal high, intermediate, and low emission intensity, the emission lifetime of the nanocrystal can be determined (colors of curves correspond to the shaded regions of **A**). **C** By fitting the lifetime data for a variety of intensity bounds, we find that the lifetime may vary with emission intensity. Error bars in the lifetime represent the standard error for the least-squares fit. **D**–**F** The corresponding results for a different nanocrystal, showing intensity fluctuations which are not accompanied by lifetime fluctuations.

nanocrystals, as shown in representative traces in Figure 4-2A–C and Figure 4-2D–F, respectively. Figure 4-2A shows an intensity trace of NC 1, with the background color-coded to indicate the definitions of low, intermediate, and high intensity. These definitions are used to associate photons with an emission intensity, and the color-coded lifetimes in Figure 4-2B are formed by calculating the emission lifetime for photons emitted during periods of equivalent intensity. Qualitatively it is evident that the lifetime decreases with decreasing emission intensity. Figure 4-2C plots emission lifetimes as a function of intensity, where the lifetime is obtained by fitting the top half of the decay with a single exponential (error bars represent the standard error of the least-squares fit). Figure 4-2C clearly shows in this case that lifetime and intensity are correlated, and has been characterized as type A. Most of the InAs nanocrystals studied exhibited type A blinking.

Some of the nanocrystals studied did not exhibit type A blinking. Figure 4-2F shows that the emission lifetime and intensity of NC 17 appear to be independent. The emission lifetime even appears to be unchanged during emission from a grey state at 25 % emission intensity (see Figure 4-1C–D). This is unlike the faster lifetimes previously observed in some CdSe samples that exhibit grey state blinking, and that have been attributed to trion emission.[118,119] It instead most closely resembles type B blinking.[41]

We can extend our analysis of emission lifetime to extract the intrinsic radiative lifetimes of our measured InAs nanocrystals. To do so, we determine the emission lifetime for each nanocrystal using only the photons arriving during intervals when the nanocrystal emits at least 70 % of its maximum intensity, akin to Fisher et al.[46]. This threshold is chosen to obtain a reasonable balance of signal and contrast, that is to have enough photons to accurately represent the emission lifetime and to ensure that only photons from the maximum intensity states are sampled. For the nanocrystals studied, this yields well-defined single-exponential decays (see Figure 4-3A), which can be fit with single exponential functions to determine radiative lifetimes. As in previous studies on CdSe, we assume that the maximum intensity corresponds to emission with unity exciton emission quantum yield. We find wide variation in these radiative

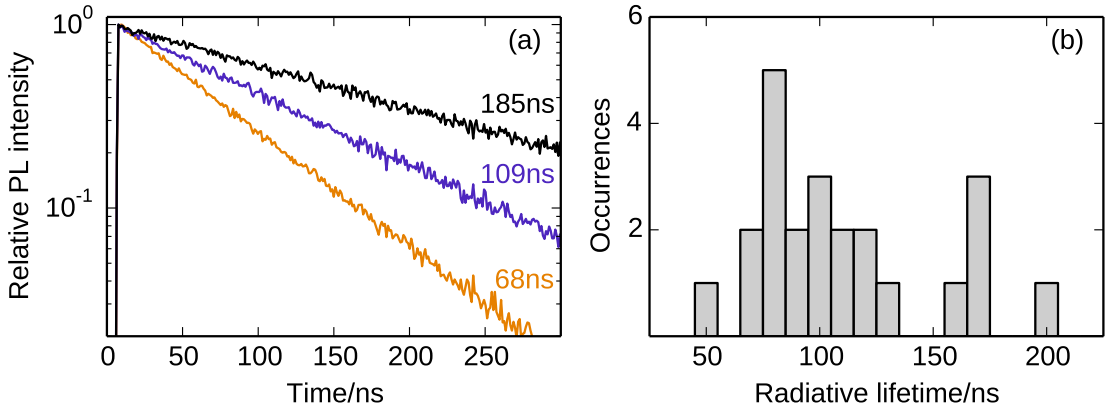


Figure 4-3: **A** PL lifetime data formed from photons arriving during intervals of high emission intensity for three different nanocrystals, assumed to represent the intrinsic radiative lifetime.[46] **B** The aggregate of the radiative lifetimes measured in this fashion for the nanocrystals in this study, showing the broad range of lifetimes observed.

lifetimes (50–200 ns, Figure 4-3B), which we attribute to a large polydispersity of nanocrystal structures and morphologies within the sample. In core-shell CdSe/CdS, the radiative rate varies with the size and shape of the nanocrystal core and shell, due to the variation in the overlap of the electron and hole wavefunctions.[120] This contrasts earlier work on CdSe/ZnS, in which the ZnS shell does not permit such asymmetric delocalization of the two charge carriers and each nanocrystal was found to have a roughly equivalent radiative lifetime.[46] The broad distribution of radiative lifetimes in our InAs/CdZnS sample indicates that the material has a quasi-type II electronic structure, such that structural heterogeneities lead directly to heterogeneity in radiative lifetime.[120]

If structural polydispersity gives rise to the distribution of radiative rates, it is reasonable to suspect that there should a corresponding distribution for the biexciton quantum yield.[120] We determine the biexciton emission quantum yield for the nanocrystals in this study by characterizing the extent of antibunching through a measurement of $g_0^{(2)}$.[54]

Previous treatments of the correlation of biexciton quantum yield and $g_0^{(2)}$ have relied on a low excitation flux and a clear temporal separation between peaks in the

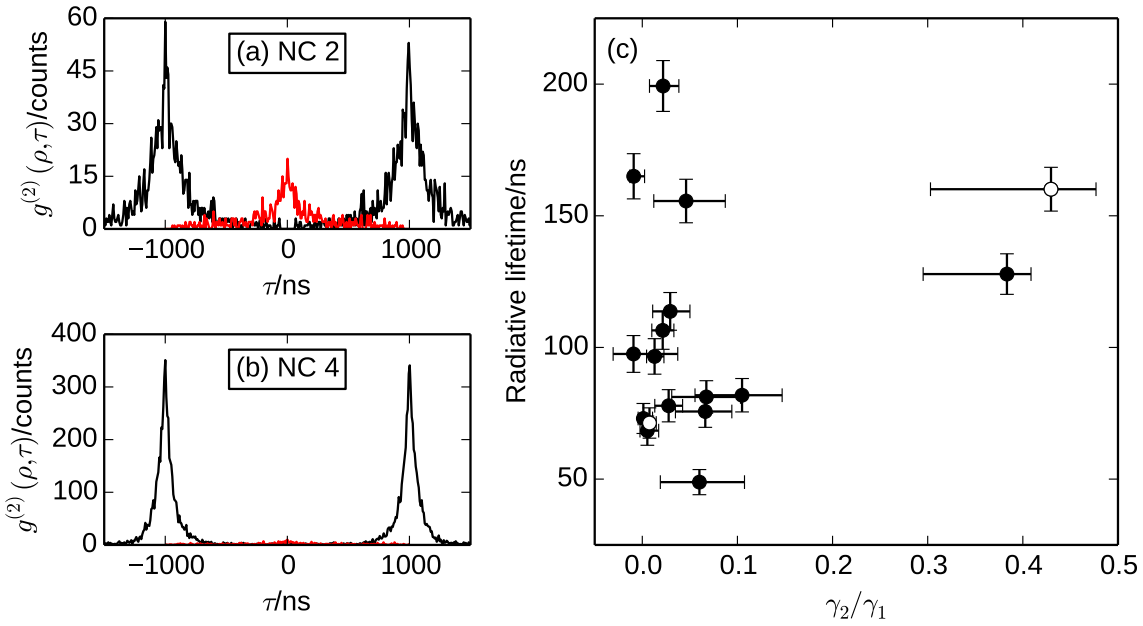


Figure 4-4: (a,b) Representative $g^{(2)}(\rho, \tau)$ from two different nanocrystal exhibiting a large (a) and small (b) $g_0^{(2)}$ (temporal bins are 8 ns). The red curves represent the center peak as identified by our pulse-resolved correlation method. (c) A scatter plot of the measured biexciton quantum yield ratio for each nanocrystal and its radiative lifetime, both calculated using only photons emitted during intervals of at least 70 % of the maximum intensity. The white-filled points correspond to the nanocrystals in (a) and (b). In total, 17 of the 24 nanocrystals yielded sufficient signal to measure $g_0^{(2)}$. The reported error for the lifetime is the standard error of the least-squares fit. For $\gamma_2/\gamma_1$, the error is estimated using the shot noise of $g_0^{(2)}$, the model in Equation (4.2), and effective excitation flux $\langle n \rangle$.

$g^{(2)}(\tau)$. In our case here these limits were not achievable, and this has motivated us to develop a more general treatment of the relationship between the biexciton quantum yield and $g_0^{(2)}$.

Due to the long emission lifetime of the nanocrystals studied (up to 200 ns), the use of a 1 MHz excitation source proved too fast to clearly temporally resolve the center and side peaks in $g^{(2)}(\tau)$. As such, a significant fraction of events contributing to the side peaks are counted toward the center, overestimating the fraction of biexciton emission events. If the emitted photons are instead associated with their excitation pulse, we obtain an equivalent photon correlation $g^{(2)}(\rho, \tau)$ in which we achieve maximal distinction of the two peaks. This analysis yields the optimal estimate of $g_0^{(2)}$ for a correlation measurement made using a pulsed excitation source, and our reported $g_0^{(2)}$ values are all determined in this fashion. We advocate this more general method even for cases where the temporal separation between peaks appears adequate.

In our microscope, photons emitted by a nanocrystal are directed to the detector with a single-mode optical fiber, which introduces some extra loss of overall system efficiency. These losses required us to operate at an excitation flux near single-exciton saturation in order to obtain a useful signal-to-noise ratio for measuring $g_0^{(2)}$. Under these conditions, the relationship between $g_0^{(2)}$ and emission quantum yield is not as well-established because we cannot assume operation in the low-flux limit.[54,97]

To account for these considerations, we have developed a model for the behavior of $g_0^{(2)}$ as a function of excitation flux and multiexciton quantum yield (see Chapter 2), akin to models presented by others.[54,97] If we assume that only the exciton and biexciton are emissive, that the exciton and biexciton emission quantum yields are constant, and that $\langle n \rangle$ is constant, we can use our model (Chapter 2) to obtain:

$$g_0^{(2)} = \frac{2\chi_2\gamma_2\gamma_1}{\left(\chi_2\left(\gamma_2+\gamma_1\right)+\chi_1\gamma_1\right)^2} \tag{4.1}$$

$$= \frac{2R\left(1-e^{-\langle n\rangle}-\langle n\rangle e^{-\langle n\rangle}\right)}{\left[\left(1-e^{-\langle n\rangle}-\langle n\rangle e^{-\langle n\rangle}\right)(1+R)+\langle n\rangle e^{-\langle n\rangle}\right]^2} \tag{4.2}$$

where $\langle n \rangle$ is the average number of excitons produced per pulse, $\chi_n$ is the probability

of producing $n$ excitons during an excitation pulse, and $R \equiv \gamma_2/\gamma_1$ is the ratio of the biexciton and exciton emission quantum yields ($\gamma_2$ and $\gamma_1$, respectively). This result requires several critical assumptions, which we discuss here.

First, our model treats the exciton and biexciton emission quantum yields ($\gamma_1$ and $\gamma_2$, respectively) as constant. To justify this, we can extend our earlier discussion of the radiative lifetime of nanocrystals to assert that photons emitted during intervals of high intensity represent high emission quantum yield. Thus the calculation of $g_0^{(2)}$ using only the photons emitted during these intervals allows us to assume that $\gamma_1 \approx 1$.[46,54] With $\gamma_1$ as a constant, the value of $\gamma_2$ can be considered the time-averaged value over the course of the experiment.

Second, our model treats only the emission of the exciton and biexciton. We presume that the triexciton is at least as subject to Auger recombination and other loss mechanisms as the biexciton, such that the triexciton quantum yield is no greater than that of the biexciton. If we do account for this state in our model, our measured value for $R$ is more closely of the sum of all multiexciton quantum yields, such that the measured value of $\gamma_2$ can be considered an upper bound for the true biexciton quantum yield.

Finally, we were unable to characterize the exact effective excitation flux used for each nanocrystal, which is the product of the excitation photon density and nanocrystal absorption cross-section. Characterization of the microscope allows us to set conservative upper and lower bounds for the value of $\langle n \rangle$. These bounds and the shot noise of $g_0^{(2)}$ set the error bars for the measurement of $\gamma_2$.

Taking these considerations into account, we determined $R$ for each nanocrystal using Equation (4.2) and compared the value with radiative lifetime of the nanocrystal, as shown in Figure 4-4C. In total, 17 of the 24 nanocrystals studied yielded sufficient bright-state signal to obtain a meaningful measure of $R$. While most of the nanocrystals show biexciton emission quantum yields between 1 % and 10 %, two outliers show significantly higher quantum yields of up to 43 %.

These results are not inconsistent with prior reports which have obtained exciton and biexciton emission lifetimes for InAs indicative of biexciton quantum yields of

far less than 1 %.[121,122] For the nanocrystals studied in this letter, such low quantum yields would manifest as a value indistinguishable from zero, and indeed several nanocrystals showed no detectable biexciton emission. Unlike ensemble methods, which report the average behavior for a sample, the method used here is most well-equipped to detect the distribution of biexciton quantum yields,[54,123,124] and we found a number of nanocrystals with biexciton quantum yield between 3 % and 10 %.

Overall, the observed range of biexciton quantum yields is consistent with the broad distributions reported previously for other materials.[54,123,124] Differences in the exact morphology and environments of individual nanocrystals clearly affect the efficiency of multiexciton emission; studies of CdSe/CdS nanocrystals have revealed a direct correlation of shell thickness with radiative lifetime and biexciton quantum yield.[75,124] The existence of biexciton emission with varying quantum yield suggests that this emission behavior may be controlled in an analogous way for InAs.

## 4.5 Conclusions

We have described a series of single-nanocrystal experiments carried out for a sample of SWIR-emitting InAs/CdZnS nanocrystals. We observed a variety of blinking dynamics in individual nanocrystals, including examples of type A and type B blinking. We measured the radiative lifetime for several InAs nanocrystals and found values ranging from 50–200 ns. We extended the analysis of $g_0^{(2)}$ to account for finite excitation flux and a low temporal separation of peaks in $g^{(2)}(\tau)$. We used this method to determine the biexciton emission quantum yield of several InAs nanocrystals, and found values ranging from 1 % to 43 %.

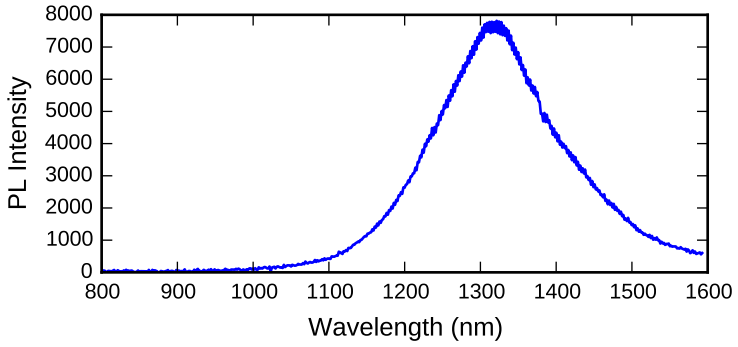


Figure 4-5: Emission spectrum of the InAs/CdZnS sample, excited using a 633 nm CW laser.

## 4.6 Supporting Information

### 4.6.1 Characterization of the InAs Sample

The sample of InAs/CdZnS nanocrystals was provided by QD Vision (batch InAs-016; 90 % Cd and 10 % Zn in the shell). We characterized its emission spectrum using a spectrometer equipped with an InGaAs linear array detector, as shown in Figure 4-5. We characterized its size polydispersity by TEM; several representative micrographs are shown in Figure 4-6. Qualitatively it is evident that the exact shape and size of the nanocrystals is not uniform, which we assert to be the primary source of heterogeneity in our optical experiments. To characterize this polydispersity, we manually defined the outlines of 1005 individual particles using ImageJ. For each particle, we measured the cross-sectional area and circumference, as shown in Figure 4-7. In that figure, the red trend line indicates the circumference-area relationship expected for a sphere, while the green trend line indicates this relationship for an ellipse with an aspect ratio of $\approx 2.4$ (eccentricity $\epsilon \approx 0.91$). The particles are not strictly ellipsoidal, but the trend lines demonstrates that they are in fact aspherical.

### 4.6.2 Estimation of $\langle n \rangle$

In these experiments, we sent 24 µW of 1 MHz excitation from a pulsed diode laser into the back of the 180 µm-working-distance sample objective. This objective is not

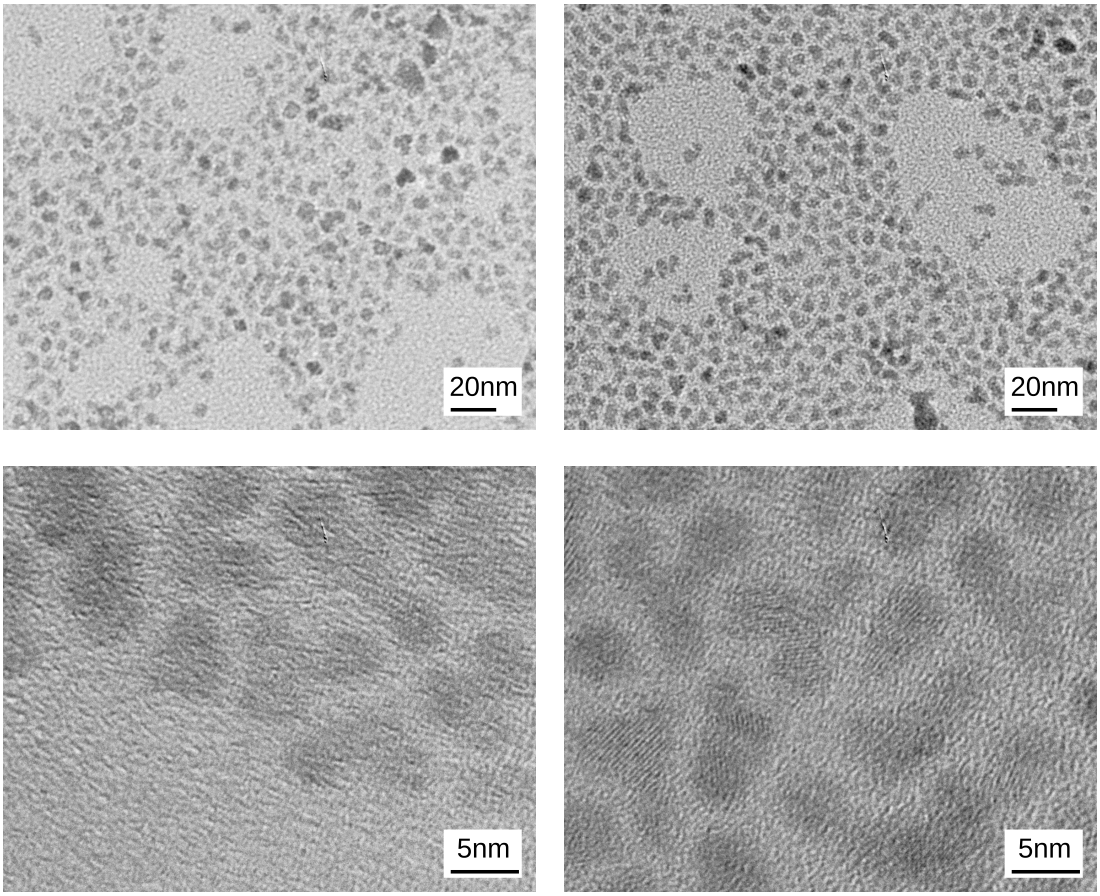


Figure 4-6: Representative TEM images of the InAs/CdZnS sample. A variety of particle shapes and sizes exist, including particles with well-defined grain boundaries.

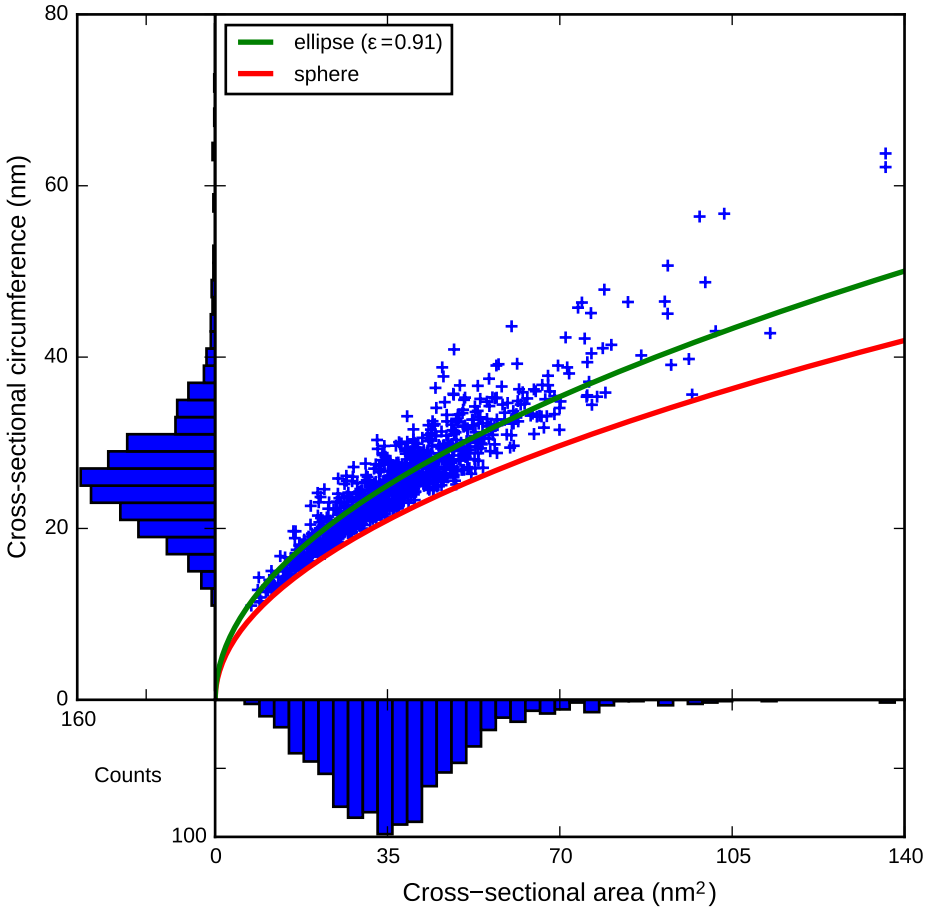


Figure 4-7: Cross-sectional areas and circumferences for 1005 particles, whose outlines were defined manually using ImageJ. The red trend line indicates the expected relationship for a sphere, while the green trend line indicates this relationship for an ellipse with an aspect ratio of $\approx 2.4$.

corrected for chromatic aberration, causing 633 nm light to focus about 10 µm closer to the objective than 1300 nm light. To compensate for this, we use a lens to defocus the excitation source and match its effective focal plane with that of the 1300 nm emitters. As a result, it is difficult to judge exactly how well-focused the beam is, and thus how large the effective spot size is for excitation.

As such, we can only estimate the excitation flux by setting reasonable upper and lower bounds. First, we can assume that we perfectly focus the excitation laser to a diffraction-limited spot to yield the maximum intensity achieved. This gives a full-width half-maximum beam waist of roughly $\lambda = 633\,\text{nm}$. Approximating the excitation as uniform through a circle of this diameter, we obtain roughly $8\,\text{mJ/cm}^2\text{/pulse}$, or $24 \times 10^{15}\,\text{photons/cm}^2\text{/pulse}$. With an absorption cross-section of roughly $1 \times 10^{-15}\,\text{photons/cm}^2$ (estimated using Yu et al.[125]), we find that $\langle n \rangle$ is likely to be no more than 24 per pulse. This is not strictly a meaningful value: this approximation assumes that each successive excitation is equally likely, but in reality the accessible transitions will be rapidly depleted at high flux. As such, the true distribution of exciton number will not be Poissonian but will instead be dominated by excitons and biexcitons. This number can be used as a rough estimate in our calculations to quantify the saturation of biexciton generation, which is what our form of the model achieves.

To estimate the lower bound, we can use the experimental data and the measured losses in the system. A typical nanocrystal emitted with maximum detected intensity of 7 photons/ms, or 0.007 photons/pulse. We estimate roughly 30 % collection efficiency at the sample objective, 90 % transmission through the long-pass filter, 20 % coupling efficiency at the single-mode fiber, and 50 % detection efficiency – with negligible geometric loss at the four channels – for an overall system efficiency of 2.7 % and a true photon rate of 0.3 photons/pulse (300 kphotons/s). Since the nanocrystal is at maximum intensity during these periods, this gives $\langle n \rangle \geq 0.3$.

We estimate $0.3 \leq \langle n \rangle \leq 24$ as the most conservative possible range of values. The microscope alignment and operation was consistent between experiments, and as such it is entirely reasonable to expect that the exact value of $\langle n \rangle$ was constant,

but its exact value is unknown. This range of $\langle n \rangle$ presented here is used to set the upper and lower limits of the estimated error for our measurement of the biexciton quantum yield.

# Chapter 5

# InAs Band-Edge Exciton Fine Structure

## 5.1 Contributions

This work was carried out in collaboration with Oscar Sandoval, a summer student at Lincoln Laboratory. Daniel Harris and Daniel Franke synthesized the nanocrystals. Matt Grein, Ryan Wilson, and Eric Dauler maintained the superconducting detector system used for photoluminescence measurements at Lincoln Laboratory. Greg Steinbrecher constructed the microscope. Thomas Bischof, Igor Coropceanu, and Oscar Sandoval analyzed the data.

## 5.2 Introduction

Semiconductor nanocrystals rarely, if ever, exhibit emission linewidths which are lifetime-limited. Instead, there are a number of linewidth broadening mechanisms which are relevant under various conditions, such as spectral diffusion,[51,126] charging,[51,127] and excitonic fine structure.[62,126–132] While spectral diffusion and charging are most likely photoinduced effects and thus can be modulated by the excitation rate of the nanocrystals, fine-structure broadening is fundamental to the photophysics of nanocrystals and most likely unavoidable. A complete understanding of the excitonic

energy landscape enables us to determine dephasing rates, linewidths, lifetimes, and other parameters essential to optical applications.

Here we discuss the relationship between the excitonic fine structure and the emission dynamics of InAs/CdS core/shell nanocrystals. At room temperature we find steady-state emission dynamics on order of 150 ns, and as the temperature is lowered we find that the relaxation is greatly slowed (1.9 µs at 3.6 K). We find that these emission dynamics are well-explained by a band-edge model including a pair of "dark" and "bright" excitonic states, separated in energy by 2.3 meV.

## 5.3 Methods

Nanocrystal cores were prepared following the method reported in Bruns et al.[133]. In this synthesis, 4 mmol indium(III) acetate (1.168 g), 16 mmol myristic acid (3.654 g), and 20 mL 1-octadecene (ODE) were added to a 100 mL round-bottom flask. This solution was heated under vacuum for 2 h. An argon atmosphere was then introduced and the solution was heated to 295 °C. Two injection syringes were prepared, one containing 0.244 mmol tris(trimethylgermyl)arsine[25] ($(TMGe)_3As$, 96 mg) and 4 mL tri-n-octylphosphine (TOP, 4 mL, and the other containing 0.72 mmol $(TMGe)_3As$ (332 mg), 1 mL TOP, and 4 mL ODE. The contents of the first syringe were injected rapidly once the solution had reached 295 °C. After 10 min, the contents of the second syringe were injected at a rate of 5 mL/h. This procedure yielded InAs cores with an absorption peak at 1031 nm, and an emission peak at 1074 nm. Based on existing size calibrations,[125] these cores have an inorganic diameter of 4.9 nm.

To add the epitaxial shell, 5 mL InAs QDs in hexanes (90 nmol 4.9 nm InAs QDs; 100 µmol InAs), 10 mL ODE and 7.5 mL oleylamine were added to a 100 mL round-bottom flask. This solution was degassed at room temperature, then 1 mL of 50 mM $Cd(oleate)_2$ in ODE were added (sufficient for one monolayer). The solution was heated to 100 °C under vacuum, then heated to 240 °C under nitrogen. Two ODE solutions, one containing 45 mM sulfur and the other 50 mM $Cd(oleate)_2$, were injected at a rate of 5 mL/h until 8.2 mL of each solution had been added. This procedure

yielded core/shell InAs/CdS nanocrystals with a 4.9 nm core, a five-monolayer thick shell, a photoluminescence peak at 1170 nm with a FWHM of 210 nm, and an emission quantum yield of 30 %.

To prepare nanocrystal films for optical experiments, we first diluted 1 µL stock InAs/CdS solution with 200 µL toluene and 200 µL PMMA/toluene (2 wt. %). We then deposited 30 µL of this diluted solution onto a 100 µm-thick Z-cut quartz substrate (MTI Corp.), and spun the sample at 5 krpm for 60 s to create a uniform film. This final sample was used without further treatment.

In our microscope, we mounted the sample in a closed-cycle helium cryostat (Montana Instruments, Cryostation). We performed our experiments in an epifluorescence configuration with a 100x near-infrared corrected long working distance objective (Mitutoyo, Plan Apo NIR), using a 640 nm pulsed diode laser for excitation (PicoQuant, LDH-P-C-640B), a 1000 nm short-pass dichroic filter (Thor Labs, DMSP1000), and a 700 nm long-pass emission filter (Thor Labs, FEL0700). The emission was collected into an SMF-28 fiber optic cable using an aspherical lens and directed into a cryostat containing a four-element superconducting nanowire single-photon detecotor (SNSPD), back-illuminated through a silicon substrate.[43,45,90] The SNSPD elements are read out using a PicoQuant HydraHarp.

## 5.4 Results

For our sample, we measured the emission lifetime at a variety of temperatures (3.6–295 K), with a laser repetition rate of 100 kHz. We verified the absence of multiexcitonic effects by confirming that the lifetime measured at one excitation power and another measured at a lower power were identical. The low repetition rate was chosen to prevent interpulse excitation at low temperatures, for which the emission lifetime is on the order of 2 µs.

The lifetime of emission at two representative temperatures is shown in Figure 5-1. At 295 K the emission is fit well as a biexponential with time constants of 49 ns and 175 ns. At low temperature the resolution of the fast component seen in Figure 5-1A

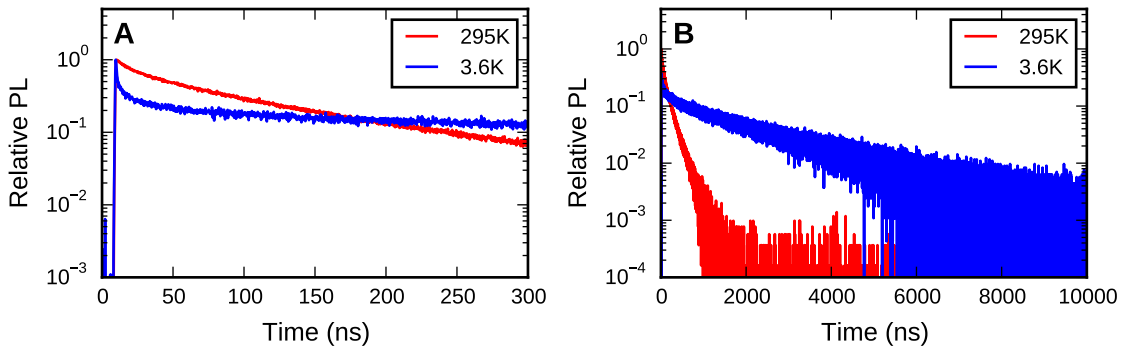


Figure 5-1: Emission lifetime of InAs/CdSe nanocrystals at 3.6 K and 295 K. **A** The emission lifetime of the film at 3.6 K (blue) and 295 K (red). **B** The same data, shown on a longer timescale to demonstrate the 1.9 µs low-temperature lifetime. All data are normalized to the maximum number of counts detected in a histogram bin.

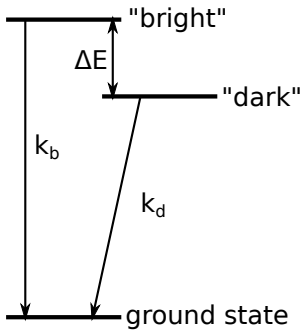


Figure 5-2: The standard three-state band-edge excitonic fine structure model.

is limited by the instrument response function (laser pulse duration ≈ 100 ps, detector jitter ≈ 60 ps), and the remaining signal is fit well as a biexponential (130 ns, 1.9 µs).

Prior reports[60,128–130,134,135] have suggested that the variability in emission lifetime is to the presence of multiple excitonic fine-structure states. In this model (Figure 5-2), the two lowest-lying excitonic states are a "dark" state, which is spin-forbidden from direct radiation, and a "bright" state, which is spin-allowed. The dark state is lower in energy, on the order of 3 meV for several binary materials.[60] At room temperature both states are approximately equally populated, such that emission primarily occurs through the bright state, but at low temperature only the dark state has significant thermal population. In both cases this manifests as a steady-state emission lifetime defined by the state populations and their relaxation rates (we

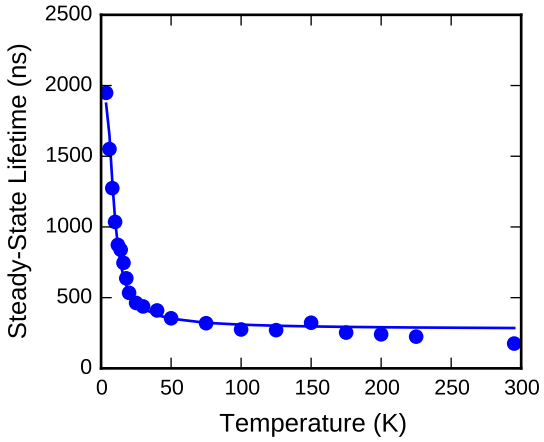


Figure 5-3: The steady-state lifetime of InAs nanocrystal emission as a function of temperature. The solid line is the fit to Equation (5.1).

assume thermal processes are fast relative to exciton recombination):[60]

$$k = f_b k_b + f_d k_d = \frac{k_b e^{-\beta \Delta E} + k_d}{e^{-\beta \Delta E} + 1} \tag{5.1}$$

Fitting this three-parameter model to the temperature-dependent steady-state lifetime, we obtain $k_b = 150\,\text{ns}$, $k_d = 1.9\,\mu\text{s}$, and $\Delta E = 2.3\,\text{meV}$ (Figure 5-3). The bright-state lifetime is comparable to reports on indvidual nanocrystals of comparable size.[45] The energetic splitting is consistent with that measured previously by photoluminescence methods[60] and ultrafast methods,[134] where it was attributed to the confined acoustic phonon energy of the nanocrystal. The agreement between transient oscillatory behavior and an equivalent splitting in state energies led Oron et al.[60] to conclude that all of the materials they studied (CdSe, InAs, PbSe, and CdTe) exhibited the same effective band-edge fine structure, with similar acoustic phonon energies.

These extracted relaxation rates are consistent with the dynamics observed in the PL transient. To fully model the PL transient we introduce the rate $k_{d \leftarrow b}$ for relaxation from the bright state to the dark state (the inverse rate is $k_{d \leftarrow b} e^{-\beta \Delta E}$, to preserve the Boltzmann distribution of population). Estimating this rate to be on the order of 25 ps,[129] we obtain an initial rapid decay consistent with our transient

data, the measurement of which is limited by the finite duration our laser pulse ($\approx 100\,\mathrm{ps}$) and the timing jitter of the detectors ($\approx 60\,\mathrm{ps}$). At intermediate times the kinetic model deviates from the data, but this can be explained by the existence of a distribution of relaxation rates,[129] most readily explained as the result of structural polydispersity of the nanocrystal sample.[45] In principle it is possible to extract an estimate of this distribution from the ensemble data, but a more precise measurement can be achieved by instead measuring the lifetimes of individual molecules.

## 5.5 Conclusions

We measured the temperature-dependent lifetime of a sample of InAs/CdSe quantum dots, and found that the steady-state relaxation rate is consistent with the excitonic fine-structure model of a bright and dark state coupled by acoustic phonons. We obtain a bright-state lifetime of 150 ns, a dark-state lifetime of 1.9 µs, and a splitting energy of 2.3 meV, which are consistent with previous reports. The relaxation rates and energetic splitting of these states are also consistent with the emission dynamics before the exciton population reaches the steady-state.

## 5.6 Acknowledgements

This work is sponsored by the Assistant Secretary of Defense for Research & Engineering under Air Force Contract #FA8721-05-C-0002. Opinions, interpretations, conclusions and recommendations are those of the author and are not necessarily endorsed by the United States Government.

# Chapter 6

# Emission Dynamics and Statistics of CdSe Multiexcitons

## 6.1 Contributions

The nanocrystal samples studied were provided by: QD Vision; Ou Chen, Yue Chen, Igor Coropceanu, and Aurelio Rossinelli (Bawendi Group, MIT); Igor Fedin and Chunxing She (Talapin group, University of Chicago). Microscopy data were collected by Thomas Bischof and Justin Caram. The data were analyzed by Thomas Bischof.

## 6.2 Introduction

The majority of research on the optical properties of colloidal semiconductor nanocrystals involves the study of monoexcitonic dynamics and statistics. The monoexcitonic description is largely sufficient for understanding the general dynamics of nanocrystal emission, such as the emission lifetime, blinking, and emission spectrum, but all nanocrystals also exhibit some number of multiexcitonic states. These multiexcitonic states complicate the use of nanocrystals as gain media[136–142] and are implicated in various blinking mechanisms,[41,42,47–49,118,127,143–148] but generally remain understudied due to the difficulties associated with isolating their emission.

Recently, a variety of number-resolved spectroscopies[54,149] have been developed which supplement transient and spectral methods.[52,145,150,151] With number-resolved spectroscopies we can measure the statistics of emission after individual pulses of excitation, which enables the unambiguous measurement of biexciton quantum yield[54] or lifetime.[149]

In this Chapter, we discuss the general theory of number-resolved spectroscopy, and its application to the study of nanocrystal emission. We use second- and third-order spectroscopies to resolve the triexciton, biexciton, and monoexciton dynamics and statistics of CdSe quantum dots. We then study the emission from individual CdSe/CdS core/shell nanoplatlets and thick-shell CdSe/CdS quantum dots, and find evidence for the existence of a spatially-separated biexcitonic state.

## 6.3 Methods

Several colloidal nanocrystal samples were studied: QD Vision red-emitting quantum dots, thin-shell CdSe/CdS quantum dots, thick-shell CdSe/CdS quantum dots, CdSe/CdS/ZnS quantum dots, and 4CdSe/3CdS nanoplatelets. See Section 6.6.1 for more information about these samples.

Samples for microscopy were produced as follows: 1 µL of stock nanoparticle solution in hexanes was diluted to 100 µL with toluene. From this solution, 1 µL was diluted to 100 µL with toluene. To this final solution was added 33 µL of 4 % (by weight) poly(methyl methacrylate) in toluene (PMMA), though for some samples we did not include this PMMA solution. The final dilute nanoparticle/PMMA solution was spin-coated onto a No. 0 glass coverslip by depositing 30 µL onto the coverslip, then spinning at 5 krpm for 60 s. The prepared coverslip was then attached face-down to a glass slide with UV-curing epoxy, and cured for about 10 min. The resulting microscopy sample has an open area of pristine film, protected from the atmosphere by the epoxy.

To collect emission from individual nanoparticles, we used a home-built confocal microscope. For excitation we used pulsed diode lasers (PicoQuant, LDH-C-400

(400 nm) and LDH-P-F-A-530-B (532 nm)). The laser emission is delivered to the setup using single-mode fiber-optic cables, then colimated for free-space use. As a dichroic we used either a 425 nm long-pass (Thor Labs, DMLP425) or 535 nm long-pass dichroic filter (Chroma Technology Corp, ZT532rdc-3). We used a 100x oil immersion objective (Nikon, NA 1.25), mounted onto a three-axis piezo stage for confocal epifluorescence scanning (Physik Instrumente, P-517.3CL). The emission is directed through a 50 µm pinhole using a 1-to-1 telescope with two 100 mm focal-length visible achromats (Thor Labs).

The emission is then filtered using either a 425 nm long-pass filter (Edmund Optics) or a 532 nm notch filter (Chroma Technology Corp, ZET532NF). The filtered emission is sent through three non-polarizing cube 50:50 beamsplitters (Thor Labs), yielding four beams of equal intensity. Each of the four beams is passed through a 100 mm focal-length visible achromat (Thor Labs) and focused onto single-photon avalanche photodiodes (Perkin-Elmer, SPCM-AQR-13). After the first beamsplitter, cold mirrors (Thor Labs, M254C45) are used as steering mirrors to suppress optical cross-talk between the SPADs (see Appendix A.2.1). All lenses and beamsplitters have visible anti-reflection coatings (400–700 nm).

The four detection channels are read out using a PicoQuant HydraHarp 400. Photon arrival times are recorded using t3 mode, which identifies the detection channel, the excitation pulse number, and the arrival time to the excitation pulse for each photon. These data are processed with custom C and Python software (see Chapter 3).

## 6.4 Results

The emission from the nanocrystal sample results from several different sources. The nanocrystal monoexciton emission is the dominant signal and generally defines the apparent emission dynamics, particularly the instantaneous emission intensity. Along with the monoexciton emission there is some biexciton and other multiexciton emission, which is typically much lower in count rate due to the Poissonian excitation statistics and the low quantum yield of these states.[54] We also find some autofluores-

cence from the coverslip, excess precursors, or glass-forming polymer, which together tend to form the most intense source of background. Some amount of laser emission leaks through the filters, and for pulsed excitation this can be detectable even at low count rates due to its short lifetime. Dark counts give a uniform background of a known count rate. Finally, all detection events have some probability of producing afterpulsing, depending on the photon energy and count rate.

We are interested in extracting the photon arrival events associated with multi-exciton emission, in order to characterize the statistics and dynamics of these states. Previously, the statistics of biexciton emission have been studied through photon correlation methods,[54,81] which identify biexcitonic emission by noting that pairs of photons generated by a single emitter after a single excitation pulse are associated with biexciton emission. Further work extended this idea to directly measure the dynamics of biexciton and exciton emission by identifying the individual photons in these pairs.[120,148,149,152] Here, we implement both methods for pulse-resolved data, and examine the emission dynamics of the triexciton and biexciton for CdSe quantum dots and nanoplatelets.

To generate the lifetimes of sets of photons, which we call the Photon Number Resolved Lifetime (PNRL$^{(n)}$; $n$ photons, see Figure 6-1), we begin by collecting emission from a molecular sample and record the photon arrival events in t3 mode, such that we retain knowledge of the originating excitation pulse in addition to the relative arrival time. This incoming photon stream is mapped onto several distinct virtual channels depending on the number of photons which were detected after a single excitation pulse, such that each virtual channel uniquely identifies the number and arrival order of the detected photons. We suppress detector afterpulsing by accepting only the first photon to arrive on a given detection channel (Figure A-6), such that our four-detector apparatus may detect zero to four photons after a single excitation pulse. A more standard apparatus with two detectors may detect up to two photons after a single excitation pulse. An example implementation of the algorithm is given in Listing 3.6.

Before analyzing the emission from an individual nanocrystal, we must develop

our understanding of how independent sources of emission contribute to the $\mathrm{PNRL}^{(n)}$ signal. Consider an ensemble of $n$ single-photon emitters, each with the same emission probability density $p(\tau)$. We experimentally measure $np(\tau)$ through the one-photon lifetime $g^{(1)}(\tau)$, which gives us the probability density of detecting an emitted photon, per unit time, per pulse.

We can precisely predict the form of $\mathrm{PNRL}^{(n)}(\tau)$ using $p(\tau)$. Assuming a detection rate $\langle\Gamma\rangle \ll 1$, for one-photon detection events we obtain:

$$\mathrm{PNRL}^{(1,1)}(\tau) \approx np(\tau) = g^{(1)}(\tau) \tag{6.1}$$

This low detection-rate limit allows us to neglect the contributions of multi-photon events, which we can account for separately.

Extending this to two-photon events, we note that pairs of photons are emitted by independent sources, such that there is no natural ordering to their emission. Instead, $\mathrm{PNRL}^{(2)}$ imposes temporal order on the natural distribution, yielding modified effective distributions:

$$\mathrm{PNRL}^{(2,1)}(\tau) \approx np(\tau)\left[(n-1)\int_{\tau}^{\infty} p(t)\,dt\right] \tag{6.2}$$

$$\mathrm{PNRL}^{(2,2)}(\tau) \approx \left[n\int_{0}^{\tau} p(t)\,dt\right](n-1)\,p(\tau) \tag{6.3}$$

Equation (6.2) may be read as the joint probability of detecting a photon at time $\tau$ from one of $n$ emitters, followed by another photon any time later from one of the other $n-1$ emitters. Similarly, Equation (6.3) is the joint probability of detecting a photon before $\tau$ from one of $n$ emitters, and another at $\tau$ from one of the other $n-1$ emitters. The sum of Equations (6.2) and (6.3) is proportional to $p(\tau)$: our imposition of time-ordering does not affect the number-insensitive distribution.

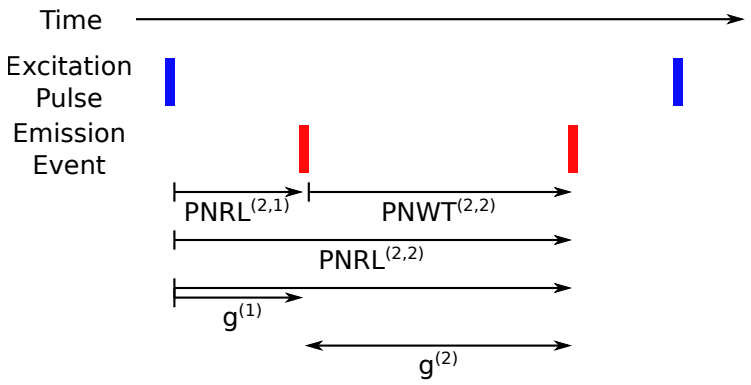


Figure 6-1: A depiction of the number-resolved spectroscopies used in this Chapter.

For three-photon events we obtain:

$$\mathrm{PNRL}^{(3,1)}(\tau) \approx n(n-1)(n-2)\,p(\tau)\left[\int_{\tau}^{\infty} p(t)\,dt\right]^2 \tag{6.4}$$

$$\mathrm{PNRL}^{(3,2)}(\tau) \approx 2n(n-1)(n-2)\left[\int_{0}^{\tau} p(t)\,dt\right] p(\tau)\left[\int_{\tau}^{\infty} p(t)\,dt\right] \tag{6.5}$$

$$\mathrm{PNRL}^{(3,3)}(\tau) \approx n(n-1)(n-2)\left[\int_{0}^{\tau} p(t)\,dt\right]^2 p(\tau) \tag{6.6}$$

We can validate Equations (6.2) to (6.6) by comparing the modeled $\mathrm{PNRL}^{(n)}$ to the experimental values for an ensemble of emitters, realized as a semi-dense film of quantum dots (thin-shelled CdSe/CdS, synthesized by the method of Chen et al.[107]. See Section 6.6.1). In Figure 6-2A we find the $\mathrm{PNRL}^{(1)}$ signature for this sample, which we have normalized by the detection rate to yield a histogram in units of counts per bin, per pulse. Applying our model for two-photon events, we numerically obtain the dashed lines of Figure 6-2B, which impeccably reproduces the experimental values. Likewise, our model for three-photon events precisely reproduces the experimental result in Figure 6-2C. Thus, given independent sources of emission we can predict their exact contribution to $\mathrm{PNRL}^{(n)}$.

For nanocrystal data, the absolute arrival times measured by $\mathrm{PNRL}^{(n)}$ are the convolution of the underlying emission distributions. For example, when a biexciton is formed the first photon is emitted at a rate set by the biexciton lifetime, and once this first relaxation occurs the remaining monoexciton may emit. Thus the apparent

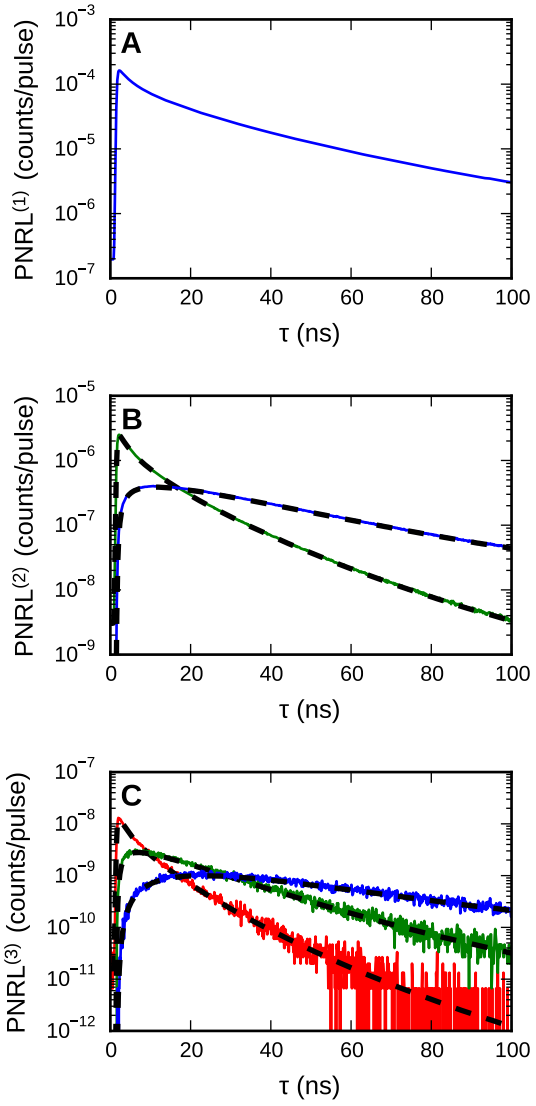


Figure 6-2: Experimental and modeled $\mathrm{PNRL}^{(n)}$ signals for an ensemble of quantum dots. **A** The measured $\mathrm{PNRL}^{(1)}(\tau)$, normalized to the count rate per histogram bin, per pulse. **B** The measured $\mathrm{PNRL}^{(2,1)}(\tau)$ (green) and $\mathrm{PNRL}^{(2,2)}(\tau)$ (blue), and the values predicted by Equations (6.2) and (6.3) (dashed black line). **C** The measured $\mathrm{PNRL}^{(3,1)}(\tau)$ (red), $\mathrm{PNRL}^{(3,2)}(\tau)$ (green), and $\mathrm{PNRL}^{(3,3)}(\tau)$ (blue). The predictions of Equations (6.4) to (6.6) are given as the dashed black lines.

monoexciton lifetime measured by $\mathrm{PNRL}^{(2,2)}$ is the convolution of the biexciton and monoexciton physics, and we instead wish to measure the delay in time between these photons. This is equivalent to studying the shape of $g^{(2)}(0,\tau)$. For clarity at higher orders, we will call this the photon number-resolved waiting time (PNWT), which may be modeled for a given distribution as follows:

$$g^{(2)}(0,\tau) \propto \mathrm{PNWT}^{(2,2)}(\tau) = \int_0^\infty p(t)\, p(t+\tau)\, dt \tag{6.7}$$

Returning now to single-nanocrystal measurements, we wish to extract the single-molecule contribution to number-resolved measurements. This is complicated by the presence of multiple emissive states for the nanocrystal and the existence of significant background signal. To account for the different nanocrystal states, we begin by measuring the emission intensity for a single quantum dot over time (QD Vision), as shown in Figure 6-3A. From this we identify ranges of intensity corresponding to the bright state (red) and to background (orange). Using photons arriving during those intervals, we measure the emission lifetime $g^{(1)}$ as shown in Figure 6-3B. We assume that the bright periods largely contain nanocrystal emission, while the dark periods largely contain photons from independent sources, such as background emission and dark counts. As such, the bright emission is the sum of the dark emission and the dot emission.

Measuring the number-resolved distributions for emission from the bright state, we obtain the solid curves of Figure 6-3C–D. Assuming that the the measured background contains negligible nanocrystal emission, we can apply the model of Equations (6.2) and (6.7) to obtain the background shown as the dashed black curves. Removal of this background leaves only the signal generated by the nanocrystal, as shown in Figure 6-3E–F. It is essential to perform this background correction step, as the long-lived signal might otherwise be attributed to exotic emissive states.

For this nanocrystal, we observe biexciton emission dynamics consistent with monoexponential decay convolved with the instrument response function, with a lifetime of 1.1 ns. For the monoexciton which remains after the biexciton decay, we observe

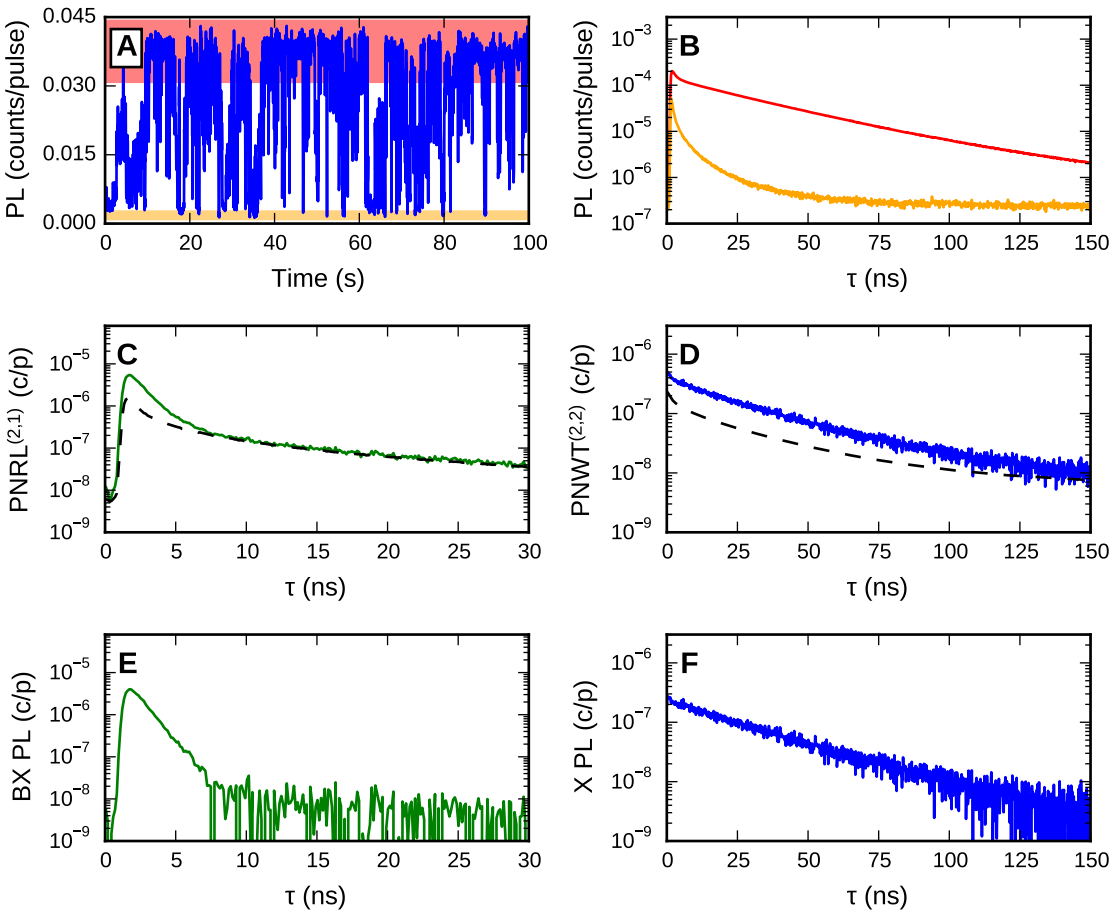


Figure 6-3: The process of extracting the emission lifetime of biexcitons and the subsequent monoexcitons they produce. **A** The intensity of emission from the nanocrystal (QD Vision quantum dot), with intervals of high (red) and low (orange) intensity noted. **B** The single-photon lifetimes measured during intervals of high (red) and low (orange) intensity. **C** $\mathrm{PNRL}^{(2,1)}$ as measured during intervals of high intensity (green), with the estimated background (dashed black line). **D** $\mathrm{PNWT}^{(2,2)}$ as measured during intervals of high intensity (blue), with the estimated background (dashed black line). **E** The lifetime of biexciton emission, and **F** that of the subsequent monoexciton, with the background removed. All lifetime data have 128 ps bins.

monoexponential emission with a lifetime of 25 ns. Because the emission arises from the bright state, we can assume that the monoexciton quantum yield is unity and thus its measured lifetime is the radiative lifetime.[46] The biexciton radiative rate is one quarter that of the exciton,[152] and if we assume that the measured biexciton lifetime is the product of the biexciton quantum yield and the radiative rate, we estimate the biexciton quantum yield $\gamma_2$ to be 18(6) %. Comparing this to the more conventional statistical measure of $g_0^{(2)}$,[54] we obtain $\gamma_2 = 18.73(3)$ % (the $g_0^{(2)}$ measurement is far more precise because its error is a result of shot noise and not fitting). We conclude that, for this nanocrystal, biexcitons are generated following the Poisson distribution, and their relaxation is completely described as the band-edge competition of radiation and Auger-like recombination. Also, the monoexciton generated after a biexciton relaxation is indistinguishable from a monoexciton produced by one-photon excitation ($\gamma_{2,1} = \gamma_{1,1}$).

Next, we measure the dynamics and statistics of triexciton emission. To measure triexciton emission statistics, we can extend the ideas of Nair et al.[54] to higher order, as discussed in Chapter 2. For $g^{(3)}(\rho_1, \rho_2)$ there are three distinct types of correlation events. When three photons arrive after a single pulse they contribute to the "center" peak, which is $G_3$ ($g^{(3)}(0,0)$). Events where two photons arrive after one pulse and a third arrives after another pulse are found along the "diagonal", and go as $G_2G_1$ ($g^{(3)}(0, \rho \neq 0)$, $g^{(3)}(\rho \neq 0, \rho \neq 0)$, and $g^{(3)}(\rho, \rho)$ for $\rho \neq 0$). Finally, there is an "off-diagonal" peak representing the arrival of three photons after three different excitation pulses, which grows as $G_1^3$ ($g^{(3)}(\rho_1, \rho_2)$ for $0 \neq \rho_1 \neq \rho_2 \neq 0$). These symmetries are readily visualized in Figure 6-4.

In a method analogous to $g_0^{(2)}$, we can extract the triexciton quantum yield $\gamma_3$ from experimental data by measuring $g_0^{(3)}$:

$$\begin{aligned} g_0^{(3)} \equiv & \frac{G_3}{G_2 G_1} \\ = & \frac{6\chi_3\gamma_3\gamma_2\gamma_1}{\left[2\left(\chi_3\left(\gamma_3\gamma_2 + \gamma_3\gamma_1 + \gamma_2\gamma_1\right) + \chi_2\gamma_2\gamma_1\right)\right]\left[\chi_3\left(\gamma_3 + \gamma_2 + \gamma_1\right) + \chi_2\left(\gamma_2 + \gamma_1\right) + \chi_1\gamma_1\right]} \end{aligned} \tag{6.8}$$

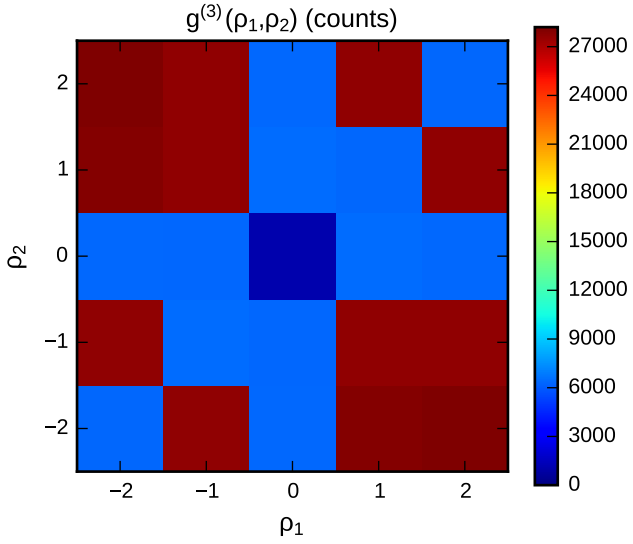


Figure 6-4: $g^{(3)}$ for a QD Vision quantum dot. The dark blue peak is the "center," corresponding to three-photon emission. The light blue peaks are the "diagonal," corresponding two a pair of two-photon and a one-photon event. The red peaks are the "off-diagonal," and result from three one-photon events.

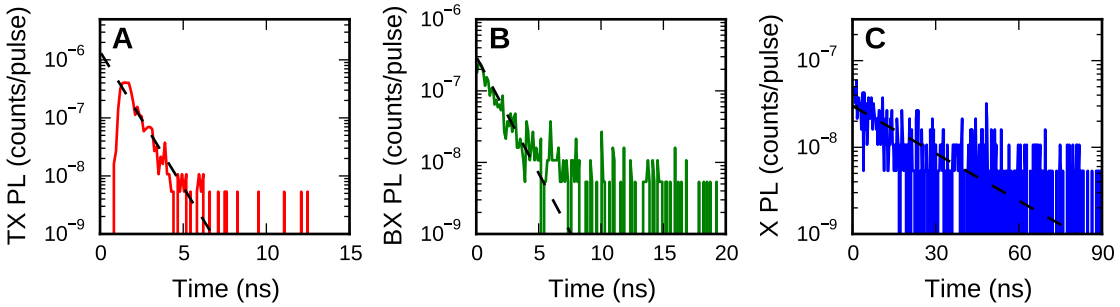


Figure 6-5: **A** Triexciton, **B** biexciton, and **C** monoexciton emission lifetimes for a QD Vision quantum dot. The black curves are single-exponential fits with lifetimes of 940 ps, 1.3 ns, and 24 ns, respectively. Bin widths are 128 ps, 128 ps, and 256 ps, respectively.

Here we have treated multiexcitons up to and including the triexciton, assuming that the biexciton which remains after a triexciton relaxes is identical to that produced through two successive excitations ($\gamma_{3,2} = \gamma_{2,2}$). Assuming Poissonian excitation, in the limit of low flux we obtain:

$$\lim_{\langle n \rangle \to 0} \frac{G_3}{G_2 G_1} = \frac{\gamma_3}{\gamma_1} \tag{6.9}$$

Applying this result to the same nanocrystal as Figure 6-3, we measure $g^{(3)}$ (Figure 6-4) and obtain $\gamma_3$=0.16(1). This apparent quantum yield is only slightly less than that of the biexciton, suggesting that the introduction of the extra carrier does not introduce significantly more Auger recombination. The similarity also suggests the idea that the triexcitonic emission does not necessarily result from the relaxation of the 1 P hole, but instead from the relaxation of the 1 S band-edge biexciton carriers. This partitioning may be studied through spectrally-resolved $g^{(3)}$ (see Chapter 8), but for now we will focus on our spectrally-integrated measurements.

We can also measure the dynamics of triexciton emission for our nanocrystal, as shown in Figure 6-5. From these data, we measure a triexciton lifetime of 940 ps (not IRF-limited, see Figure 6-9), a biexciton lifetime of 1.3 ns, and a monoexciton lifetime of 24 ns. The biexciton and monoexciton lifetimes agree with the values measured through two-photon emission, within uncertainty. Thus we conclude that the biexciton which remains after triexciton emission is equivalent to a biexciton formed through by two successive excitations, and that the monoexciton which remains after that biexciton relaxes is equivalent to other monoexcitons ($\gamma_{3,2} = \gamma_{2,2}$, $\gamma_{3,1} = \gamma_{2,1} = \gamma_{1,1}$).

For this QD Vision quantum dot, we have demonstrated that, when the nanocrystal is in a bright emission state, all states with the same number of excitons are equivalent and relax with monoexpontial dynamics. Furthermore, biexciton relaxation is completely described as the competition of the radiative channel with some fixed non-radiative rate. In this bright state, the quantum dot has a triexciton quantum yield of 16(1) % with 940 ps lifetime, and a biexciton quantum yield of 19 % with

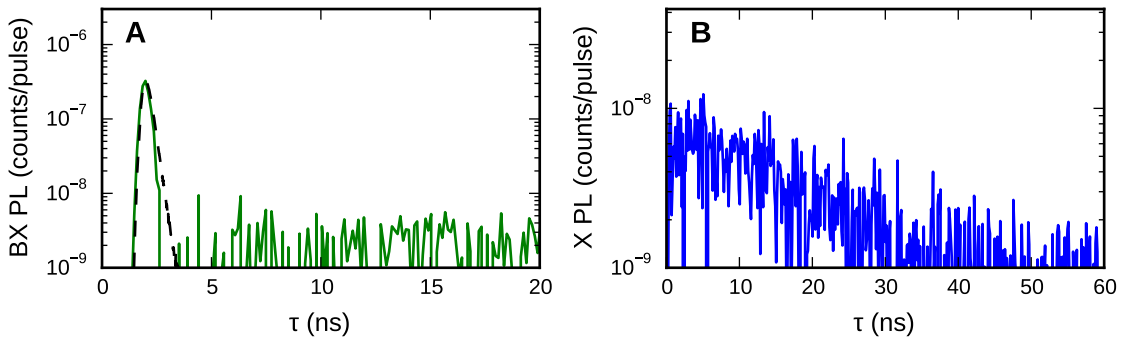


Figure 6-6: **A** Biexciton and **B** monoexciton lifetimes for a CdSe/CdS/ZnS quantum dot, with a biexciton quantum yield of 4.2(1) %. The dashed black curve is the instrument response function of the microscope; the biexciton lifetime is no more than ≈ 300 ps.

1.1 ns lifetime.

### 6.4.1 Exotic Materials

Moving on from our initial sample, we studied a batch of CdSe/CdS/ZnS quantum dots. These nanocyrstals have a biexciton quantum yield on the order of 6 %, and for individual molecules we obtain number-resolved data such as Figure 6-6. For these nanocrystals, the extracted biexciton signal is limited by the instrument response function of our microscope: the Auger rate for these nanocrystals is sufficiently fast that the biexciton lifetime is less than ≈ 300 ps. This is consistent with the measured monoexciton radiative lifetime of 18 ns, which indicates a biexciton lifetime of 180 ps given the measured biexciton quantum yield. For such a sample $g_0^{(2)}$ provides meaningful statistics, but a narrower instrument response function is needed to measure the biexciton lifetime at the single-molecule level.

In more exotic structures, new physics may emerge. For example, in partially-confined systems such as colloidal nanoplatelets,[142,153,154] it is conceivable that multiple excitons may coexist without a strong interaction if they can be created with sufficient spatial separation.[155–158] To test this idea, we studied individual molecules from a sample of core/shell 4CdSe/3CdS nanoplatelets. For one molecule in this sample we find a biexciton quantum yield of 42 %, and an exciton radiative lifetime

of 18 ns. However, examining the biexciton emission we find that it is best fit as a biexponential with time constants of 1 ns and 11 ns. The fast time constant for the biexciton emission suggests a biexciton quantum yield of about 20 %, which underestimates the value measured through $g_0^{(2)}$ by a factor of 2. We find similar values for another nanoplatelet from this sample, and it is conceivable that the excess apparent biexciton signal is the result of emission by an unbound pair of excitons. However, the signal-to-noise of this experiment is relatively low due to the unstable emission of these materials, and given the large amount of background emission it is entirely possible that our approximation of the background containing no nanocrystal emission is invalid. Our background-correction method should properly account for out-of-plane emission, so our results suggest but do not conclusively demonstrate the existence of an unbound biexcitonic state.

Finally, we examined emission from a thick-shelled CdSe/CdS quantum dot. Due to the large shell the absorption cross-section at 414 nm was significantly higher than for normal quantum dots, and such we were able to much more accurately measure the biexciton emission relative to the background, though unfortunately these dynamics were extremely chaotic and the nanocrystals photobleached after a short time (Figure 6-8). For one quantum dot from this batch, we measured an exciton radiative lifetime of 34 ns, $g_0^{(2)} = 0.194(1)$, and $g_0^{(3)} = 0.014(3)$. The $\mathrm{PNRL}^{(2,1)}$ data are fit well as a triexponential with time constants of 750 ps, 4.9 ns and 24 ns. These results are somewhat baffling: if this first-photon emission arises from the biexciton, then none of these time constants are consistent with the measured $g_0^{(2)}$ and exciton radiative rate. But based on $g_0^{(3)}$ this emission is unlikely to arise from the triexciton. It is also conceivable that we are observing some emission from the CdS shell, because we used an 414 nm laser for excitation.[68]

## 6.5 Conclusions

We have demonstrated that the true triexciton, biexciton, and monoexciton emission lifetimes of nanocrystals may be determined through number-resolved emission

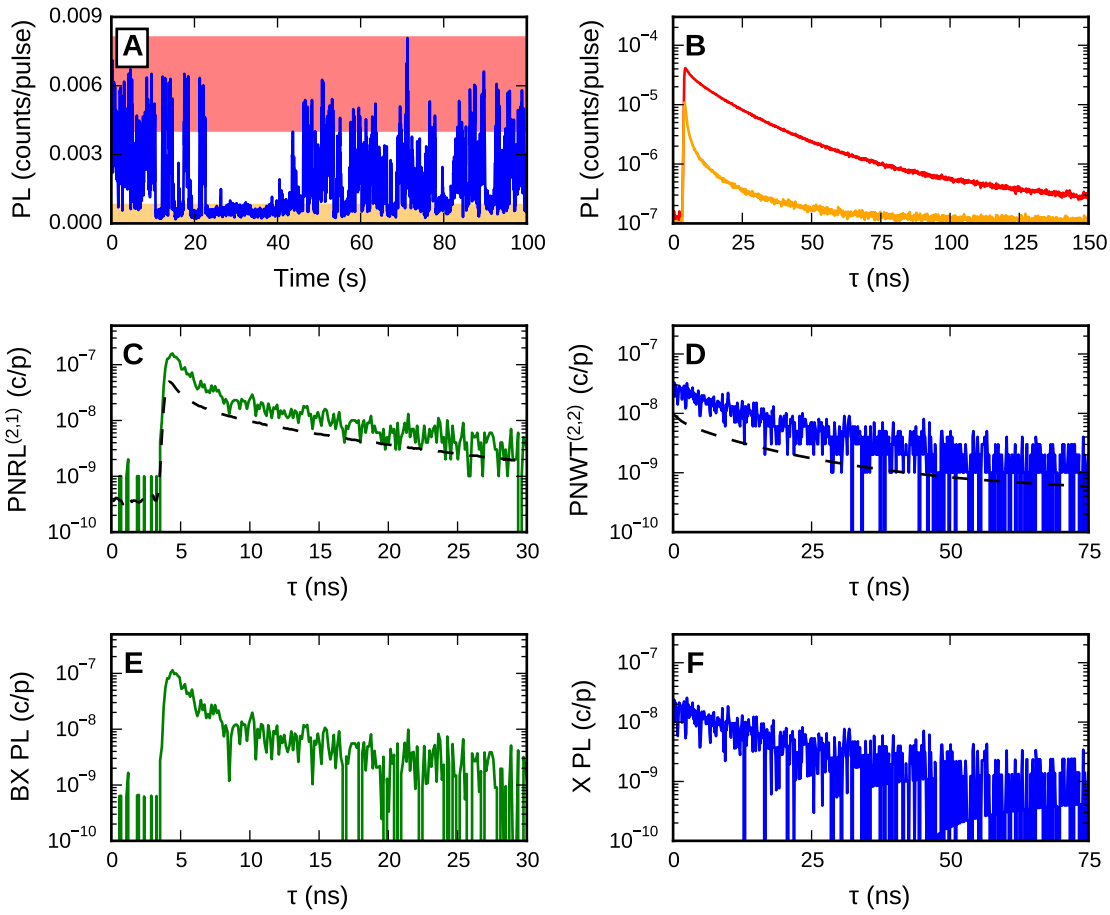


Figure 6-7: Two-photon emission from a 4CdSe/3CdS core/shell colloidal nanoplatet. Subfigure descriptions are the same as those of Figure 6-3.

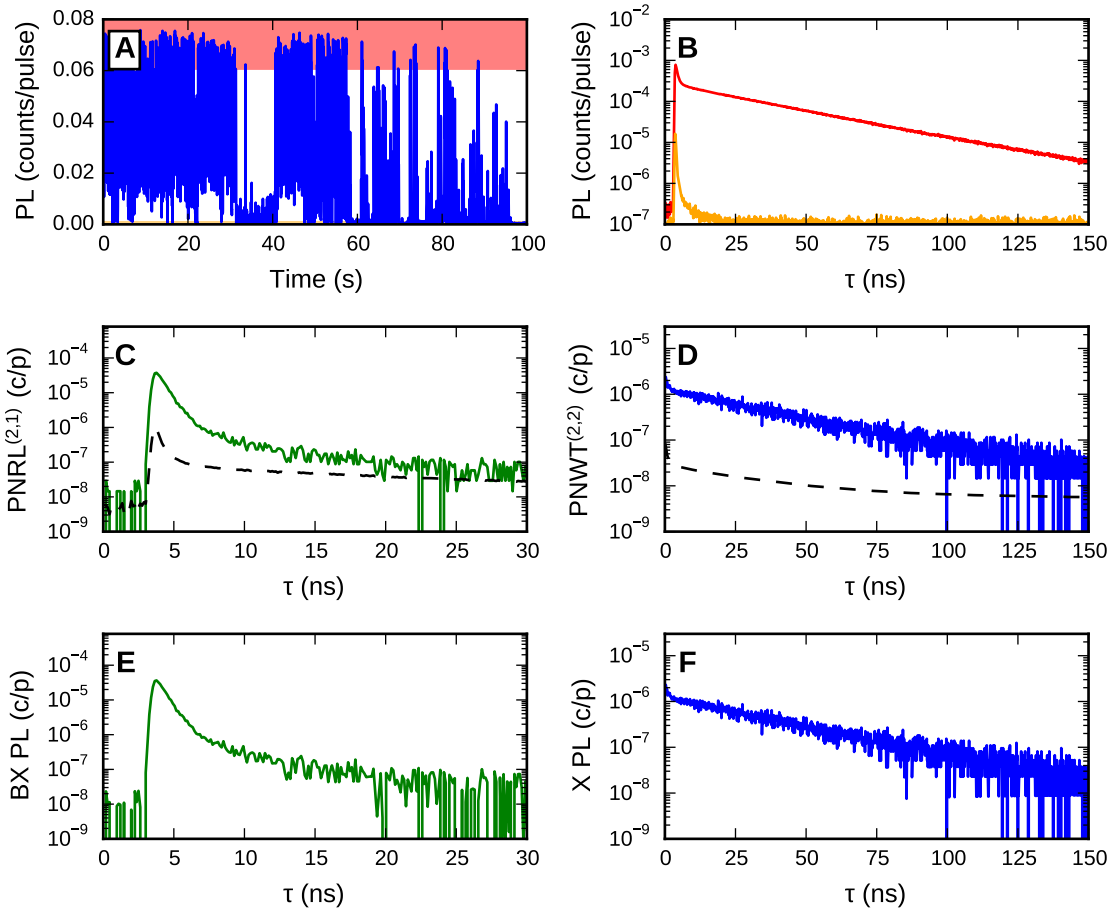


Figure 6-8: Two-photon emission from a thick-shell CdSe/CdS core/shell quantum dot. Subfigure descriptions are the same as those of Figure 6-3.

lifetimes. For quantum dots emitting from the bright state, all states with equal numbers of excitons are equivalent, regardless of the original number of excitons, and relax with monoexponential dynamics. Biexciton emission is completely described as the competition between radiative and Auger relaxation.

For more exotic materials such as nanoplatelets and thick-shell quantum dots, we find preliminary evidence which suggests the existence of a long-lived biexcitonic state. This emission could arise from some spatially-separated charge carriers, but could also arise from various known artifacts of the experiment.

## 6.6 Supporting Information

### 6.6.1 Nanocrystal Samples

#### QD Vision quantum dots

This sample of red-emitting quantum dots was provided by QD Vision, batch identifier grCdSeCS-486.

#### CdSe/CdS core/shell quantum dots

This sample was provided by Ou Chen and Yue Chen (Bawendi group, MIT). It was synthesized according to the methods of Chen et al.[107].

**Synthesis** 1-octadecene (ODE, 90 %), trioctylphosphine oxide (TOPO, 99 %), trioctylphosphine (TOP, 97 %), oleylamine (OAm, 70 %) were obtained from Aldrich. Cadmium oxide (CdO, 99.998 %), selenium powder (99.999 %), stearic acid (98 %), myristic acid (MA, 99 %), oleic acid (OLA, 90 %), octadecylphosphonic acid (ODPA) and hexylphosphonic acid (HPA, 99 %) were purchased from Alfa Aesar.

CdSe/CdS core/shell QDs were synthesized according to our previously-published method.[107] Briefly, a hexane solution containing 300 nmol of CdSe QDs was loaded in a mixture of 1-octadecene (ODE, 5 mL) and oleylamine (OAm, 5 mL). The reaction solution was degassed under vacuum at room temperature for 1 h and 120 °C for 20 min to completely remove the hexane, water and oxygen inside the reaction solution. After that the reaction solution was heated up to the growth temperature under nitrogen flow and magnetic stirring. When the reaction solution had reached 240 °C, a desired amount of cadmium(II) oleate (Cd-oleate, diluted in 6 mL ODE) and 1.2 molar equivalents of octanethiol (diluted in 6 mL ODE) were injected dropwise into the growth solution at a rate of 3 mL/h using a syringe pump. The reaction temperature was further raised to 310 °C and maintained for the rest of the reaction. After finishing precursor infusion, 1 mL oleic acid was quickly injected and the solution was further annealed at 310 °C for 60 min. The resulting CdSe/CdS core/shell QDs were precipitated by adding acetone, and then redispersed in hexane. The particles

were further purified by precipitation-redispersion for two more rounds and finally suspended in $\approx 2\,\mathrm{mL}$ hexane or chloroform.

### CdSe/CdS/ZnS core/shell quantum dots

This sample was provided by Ou Chen and Yue Chen (Bawendi group, MIT).

### CdSe/CdS thick-shell core/shell quantum dots

The sample was provided by Igor Coropceanu (Bawendi group, MIT). It was synthesized according to the methods of Coropceanu and Bawendi [159].

### CdS/CdSe/CdS shell/core/shell nanoplatelets

This sample was provided by Igor Fedin, Chunxing She, and Dmitri Talapin (University of Chicago). The sample studied consisted of a four-monolayer CdSe core, and a three-monolayer CdS shell.

**Synthesis** All sample synthesis and preparation was performed inside an $N_2$-filled glovebox.

CdSe NPLs were synthesized following a previously published procedure [153] with slight modifications. Specifically, in a three-necked flask, 170 mg of cadmium myristate was degassed in 15 mL of 1-octadecene (ODE) at 90 °C for 30 min before adding 12 mg of selenium powder. The resulting mixture (cadmium myristate and Se in ODE) was further degassed at 90 °C for 1 h. We then heated the mixture rapidly and added 40 mg of cadmium acetate dehydrate at 195 °C. After keeping the reaction mixture at 240 °C for 5 min, we rapidly cooled the mixture down to 70 °C and then injected a solution of 2 mL of oleic acid in 10 mL of anhydrous hexane. The mixture was then centrifuged, and the precipitate containing the nanoplatelets was suspended in hexane.

CdS/CdSe/CdS shell/core/shell NPLs were synthesized following one of the variants of the colloidal atomic layer deposition approach [142,154] with some modifications and optimizations. Before shell growth, we precipitated CdSe NPLs, synthesized as

described above, and re-dispersed them in hexane three times to remove free $Cd^{2+}$ in the solution. Then, the first layer of $S^{2-}$ was introduced by phase transferring 4CdSe NPLs from hexane to 5 mL of N-methylformamide (NMF), in which 50 µL of aqueous solution of ammonium sulfide (40 %) was dissolved. After phase separation, we added acetonitrile and toluene to precipitate the NPLs, and dispersed them in 5 mL of NMF. To grow the first layer of Cd, we redispersed the solution in 2 mL of NMF, introduced 2.5 mL of 0.2 M cadmium acetate in NMF, and stirred the solution for 1 min. Then, we precipitated the NPLs with toluene, centrifuged them, and re-dispersed the precipitate in 5 mL of NMF. The first monolayer of CdS shell growth is completed at this stage, with the surfaces terminated by Cd layers. To grow a thickness of $x$ monolayers of CdS, the above steps were repeated $x$ times. The final shell/core/shell NPLs were dispersed in 5 mL of hexane with the addition of 250 µL of dried 70 % technical-grade oleylamine.

### 6.6.2 Instrument response function of the microscope

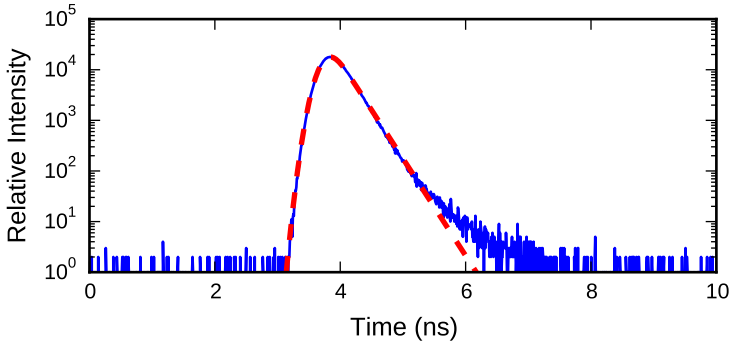


Figure 6-9: Instrument response function of the microscope, measured by detecting the 532 nm laser back-reflected off a silver mirror. The dashed line indicates the fit to a Gaussian function convolved with a single exponential. The optimal fit is: $\sigma = 140$ ps, $\tau = 230$ ps.

# Chapter 7

# Deep-tissue Imaging Using Infrared Emission

## 7.1 Contributions

This work was carried out in collaboration with Oliver Bruns, a post-doctoral biologist in our group with extensive experience handling mice and performing biological imaging, and Daniel Harris, a graduate student materials scientist in our group devoted to the synthesis of infrared-active materials.[26] My contribution to the project was primarily methods development: the design of the imaging apparatus, the development of effective protocols, and methods for optical experiments and data processing.

Some of the results described in this chapter are also reported in Bruns et al.[133] and Harris[26].

## 7.2 Introduction

Tissue is not usually transparent to visible light: if we wish to see what a heart looks like, we generally have to cut open the chest to get a closer view. This is quite invasive, and as a result researchers have developed a host of less invasive methods, such as MRI, X-ray, and PET imaging. Many of these methods have large infrastructural costs, for example the liquid helium required for superconducting magnetics in an

| Material | Emission | Quantum Yield | Emission Lifetime | Diameter† | References |
|---|---|---|---|---|---|
| $Ag_2S$ QD | 800–1200 nm | 2 %* | 50–200 ns | 2–10 nm | [160–162] |
| $Ag_2Se$ QD | 650–1300 nm | 2 %* | 130 ns | 2–40 nm | [163–166] |
| Au QD | 400–1200 nm | | | 1–2 nm | [4–11] |
| Carbon nanotubes (CNT) | 1000–1400 nm | 0.1 %* | | $d$ =3–10 nm, $l \geq$100 nm | [167–173] |
| $Cd_3As_2$ QD | 530–2000 nm | 0.5–60 % | 180 ns‡ | 2–5 nm | [26,174] |
| HgTe QD | 1200–5000 nm | 1–20 % | | 4–10 nm | [175–177] |
| InAs QD | 600–1500 nm | 0.5–30 % | 50–200 ns | 2–5 nm | [26,45] |
| IR-26 | 1100–1300 nm | 0.05 % | 22 ps | | [111,178,179] |
| IR-1061 | 1100–1300 nm | 0.05 %* | | | [180] |
| PbS QD | 800–2000 nm | 0.5–30 % | 0.5–3 µs | 2–16 nm | [113,181,182] |
| PbSe QD | 900–4000 nm | 0.5–30 % | 0.2–3 µs | 7.5–17 nm | [111,130,183] |
| PbTe QD | 1150–2050 nm | 0.5–5 %* | | 2–9 nm | [184] |
| Rare-earth doped NP | 1000–1600 nm | 10–90 % | 10–1000 µs | $>$ 5 nm | [185–189] |
| Singlet Oxygen $\left({}^1O_2\right)$ | 1270 nm | $10^{-6}$ %[190] or 1 %[191] | | | [190–192] |

Table 7.1: A brief summary of some of the known molecular and nanocrystal SWIR emitters. Note that material parameters such as lifetime and quantum yield will vary as a function of size, ligands, etc.; values presented here are meant to reflect typical values for each category, rather than those for a specific sample. Non-emissive materials may also be made with larger dimensions, but these are excluded.

∗: Many quantum yield measurements are performed relative to IR-26 or a related dye. In some cases, these values have overestimated the quantum yield of the sample because of old, overstated reports for the absolute quantum yield of IR-26.[178,193,194] The values indicated here are what we believe to be reasonable possible values, based on the particular measurement performed in a given paper.

†: Inorganic core diameter nanocrystals. Epitaxial shells and ligands will increase the effective diameter.

‡: See Figure B-1.

MRI machine, or have low permissible exposure limits (X-ray), and medical research is constantly moving toward less invasive, less expensive, and less hazardous imaging methods.

One emerging method is SWIR imaging (short-wave infrared, here roughly 1000–2000 nm[1]). Unlike visible light, which generally is completely scattered or absorbed by tissue after a short distance, SWIR light penetrates far deeper through tissues[195] and can be used to examine structures up to millimeters into the body, through skin and skull.[160,170–173] Prior reports have used carbon nanotubes,[168–173,196] silver chalcogenide nanoparticles,[160,161,165,166] lead chalcogenide nanoparticles,[197–199] laser dyes,[180] and rare-earth doped nanoparticles[186] as contrast agents for deep-tissue fluorescence imaging, but in our laboratory we are able to synthesize infrared emitters from materials such as InAs and lead chalcogenides with far superior quantum yield. See Table 7.1 for a summary of SWIR emitters we have worked with or encountered in the literature.

With superior quantum yield comes a relative abundance of signal, which is the primary advantage quantum dots have over other materials. This enables us to measure smaller concentrations of emitters, such that we can use lower doses, or to measure faster dynamics by using shorter integration times. With this in mind, we carried out a number of experiments demonstrating possible applications enabled by sensitivity or high frame rates, including the measurement of: the dynamics of lipoprotein metabolism, vital signs, and blood flow in brain vasculature.[133,200]

In this chapter, we discuss the technical considerations necessary for SWIR imaging. We then discuss three applications which are enabled by the use of our SWIR QD, and finally comment on the future directions of the work.

[1]Practically speaking, we generally refer to SWIR as the region which is accessible to an InGaAs detector but not a silicon detector. Thus our working definition may or may not quite be aligned with others'.

## 7.3 Understanding "Brightness"

For *in vivo* imaging, we can use labels to provide structural or chemical contrast. This requires the introduction of a sufficient number of molecules to provide the correct spatial resolution or sensitivity, with a dosage which does not modify the tissue itself. Thus there are three criteria for evaluating the effectiveness of a particular emitter: absorption cross-section, emission quantum yield, radiative lifetime, and emission density. These criteria are individually more or less important in various circumstances, which we discuss here.

The absorption cross-section of an emitter relates the excitation density with the rate at which fluorophores are excited, typically expressed as an absorptivity per $\mathrm{cm}^2$. For example, a single quantum dot might have a cross-section on the order of $10^{-15}\,\mathrm{cm}^{-2}$,[201,202] and for excitation into the continuum of states with a diffraction limited beam this yields about 10 excitons per $10^6$ excitation photons. Thus for every million photons input, we can expect at most 10 photons output, in the best possible case. This means an experiment must carefully balance the signal needed with the excitation required to prevent tissue damage, which is particularly evident in two-photon microscopy.[203–205] Standards exist for safe exposure limits,[206] and experiments are typically designed not to exceed these limits.

The emission quantum yield is the probability that an excited emitter will emit a photon. This most relevant in wide-field imaging and other low-flux methods, where the excitation of an individual fluorophore is relatively rare and thus the efficiency of photon production is critical.

The radiative lifetime is the average amount of time required for an excited emitter to radiatively relax to the ground state, and is often the product of the emission lifetime and emission quantum yield. For many organic fluorophores this is on the order of a few ns, for quantum dots 10–1000 ns, and for rare-earth doped nanoparticles µs to ms. The radiative lifetime ultimately limits the rate at which photons can be produced by an emitter and is most relevant in microscopy, where the excitation flux can be quite large. For example, in scanning confocal imaging a typical dwell time at

a pixel may be on the order of 100 ns, and fluorophores are often excited to saturation to provide sufficient signal. Under such conditions, it is optimal to have the shortest radiative lifetime.

Finally, the emission density is the number of emitters present per unit volume. The larger a particular emitter is, the fewer of them we can fit into a cell, blood vessel, or other feature of predetermined size. As a result, even an emitter with unity quantum yield and short lifetime is useless if it cannot be delivered to a location. In its place, the use of a number of small but weak emitters is actually a viable option, and so the design criteria for a probe must include its size.

Based on these considerations, we can quantify brightness as follows:

$$\text{Low flux: } B \approx \frac{\text{QY}}{V} \tag{7.1}$$

$$\text{High flux: } B \approx \frac{k_r}{V} \tag{7.2}$$

for emission quantum yield QY, emitter volume $V$, and radiative rate $k_r$ (inverse of radiative lifetime).

## 7.4 Designing SWIR Imaging Apparatus for Biology

SWIR imaging is not sufficiently common in the public sector for there to be standard commercial suppliers of imaging apparatus, and therefore we decided to construct our own. After several attempts, we developed the following design criteria for a wide-field imaging setup:

1. Simplicity. The setup must have the fewest moving parts necessary to achieve maximum stability and ease of alignment.

2. Openness. When working with animals, we need to have the largest possible experimental area to leave room for the mouse, the operator's hands, any cages or tubes, and other pieces of an experiment.

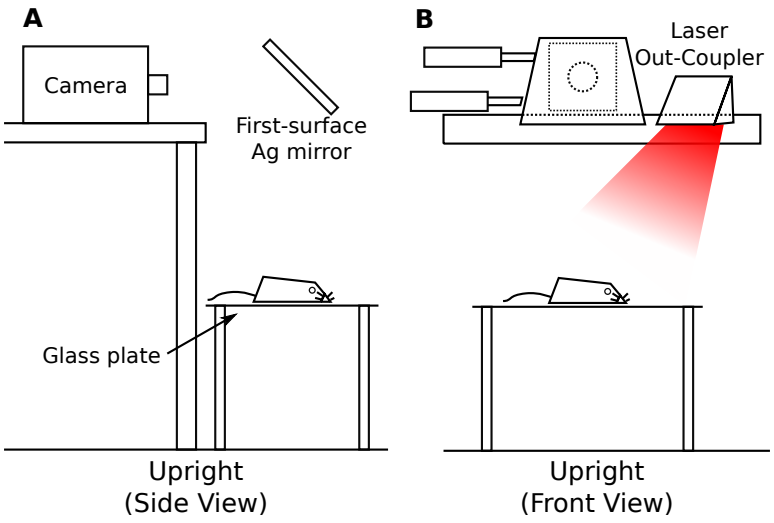


Figure 7-1: **A** The SWIR imaging apparatus used for wide-field experiments (not to scale, particularly the mouse), in the upright configuration. **B** A face-on view in the upright configuration from the perspective of the experimenter, with a fiber-coupled excitation source. The mirror is mounted to an XT95 optical rail using $\varnothing\frac{1}{2}$in posts and post holders. The glass plate is 12 in x 12 in, and is mounted to $\varnothing$1 in posts (6 in or 12 in long) using putty.

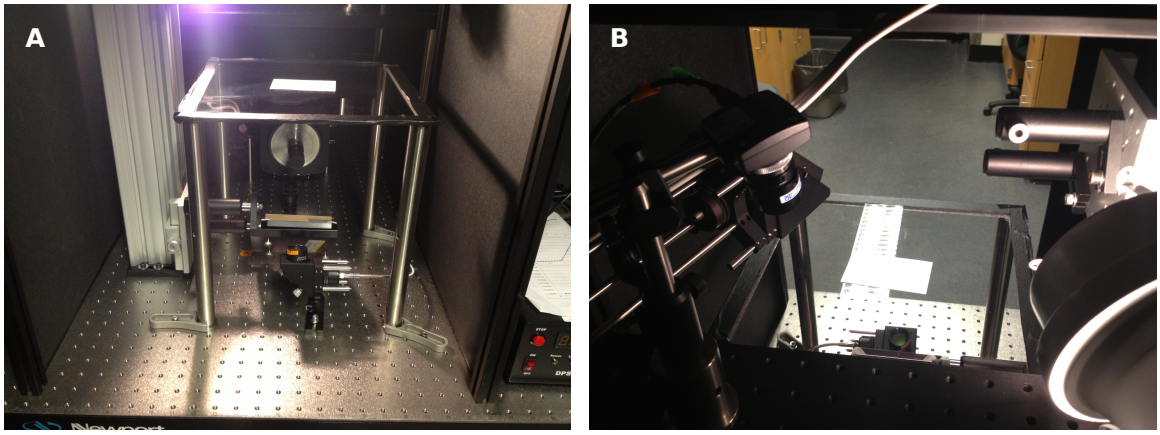


Figure 7-2: **A** The SWIR imaging apparatus used for wide-field experiments, in the inverted configuration from the perspective of the experimenter. The fiber out-coupler (bottom middle) contains a plano-concave lens, SP1000 nm excitation filter, and a ground-glass plate, designed to illuminate the center of the imaging stage. The imaging mirror is mounted directly below the imaging stage, and the business card indicates the typical placement of the mouse. A box is used to block stray light, and to protect the researcher from stray exposure. Controls for the laser are nearby for safety and convenience (right). **B** The view from behind the setup, showing the fiber out-coupler (left), a Si-CMOS monitoring camera (left), the imaging stage (center), an incandescent scene light (lower right), and the XT95 tower used to mount the imaging mirror (upper right).

3. Ease of configuration. In some experiments we wish to image from below the mouse, and for some we image from above. Switching between these two configuration should take minutes at most, and should require minimal or no realignment.

4. Automation. All shutters, power controls, and acquisition must be able to be driven from a single point, with secondary controls for the excitation source and shutter as close to the experiment as possible.

5. Reliability. Anything can go unexpectedly in an animal experiment, and so we must engineer all other aspects of the setup to the point that they will not fail.

With these criteria in mind, we arrived at the apparatus presented in Figure 7-1. In this setup, we use a pane of glass (McMaster-Carr) mounted with putty onto four $\varnothing 1$ in posts (Thor Labs), 6 in long for imaging from above or 12 in for imaging from below. The tower to the left has rail carriages (Newport) aligned to place a 4 in square first-surface silver mirror (Edmund Optics[2]) in the correct position to see the center of the pane of glass, and to provide the correct working distance for our optics. This allows the camera to be mounted horizontally on the table or a raised platform, with sufficient room to install various filters. As such, there is plenty of open access to the working area and sufficient distance between the mouse and the camera to prevent unwanted contamination of the optics. The components used for the working area are generally commodity items, and can be cleaned or replaced as needed.

For the excitation optics, we outcouple light from our laser fiber using a $f = 25$ mm concave-planar lens (Thor Labs) with a wavelength-appropriate anti-reflective coating, and send the defocused light through a ground-glass plate (Thor Labs). There are two out-couplers set up and aligned such that the only modification needed to switch is to move the fiber (large-core multi-mode high-power metal-cladded fiber). We use a

[2]In some of our earlier experiments, we used inexpensive rear-coated mirrors (e.g. "truck" mirrors). These are more readily available in a variety of form factors, but due to the front-surface reflection our data was plagued by ghost images. This limits sensitivity, since bright regions can easily overwhelm neighboring dimmer regions, and so we changed the apparatus to include only first-surface mirrors.

motorized shutter in the free-space component of the laser, which is controlled either using the panel of the driver or in software at the acquisition computer.

This is by no means the only configuration for all experiments. If you find yourself in the position to build a custom setup for your experiments, here are some technical points to consider:

### 7.4.1 Excitation Sources

For broadband excitation we use an incandescent light bulb, which emits plenty of SWIR light and is useful for overall illumination of a scene[3].

For narrow-band excitation, we use lasers and LEDs. There are some LEDs operating at infrared wavelengths, available from sources such as ThorLabs. These can achieve milliwatt to watt of illumination, which is generally sufficient for a small scene (a few $cm^2$), but for larger scenes (e.g. a mouse) we need a few watts. For this purpose we use diode lasers (Opto Engine), which can easily achieve 10 W or more of emission power. We couple this light into high-power metal-shielded multimode fiber optic cables for safety and simplicity, and use out-coupling optics to spread the light uniformly over the scene, typically a short-focus concave lens and ground glass plate.

### 7.4.2 SWIR Imaging Optics

Imaging optics are generally not fully SWIR-compatible. For example, many microscope objectives, microscope tube lenses, camera lenses, and other optics are designed for visible applications and carry coatings and chromatic corrections suitable for those wavelengths. Anti-reflective coatings can drastically reduce the throughput of light outside the design spectrum, and so it is necessary to seek out specialized SWIR equipment.

For microscopy, optics designed for two-photon microscopy tend to have reasonable SWIR throughput, though many of these corrections often cut off around 1100 nm. Many objectives designed for biological microscopy are water-immersion, which can

[3]SWIR emission from incandescent bulbs is actually the reason they are so wasteful for visible illumination. See blackbody radiation and the solar spectrum.

negatively affect the throughput of infrared light at some wavelengths, due to the strong vibrational absorption bands of water.[195]

In addition to throughput, it is necessary to consider the chromatic aberration of imaging optics. Essentially, for any refractive system there will be some variability in the index of refraction as a function of wavelength, leading to different effective focal distances for different wavelengths (see Appendix A.1.2). For detected light over of a range of wavelengths this leads to a blurred image,[172] though for a narrow-band emitter this is less relevant.[133]

For filters, we typically use either colored-glass or dielectric filters. Colored-glass filters at infrared wavelengths are typically composed of PbS or PbSe nanocrystal glasses, and as such exhibit some fluorescence. Dielectric filters eliminate fluorescence but exhibit angle-dependent transmission properties. Typically, we simply use two LP1000 nm colored-glass filters (Thor Labs, FGL1000S), unless it is necessary to detect a specific wavelength band.

### 7.4.3 SWIR Detection

SWIR detection is the most expensive component of the imaging apparatus[4]. For direct detection the only real option is an InGaAs-based imaging plane system, which is expensive for three primary reasons: growing InGaAs of sufficient quality is difficult, there is not a high demand outside of defense applications, and the sale of imagers is regulated by ITAR.

The issue of crystal growth is being addressed, and there are now a few factories in the world which can provide chips of suitable quality for imaging. Vendors selling cameras include Princeton Instruments, New Imaging Technologies, Sensors Unlimited, and Raptor Photonics, though most of these vendors get their chips from the same source.

The lack of demand is closely linked to the ITAR regulations. In short, ITAR

[4]This is becoming less true with each passing day. When we began this work, ITAR-free cameras with good specifications cost on the order of $100k. Now, smaller and less-cooled systems cost less than $20k. Depending on your sensitivity and spatiotemporal needs, SWIR imaging may very well be afordable.

regulations apply to potentially defense-sensitive items and require that no foreign national have access to the restricted item[5], typically by restricting access to the room in which it is stored. Furthermore, an item produced internationally but imported into the United States *becomes* ITAR-regulated if it is sufficiently equivalent to another regulated device. Lastly, the onus is on the customer, not the vendor, to verify the status of an item and to ensure that proper steps are taken. As a general rule, all existing InGaAs imaging planes are regulated unless explicitly verified otherwise.

That being said, vendors are gradually successfully petitioning to have their products deregulated, and most now offer ITAR-free products. We generally avoid purchasing any item with ITAR restrictions, to prevent the highly likely case that a foreign national comes in contact with it (see Oliver the German, a.k.a. the resident mouse biologist for the project).

Other than these legal issues, an InGaAs imaging plane is functionally identical to any other monochrome plane detector.

One final consideration for any imaging plane is the readout method. There are two basic schemes: integrate then read, or read while integrating. In the integrate-then-read scheme, all pixels are set for detection for some amount of time, after which the pixels are deactivated and their stored charge measured. This ensures that all pixels in a given frame represent the same time point, and is standard for most scientific cameras. In the read-while-integrating scheme, all pixels are kept on at all times, and each row is successively deactivated, read out, then reactivated. This is common in CMOS cameras and has the advantage of maximizing the exposure time for any given pixel, but can lead to artifacts if the dynamics are faster than the frame rate, for example in images of plane rotors as taken with iPhones or similar cameras.[207] The integrate-then-read scheme does not suffer from this artifact, but suffers from a reduced exposure time since the duration of a frame can be no less than the time required to read out all pixels (e.g. $\approx 9\,\text{ms}$ for the NIRvana). Make sure you know your requirements before investing in either solution.

[5]This includes lenses, screws, and other military-specification items!

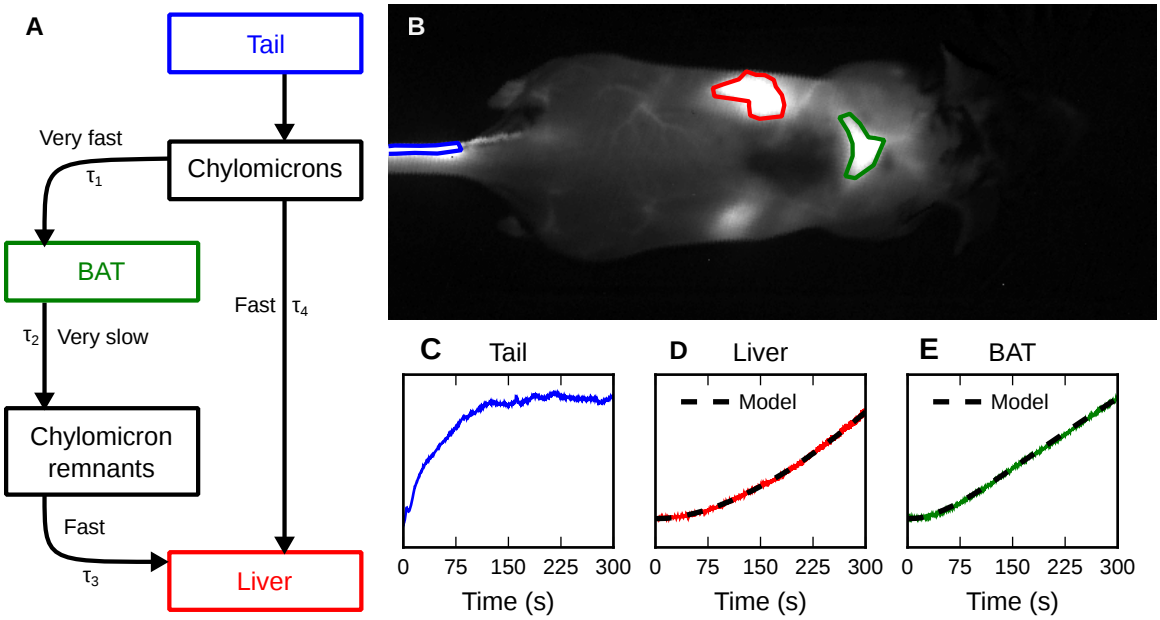


Figure 7-3: Metabolic imaging in a mouse. **A** A conventional model for the processing of injected chylomicrons, where each transfer process is approximated as first order. **B** The final state of the mouse, with the tail injection size (blue; left), liver (red; middle), and brown adipose tissue (BAT; green; right) indicated. The bright region below the liver is the spleen, and is not accounted for in our model. **C**–**E** The measured dynamics for the tail, liver, and BAT, respectively. The signal from the tail is set as a fixed parameter, and the dashed black lines indicate the predictions of the optimized model. We obtain $\tau_1 = 4\,\text{s}$, $\tau_2 = 14\,\text{min}$, $\tau_3 = 19\,\text{s}$, and $\tau_4 = 18\,\text{s}$ by fitting against the square error magnitude with a downhill algorithm. These parameters largely provide an order-of-magnitude estimate, since there are many similarly-well-fitting values nearby in phase space.

## 7.5 Applications of SWIR Imaging

### 7.5.1 Metabolic Imaging

There is considerable interest in understanding the activity and dynamics of the organs associated with digestion,[208–212] as a means for understanding the effects of various interventions on the process. For example, it would be useful to study the effects of a drug treatment regime in real time, but the measurement of these dynamics is complicated by the dearth of analytical methods for assessing nutrient concentrations which are non-invasive and have reasonable time resolution.

To measure the kinetics of lipid digestion, we synthesized lipoproteins labeled

with InAs QDs, which are micron-scale water-soluble micelles. We introduced these into a sedated mouse through the tail vein at a low rate (13.3 µL/min, 10 mg/mL triglycerides), and measured the emission from the mouse over time. We found that most emission comes from the brown adipose tissue (BAT), the liver, and the spleen.

Prior experiments have suggested that the process of lipoprotein digestion occurs through a few pathways.[213–217] One pathway is that the chylomicrons reach the BAT, where they reside for some time while being broken up into smaller micelles, which are then cleared from the bloodstream by the liver and spleen. Another pathway is that the chylomicrons are cleared directly by the liver. This leads to the kinetic model presented in Figure 7-3A, where we approximate each process as first-order.

To validate the model, we identify the tail, BAT, and liver in the imaging data (Figure 7-3B) to obtain kinetics data. We use the experimentally-measured tail signal as the population driving the first-order model, and treat as free parameters the transfer rates and the proportionality between the measured BAT and liver signals and the QD concentration[6]. Optimizing to the square error between the model and the experimental BAT and liver signals, we achieve the fit presented in Figure 7-3C–E.

The advantage of this method is the immediacy of the measurement, which allows us to collect time points with effectively arbitrary resolution. This is a stark contrast to earlier work using radio-labeled nutrients,[217] in which each time point yields a precise measurement of concentration but requires the sacrifice of the mouse. Other MRI-based methods are able to yield reasonable time resolution within a single mouse,[208] but suffer from a non-linear signal with low sensitivity and dynamic range.

Note that, while we can obtain a good qualitative fit to the kinetic model, this only confirms that the model is not inconsistent with the data. To properly test any metabolic model, we must design experiments in which the injection profile is varied in some way or some medicinal intervention is applied, to provoke a testable response. For example, our model treats each organ as containing a single type of nanocrystal-containing population, but what if some chylomicrons are taken semi-

[6] We cannot measure absolute concentrations in this method, so we assume the measured intensity is proportional to the true concentration.

permanently up into the BAT instead of being cleared immediately? To test this mechanism, we have performed preliminary experiments in which the injection is halted, and indeed we observe two distinct timescales for clearance from the BAT, one on the order seen in Figure 7-3, and another longer-lived population consistent with uptake. This is consistent with other reports in the literature,[209] and in future experiments we anticipate the design of injection profiles and other interventions as tools for accounting for all possible metabolic pathways.

### 7.5.2 Vital Signs of Awake and Unrestrained Mice

Measuring the vital signs of a human can be performed in various ways, for example by using a stethoscope, by attaching electrodes, by using infrared transmittance to measure fluctuations in blood volume, or perhaps by measuring fluctuations in skin height near exposed blood vessels. Most of these methods function best for a cooperative patient, particularly those requiring direct contact, but what if a patient will not cooperate? This is a conundrum faced in animal research, where researchers are interested in studying the activities of animals under normal physiological conditions but often must use invasive methods to obtain results.

For example, to measure the heart rate of a mouse, researchers may implant electrodes into the nervous system of a mouse,[218] and before study the animal must be allowed to recover for a significant amount of time. An alternative option is to use conducting gel pads as electrodes, but these tend to be unreliable.[219] Each of these methods are viable but have significant drawbacks, and so we explored fluorescence imaging as an alternate solution.

To measure the heart rate of a mouse, we studied the dynamics of emission from the blood contained in the heart, using the intensity of emission as a measure of the relative volume of blood over time. During a heartbeat the various chambers will empty and fill, giving rise to $\approx 30\%$ variations in total contained blood volume. This occurs for up to 800 bpm, or $\approx 13$ Hz. To measure this process we acquired intensity data on the order of 60 Hz.

In our experiment, we prepared PEGylated InAs QDs and injected them into the

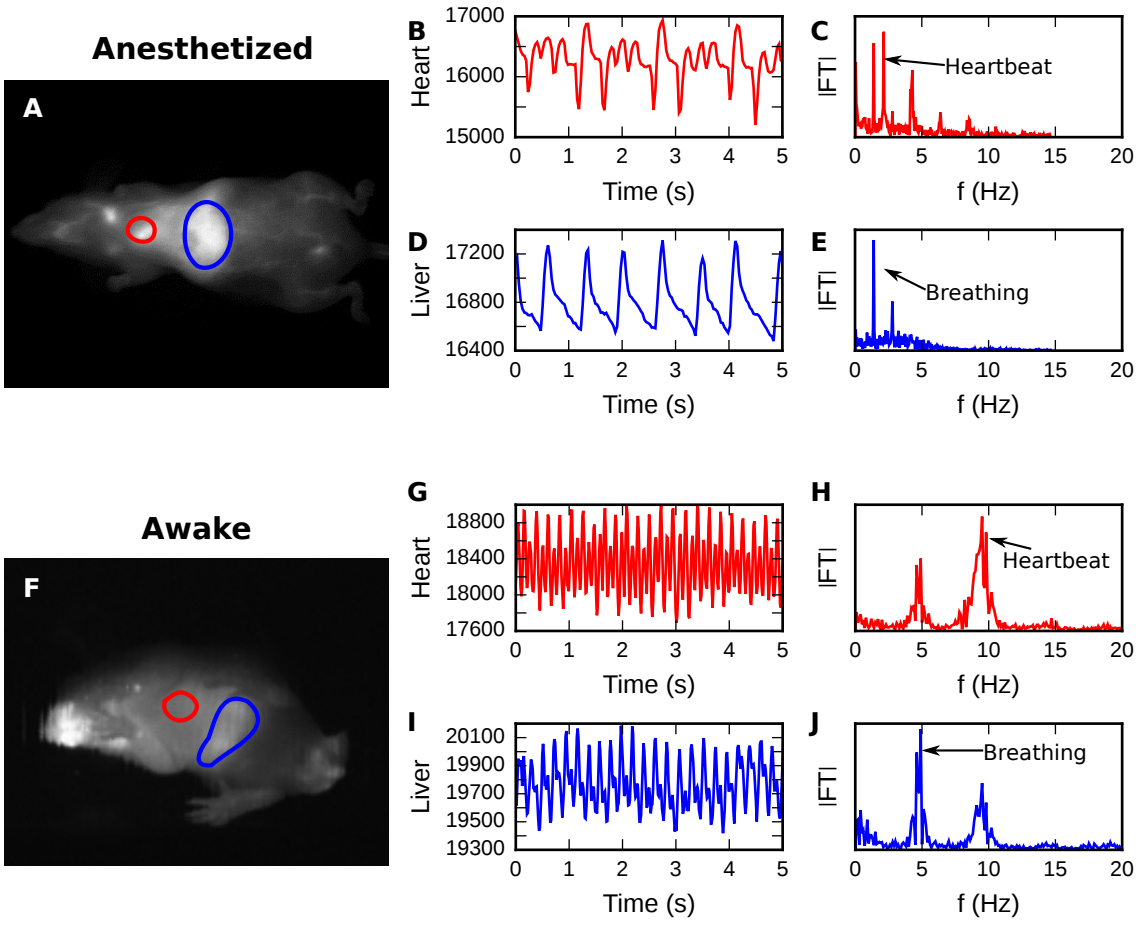


Figure 7-4: SWIR imaging for the monitoring of mouse vital signs. **A**–**E** Vital signs of an anesthetized mouse, measured at 30 fps. The red region of interest (**A**, left) is the heart, with the measured **B** intensity and **C** Fourier transform magnitude plotted. The mean was subtracted from the intensity data before the FT was performed, to suppress the 0 Hz component. The heartbeat of this mouse is 130 bpm. The blue region of interest (**A**, right) is the liver, whose **D** intensity and **E** FT magnitude are shown. The movement of the liver into and out of the region of interest shows the breathing rate of 84 Hz, which is also evident in **C**. Note that the higher harmonics present in **C** and **E** arise from the fundamentals indicated. **F**–**J** The equivalent analysis of an awake mouse resting in the field of view, measured at 66.5 fps. This mouse has a heartbeat of 550 bpm, and a breathing rate of 300 bpm. Higher harmonics are also apparent, though less evident than in **C** and **E**.

tail vein of a mouse. Once the particles had distributed systemically, we excited the mouse with an 808 nm source (60 mW/cm$^2$) and imaged the emission using an LP1000 nm filter. We performed this experiment for a sedated mouse and for a mouse which was awake, and were able to detect the fluctuations in heart emission intensity (Figure 7-4); the sedated mouse had a heartbeat of 130 bpm, and the awake mouse had a heartbeat of 550 bpm.

In addition to measuring the heartbeat rate of the sedated and awake mice, we can measure their breathing rates by observing the motion of the livers as the lungs compress and expand. The sedated mouse breathes at 84 bpm, while the awake mouse breathes at 300 bpm (Figure 7-4).

These experiments highlight the profound differences between awake and sedated animals, which is an obvious result: nobody expects that an animal will behave under anesthesia as it would when awake. But many mouse-based experiments rely on data acquired through means which are sufficiently invasive as to require sedation, and part of the goal of new measurement methods is to remove these perturbations. Ideally we would not even need a fluorescent, but at the moment SWIR imaging requires the external introduction of emitters (see Section 7.6.2 for our work to this end).

### 7.5.3 Intravital Microscopy

Cancerous cells exhibit an abnormal ability to survive in hypoxic and otherwise harsh conditions, which makes them resilient under conditions that kill normal cells.[220,221] Not coincidentally, tumors tend to exist in regions where blood vessels are contorted into abnormal configurations, such that the normal flow of nutrients and waste is disrupted. Understanding how and why this behavior occurs is of considerable interest for researcher looking to understand how various interventions affect the regrowth or replacement of damaged blood vessels, which requires tools to measure the flow of blood throughout the brain.

There are several existing methods for measuring flow or structure in vasculature. Two-photon microscopy (2PM) is the standard for measuring structure at depth but suffers from low signal throughput and photodamage. When implemented as a scan-

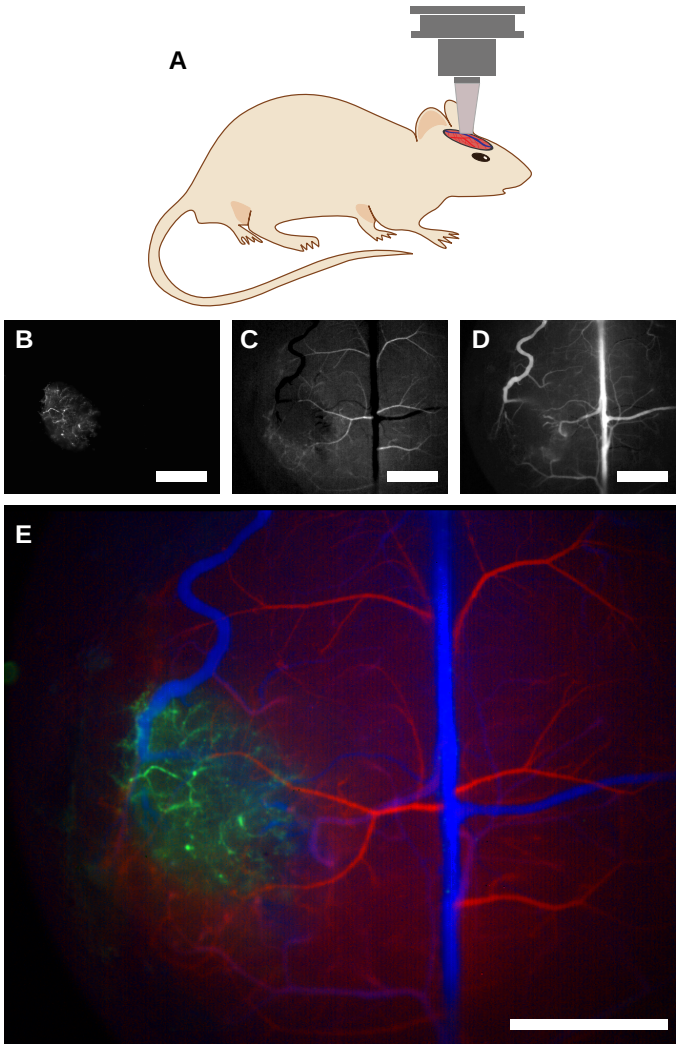


Figure 7-5: **A** A schematic of a mouse with a cranial window, akin to what is used in our brain-imaging experiments. **B** Three days after injection of composite QD particles, a glioblastoma multiforme (GBM) has accumulated the particles. **C** Immediately after injection of a second dose of QDs the arteries are illuminated, and **D** afterward the veins are illuminated. **E** Coloring the tumor green, the arteries red, and the veins blue, we obtain an angiograph. Scale bars are 1500 µm.

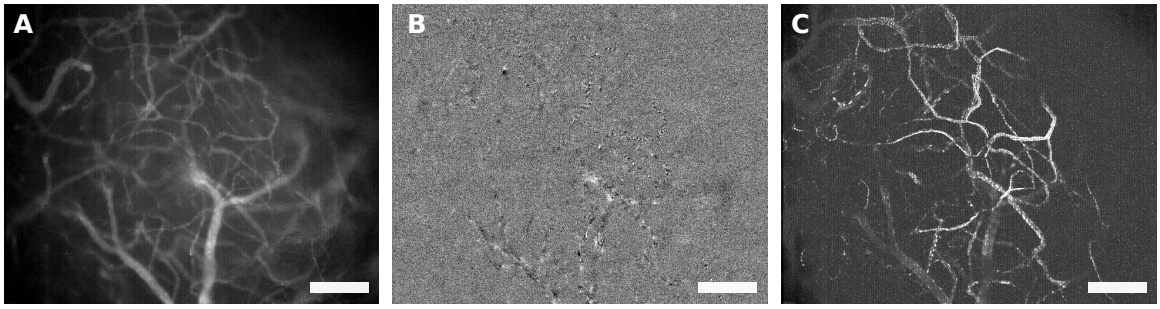


Figure 7-6: Forming z-sections through single-particle imaging. **A** A sample image of the brain, with individual QD composite particles visible. **B** The difference between two successive frames. **C** The projection of the maximum intensity of the diffed frames for this field of view. Scale bars are 200 µm.

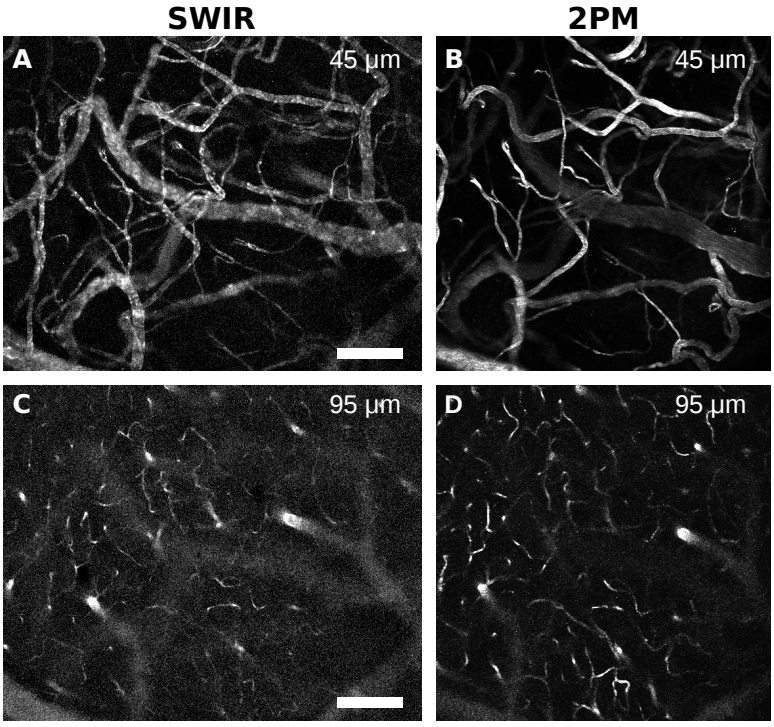


Figure 7-7: A comparison of structural images of a mouse brain at various depths, as obtained using **A, C, E** SWIR one-photon microscopy or **B, D, F** visible two-photon microscopy. Scale bars are 200 µm.

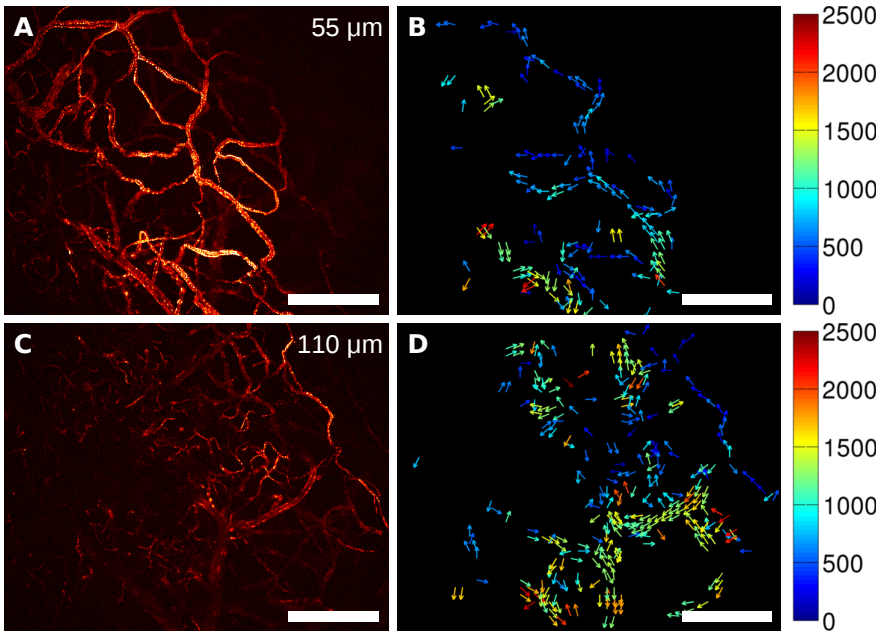


Figure 7-8: **A,C** Structural images at various depths of a mouse brain. **B, D** Velocimetry maps for the same fields of view. Scale bars are 300 µm, and the units of velocity are µm/s.

ning method, 2PM necessarily trades spatial and temporal resolution, since it can only measure signal for one voxel at a time, and kinetic studies are limited to measurements along very specific dimensions.[222] Optical coherence tomography (OCT) methods exist to measure flow by detecting the associated Doppler shift,[223,224] but the analysis is complicated by the limited resolution of the Doppler angle. Finally, optical frequency-domain imaging (OFDI) can achieve spatial resolution comparable to 2PM without a label but is limited in spatiotemporal resolution for similar reasons.[225]

The strong signal afforded by SWIR QD enables direct wide-field microscopy, such that we are able to acquire a full-frame image at rapid rates at 2PM-like depths. To visualize the flow of blood in a mouse brain, we obtained mice with glioblastoma multiforme (GBM), a form of brain cancer, which had been equipped with a cranial window. We formed PEGylated QD composites, such that individual particles yielded sufficient signal to be imaged in our microscope. After injecting these particles into the mouse, we waited three days to allow them to either accumulate in the tumor or clear from the bloodstream. Examining the brain under the microscope, we obtain Figure 7-5B. After the injection of a second dose of QDs, we can identify the arteries

and veins by their temporal profiles, since arteries will exhibit QD emission before veins, and obtain Figure 7-5C and 7-5D, respectively. Combining these images yields the angiograph shown in Figure 7-5E.

Beyond the identification of arteries and veins, we may use our ability to visualize the transit of individual particles through the field of view to isolate a single z-section, and repeat the measurement for several depths to reconstruct the three-dimensional vascular structure. To do this, we acquire a sequence of images for a given field of view at 60 fps, each of which may look like Figure 7-6A. In these images, the particles are visible at the focal plane, but become blurry or otherwise indistinguishable outside this z-section. By calculating the difference of intensity between successive frames (Figure 7-6B), we isolate the contribution of the particle motion, since the background and out-of-plane motion do not give rise to a dynamic signal at this timescale. This yields a positive signature for the new location of each particle, and a corresponding negative signature for its original location.

We can calculate the maximum intensity projection for the diffed frames to reconstruct the vascular structure in the focal plane (Figure 7-6C). Our structural resolution is directly related to the ability to observe the transit of at least one particle through each vessel, as with other stochastic methods such as STORM,[226] but within 10 s (600 frames) we are able to obtain images such as Figure 7-6C. By adjusting the relative height of the mouse and the objective, we can obtain data to reconstruct the vasculature in three dimensions, with results comparable to two-photon microscopy images of the same field of view (Figure 7-7). Both images require seconds of integration time, but the SWIR images can be collected under relatively lower excitation flux, eliminating the photodamage typically associated with two-photon microscopy.

The striping of the nanocrystal emission evident in Figure 7-7A is a consequence of the integrate-then-read electronics in our camera: the bright spot occurs during integration, while the dark gap occurs during readout. In this method, our ability to resolve motion is limited by our integration time, since a fast-moving particle will lead to a longer streak with less intensity per pixel. Thus our integration time and spatial resolution set an upper bound on our ability to resolve in-plane motion.

To quantify flow, we use particle image velocimetry (PIV[227–230]) to measure the relative displacements of particles and thus the velocity in time and space. Particle image velocimetry is a correlation method which determines the relative probability of signal having shifted between neighboring pixels between frames, such that the minimum velocity we can measure is set by the spatial resolution and the acquisition rate. The maximum velocity we can measure is set by the frame width and acquisition rate; if a particle leaves the field of view, we cannot determine its displacement between frames. For our experiments, this yields a range of velocities of 0–2400 mm/s.

Performing PIV for our mouse brain data, we obtain velocity maps such as the one shown in Figure 7-8B, with corresponding structural image Figure 7-8A. In the structural image, bright regions are regions of low velocity since the intensity is concentrated in a small number of pixels, while dimmer regions represent faster flow. PIV enables us to capture both regimes effectively, providing a three-dimensional spatially-resolved measure of average blood velocity.

With these microscopy tools, we can perform measurements equivalent to two-photon microscopy, but with far lower excitation flux and minimal experimental complexity. As a plane-imaging method our spatial resolution is set by the pixel pitch of the camera, and our acquisition rate is set by its readout time. At present, our emitters are not the limiting factor for velocity resolution, and as the camera technology advances the benefits translate directly onto our imaging methods.

## 7.6 Future Directions

### 7.6.1 FDA-Approvable Emitters

Simply put, it is extremely unlikely that the FDA will ever approve quantum dots for labeling in humans. They tend to be composed of highly toxic materials (e.g. Cd, In, Pb, Se, Te, As), coated with reasonably caustic ligands (amines, thiols, etc.), and have surfaces which can be highly reactive (Ag nanoparticles are used as antimicrobial agents). Some of these issues can be addressed, but ultimately even a sound scientific

argument is unlikely to quell public discomfort over the perceived hazards. The one exception is if an application emerges which is sufficiently important to override toxicity concerns, as has been the case with Gd-containing MRI contrast agents,[231] but modern medicine is constantly moving towards less-invasive procedures and generally will not tolerate regression.

As such, the path forward is to identify and develop potential fluorophores which are non-toxic, bright, and biologically compatible. This is complicated by the fact that, fundamentally, infrared emission is not generally found in organic molecules due to the competition with vibrational relaxation. This is the reason why inorganic nanocrystals are uniquely qualified for SWIR imaging, and a starting point for future work.

One potential candidate is Au semiconductor clusters. Such clusters are quantum dots for small numbers of gold atoms, and have been shown to be emitters of visible[6–9] or infrared light.[4,5,10,11] However, the literature is full of conflicting reports as to the exact relationship between cluster size and emission character. This is most likely evidence that the excited state is likely delocalized over the gold and the ligands, and thus its dynamics are exquisitely sensitive to the balance of core oxidation state and surface passivation.[232–234] That being said, if these clusters can be induced to have even a moderate quantum yield of 1 %, they would be of great interest due to their small size and potential non-toxicity. One potential concern is that slightly larger clusters are plasmonic in character and extremely effective catalysts,[235] but this is a problem which may be solved by sufficient stabilization and purification.

It is conceivable that other metals can act as quantum dots. For example, silver oxide clusters are known to emit visible light,[236] and generally visible-emitting materials are far more well-known due to the simplicity of serendipitous discovery: we can see visible emission, and therefore do not need to invest time with specialized instruments to search for it. It could potentially be quite rewarding to screen a variety of materials to determine whether SWIR emission exists at all, with the goal of determining which elements can be used to form emissive clusters and which cannot. Armed with such knowledge, we can identify the emissive species and optimize around

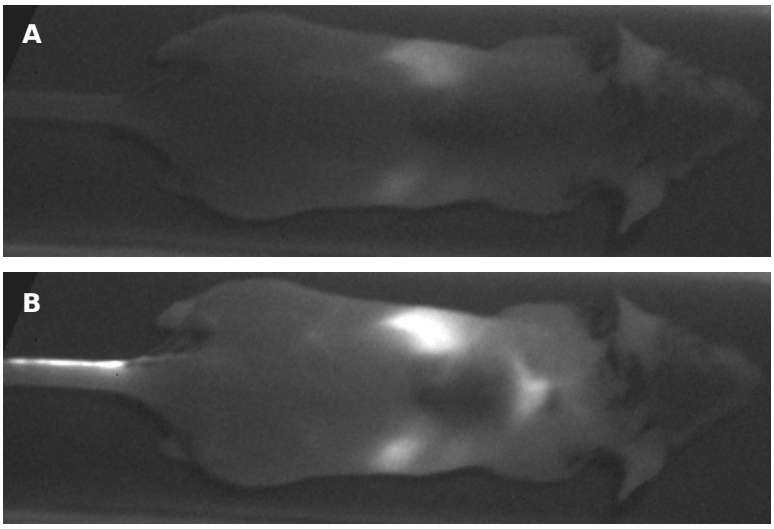


Figure 7-9: **A** An image of emission from a mouse under excitation by 808 nm light with a pair of LP1000 nm emission filters. The liver and spleen exhibit some autofluorescence (see Section 7.5.1). **B** The same mouse, during injection of QD-labeled lipoproteins.

its structure.

One metal of interest is lead. While this cannot be used for medical research, if lead clusters are found to be emissive it could prove to be useful in water monitoring and other processes. In Hwang[21], emission around 1600 nm from PbS-based optoelectronic devices is attributed to reduced lead clusters on the surface of the particles, and if we can independently synthesize lead clusters we can more clearly determine the source of this emission.

### 7.6.2 Endogenous Infrared Autofluorescence

When processing experimental images of mice, we typically present images with brightness adjusted to prevent saturation of detected emission. But this suppresses a key signal present in all mice, which is the autofluorescence of various tissues.

For example, in Figure 7-9A, on the top we see a mouse illuminated by an 808 nm source, before injection of labeled lipoproteins. In Figure 7-9B we see the same mouse, with the lipoproteins injected. The liver and spleen are clearly visible before the injection; some autofluorescence occurs naturally in these organs. Understanding

the molecular and biological origin of this autofluorescence may lead to non-invasive screening methods for a variety of diseases.

To characterize what sort of molecules can emit SWIR light, we surveyed various "biologically-compatible" compounds, namely: pizza, Coca-Cola, and coffee. For each of these materials, we indeed find significant amounts of SWIR fluorescence, as shown in Figure 7-10. We did not investigate the process further, but hypothesize that the emission arises from various polyaromatic hydrocarbons present due to roasting and caramelization processes. If this emission is sufficiently bright, it is conceivable that food products could be used as contrast agents for SWIR imaging.

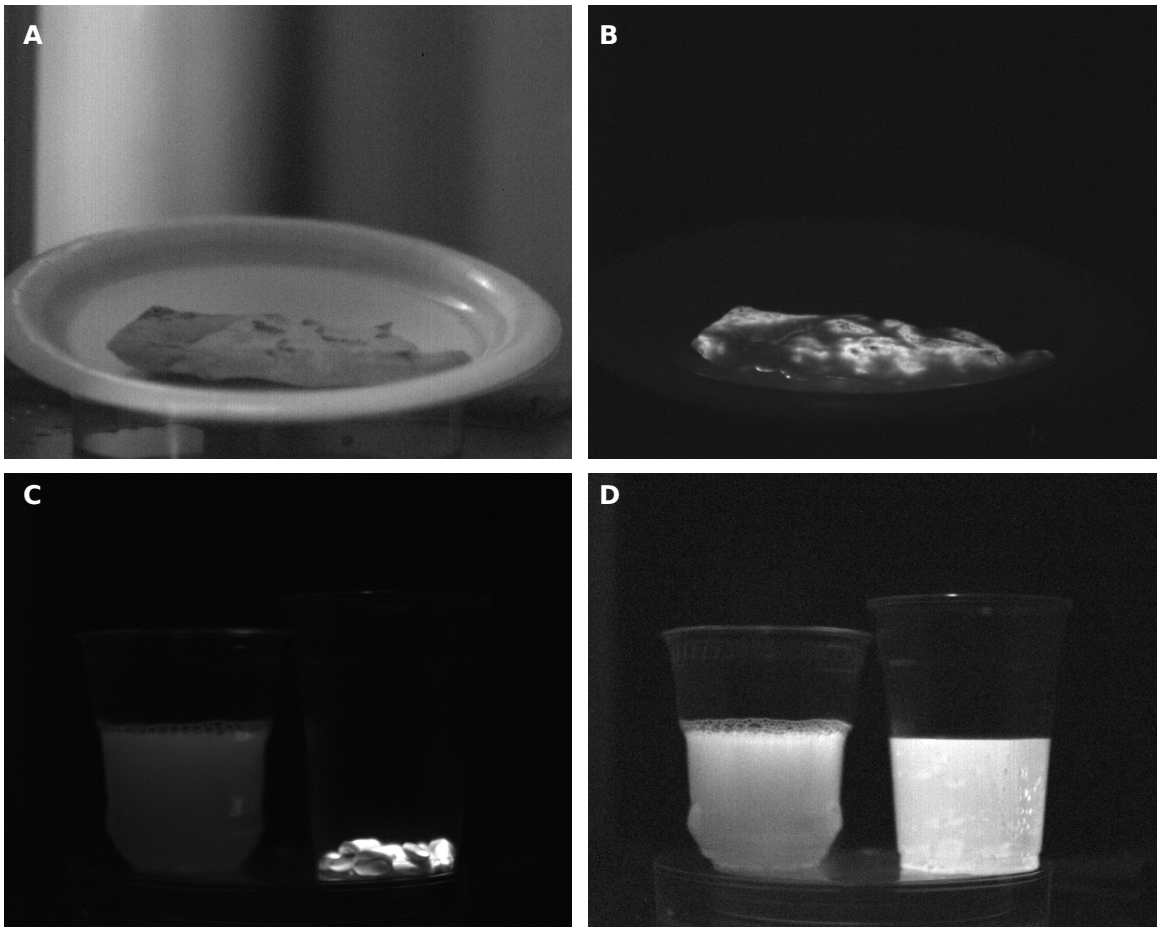


Figure 7-10: All images are collected using a pair of LP1000 nm emission filters. **A** Image of a slice of pizza, illuminated using an incandescent light bulb. **B** The same slice of pizza, under illumination by an 808 nm source. **C** Fluorescence image of brewed coffee (left) and coffee beans (right). **D** Fluorescence image of brewed coffee (left) and Coca-Cola (right). Exposure times vary between each image; the comparisons are meant to be qualitative.

# Chapter 8

# Future Directions

Nearly every line of inquiry leads to interesting diversions, some of which are followed but many of which are put aside for some later time. In this chapter, we discuss some of the more promising ideas which arose during the studies detailed in this thesis, but which were not brought to fruition.

## 8.1 Single-Molecule Measurement of Multiple Exciton Generation Efficiency

In a variety of materials, it is possible to convert a single exciton into multiple excitons, each with some lower amount of energy.[237–251] For nanocrystals this process is known as multiple exciton generation (MEG) and is of particular interest for solar cell applications, for which it is hoped that efficient MEG may be used to harvest energy from short-wavelength light that would otherwise be lost to thermalization. The dynamics and efficiency of MEG are typically measured through ultrafast transient photoluminescence or absorption spectroscopies, in which the extra exciton manifests as a biexciton-like signature which remains even in the limit of low excitation flux.[239] In devices this can manifest an above-unity internal quantum efficiency[252] or excess transient photocurrent. However, all existing studies of MEG in nanocrystals have relied on ensemble methods; is it possible to study MEG in an individual molecule?

There are two potential methods for studying MEG at the single-molecule level: fluorescence lifetime, and photon correlation. A fluorescence lifetime-based measurement would mimic the design of the ensemble experiment: isolate a single emitter, measure the lifetime of its bright-state emission under "red" excitation ($< 2E_g$), and repeat the measurement under "blue" excitation ($> 2E_g$). In the limit of low excitation flux, the lifetime will exhibit a biexciton signal at early times only for the blue excitation, and this difference can be used to quantify the efficiency of MEG. However, the timescale of biexciton relaxation in many lead chalcogenides is on the order of 100 ps, which can be difficult to measure using single-molecule methods due to finite temporal response of single-photon detectors. The advantage of this method is that it is directly analogous to existing experiments, and has a signal which scales linearly with the detection rate.

Alternately, we can measure MEG efficiency using $g^{(2)}$. This signal scales as the square of the emission rate per pulse, but provides the most accurate statistics of biexciton emission. For red excitation, the generation of multexcitons is strictly Poissonian, as described in Chapter 2. But for blue excitation, the absorption of a single photon has some probability of generating two excitons $\Phi(\nu)$. Comparison of $g^{(2)}$ for red and blue excitation allows us to measure $\Phi$.

The extraction of $\Phi$ from $g^{(2)}$ requires modeling akin to that of Chapter 2. If we assume that the multiexciton produced through MEG is equivalent to that produced by multiple successive excitations, we obtain a modified expression for $\chi_n$:

$$\chi_n^{(\Phi)} = \begin{cases} \chi_0; & n = 0 \\ \chi_1 (1 - \Phi); & n = 1 \\ \chi_1 \Phi + \chi_2 (1 - \Phi)^2; & n = 2 \\ \dots \end{cases} \tag{8.1}$$

These new excitation probabilities may be substituted directly into Equation (2.15) to yield a new expression for $g_0^{(2)}$. Treating Poissonian absorption up to the biexciton

and accounting for second-order correlations[1], we obtain:

$$\begin{aligned} \mathrm{G}_1 =& \chi_1 (1-\Phi)\gamma_1 + \left(\chi_1\Phi + \chi_2 (1-\Phi)^2\right)(\gamma_2+\gamma_1) + \\ & 2\chi_2\Phi(1-\Phi)(\gamma_3+\gamma_2+\gamma_1) + \chi_2\Phi^2(\gamma_4+\gamma_3+\gamma_2+\gamma_1) \end{aligned} \tag{8.2}$$

$$\begin{aligned} \mathrm{G}_2/2 =& \left(\chi_1\Phi + \chi_2 (1-\Phi)^2\right)\gamma_2\gamma_1 + \\ & 2\chi_2\Phi(1-\Phi)(\gamma_3\gamma_2+\gamma_3\gamma_1+\gamma_2\gamma_1) + \\ & \chi_2\Phi^2(\gamma_4\gamma_3+\gamma_4\gamma_2+\gamma_4\gamma_1+\gamma_3\gamma_2+\gamma_3\gamma_1+\gamma_2\gamma_1) \end{aligned} \tag{8.3}$$

The effect of MEG is to provide some excess multiexciton signal, such that even "exciton" excitation events now can yield two photons. Equivalently, the average of the Poisson distribution is increased by some amount set by $\Phi$. Under conditions of low excitation flux ($\langle n\rangle \ll 1$) and neglecting $\gamma_{n>2}$, we obtain:

$$g_0^{(2)} = \frac{2(\chi_1\Phi+\chi_2)\gamma_2\gamma_1}{(\chi_1(\gamma_1+\Phi\gamma_2))^2} \tag{8.4}$$

Substituting Poissonian excitation probabilities:

$$\lim_{\langle n\rangle\to 0} g_0^{(2)} = \frac{\gamma_2\gamma_1}{(\gamma_1+\Phi\gamma_2)^2}\left(1+\frac{2\Phi}{\langle n\rangle}\right) \tag{8.5}$$

This has the curious effect of including a $1/\langle n\rangle$ term, such that $g_0^{(2)}$ tends toward $\infty^+$ at low excitation flux (see Figure 8-1). In the case without MEG, the limit approaches $\gamma_2/\gamma_1$ because it is equally probable to obtain two excitations from a single pulse as to obtain two excitations from different pulses. Here, because we now have a mechanism which provides photon pairs with asymptotically higher probability than a pair of excitations, we obtain reduced antibunching and even superbunching under conditions of low excitation flux.

As an unfortunate side effect, this means that we cannot ignore effects of the excitation flux in our experiment. One method for accounting for this is to measure

[1]Note that, in a full treatment of the problem, $\mathrm{G}_1^2$ also contains a leading term of $\chi_1\chi_3$, since the generation of a biexciton on two successive pulses occurs with asymptotically identical probability as the generation of a monoexciton and triexciton.

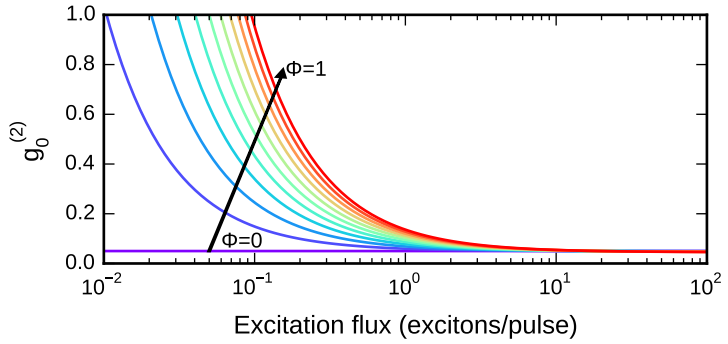


Figure 8-1: The variation of $g_0^{(2)}$ with excitation flux and MEG efficiency. Here, $\gamma_1 = 1$ and $\gamma_2 = 0.05$.

$g_0^{(2)}$ for a variety of $\langle n \rangle$, and to fit the result to Equation (8.5) using $\gamma_2$, $\gamma_1$, and $\Phi$ as free parameters. Such an experiment is quite ambitious for single-molecule spectroscopy, because while some champion nanocrystals provide sufficient signal for detailed analysis under a number of different conditions (Chapter 6), these are rare even among well-developed materials such as CdSe.

A more immediately practical approach to measuring $\Phi$ is to use a solution-based method akin to the method of Beyler et al.[75]. The use of nanocrystal solutions greatly simplifies the experimental requirements by eliminating the need for any single molecule to survive prolonged experimentation, and while this would not be an experiment on an individual molecule it would return the ensemble-averaged single-molecule MEG efficiency. The advantage over existing lifetime-based methods is that we can directly measure the biexciton statistics induced by MEG, regardless of the temporal dynamics of the multiexcitons (see Section 8.2 for such details).

That being said, S-$\lambda$-$g^{(2)}$ is complicated by the fact that we must explicitly consider $\langle n \rangle$. When studying an individual molecule on a substrate, the focal volume is defined primarily by the overlap of the excitation source and the molecule, since no other emitters are nearby. In a solution measurement the focal volume is defined by the overlap of the excitation source and the detection scheme, and as such there is some probability distribution for detecting emission from molecules which experience some variety of $\langle n \rangle$. In Beyler et al.[75] it was possible to average over the focal volume to

obtain the following result:

$$\frac{g^{(2)}(0)-1}{g^{(2)}(T_{\text{rep}})-1}=\frac{\langle\gamma_2\gamma_1\rangle}{\langle\gamma_1\gamma_1\rangle} \tag{8.6}$$

In principle it may be possible to obtain an analogous result which accounts for MEG, but it is not immediately clear that this is analytically straightforward. For the same reason, S-$g^{(3)}$ is a non-trivial task.

### 8.1.1 Practical Considerations for an S-$\lambda$-$g^{(2)}$ Study

Let us suppose that we are interested in studying MEG in some material through solution-$g^{(2)}$. Given the excited-state lifetime of the material, we must select a repetition rate $f$ which is sufficiently low to prevent re-excitation by successive pulses. For lead chalcogenides the excited state lifetime is on the order of 1 µs, and thus $f$ should be on the order of magnitude of 100 kHz[2]. Next, we must measure $g^{(2)}$ for some excitation flux $\langle n\rangle$ – probably several – with some average focal volume occupation $\langle N\rangle$. This emission is detected with some probability $\xi$. This gives us an average single-photon detection rate of approximately:

$$\mathrm{G}_1=\langle n\rangle\ \langle N\rangle\,\xi+k_{\text{dark}}/f \tag{8.7}$$

Our side peak at $g^{(2)}(\infty)$ grows as $\mathrm{G}_1^2$, but due to the photon bunching induced by the diffusion of molecules through the focal volume we have:

$$g^{(2)}(T_{\text{rep}})\propto\mathrm{G}_1^2\left(1+\frac{1}{\langle N\rangle}\right) \tag{8.8}$$

The center peak also contains the Poissonian background due to the free diffusion of nanocrystals:

$$g^{(2)}(0)\propto\mathrm{G}_1^2+\mathrm{G}_2\frac{1}{\langle N\rangle} \tag{8.9}$$

[2]The value of $f$ sets the probability that an excited nanocrystal will be re-excited, or that the detected photon will be associated with the correct pulse.

Note that both of these expressions neglect the inhomogeneous excitation throughout the focal volume, and are meant as approximations of the true count rates. So long as $T_{\mathrm{rep}}$ is sufficiently small relative to the diffusion time, these expressions are nearly exact,[75] in the absence of MEG.

To estimate the experimental time necessary to measure $\gamma_2$ and other parameters with sufficient precision, we can substitute reasonable estimated values. Let us suppose we wish to measure $g_0^{(2)}$ to a percent precision, for experimental parameters of: $\langle n \rangle = 0.3$, $\langle N \rangle = 1$, $\xi = 0.02$[3], $k_{\mathrm{dark}} = 400\,\mathrm{cps}$, and $f = 100\,\mathrm{kHz}$. This gives $10^{-2}$ counts per pulse, for a Poissonian background rate ($\mathrm{G}_1^2$) of 10 pairs per second. To measure this background to a percent in shot noise we must measure at least $10^4$ counts, or 1000 s integration (17 min). On top of this signal is the single-molecule contribution, which grows in at a count rate which goes as $1/\langle N \rangle$. The side peak $g^{(2)}(T_{\mathrm{rep}})$ grows at double the rate for $\langle N \rangle = 1$, but the center peak $g^{(2)}(0)$ is generally a relatively weak signal. For $\gamma_2 = 0.1$, this peak grows at one-tenth the rate of the background, such that we need $10^4$ s to measure its rate to 1 % precision.

As we can see, precise measurements through S-$g^{(2)}$ generally require more experimental time than equivalent SM-$g^{(2)}$ measurements due to the need to precisely measure the Poissonian background. The advantage of S-$g^{(2)}$ is determinism: given a working setup and known experimental parameters, S-$g^{(2)}$ will be complete in a predictable amount of time, while SM-$g^{(2)}$ can only proceed as rapidly as it is possible to find and examine long-lived nanocrystals. Particularly since the measurement of MEG through $g^{(2)}$ requires repeated measurements of the same sample, solution-based experiments are far more appealing.

Given all of this, a successful S-$\lambda$-$g^{(2)}$ study will most likely follow equivalent procedures to those used in Beyler et al.[75]. First, we must measure $g_0^{(2)}$ ratio under some sub-MEG excitation. To verify this measurement, it should be repeated for a variety of excitation fluxes and sample concentrations, to ensure that these parameters

[3]Free-space Si SPAD microscopes can have system efficiencies of 8 % (see Chapter 6). Infrared systems are not as efficient due to fiber coupling or detector losses, but InGaAs SPAD efficiency has improved dramatically in recent years. The estimation of 2 % here is what has been achieved with a fiber-coupled SNSPD microscope.[45]

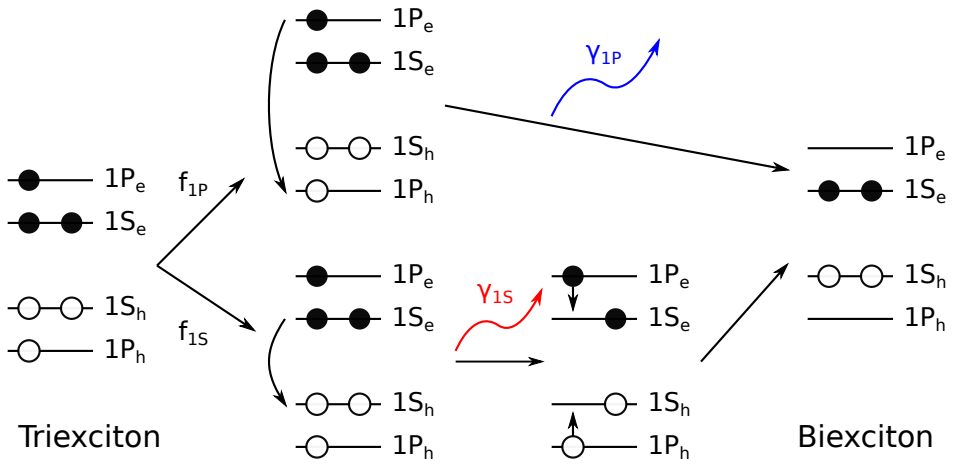


Figure 8-2: Possible mechanisms of relaxation for the CdSe triexciton. In the upper pathway, two 1P carriers recombine with probability $f_{1P}$ to yield blue-shifted emission (relative to the monoexciton) with quantum yield $\gamma_{3,1P}$. In the lower pathway, the band-edge "biexciton" recombines to yield a photon with quantum yield $\gamma_{3,1S}$.

are calibrated correctly and that sample aggregation is not a problem. Finally, under MEG-capable excitation we must measure $g_0^{(2)}$ for a variety of average excitation fluxes $\langle n \rangle$. Using these measured values for $\gamma_2$, $\gamma_1$, and $\langle n \rangle$, we can fit the data to an analogue of Equation (8.5) with $\Phi$ as the free parameter.

## 8.2 Is the Triexciton a Cooperative State, Or a Collection of a Biexciton and an Additional Exciton?

For CdSe the electronic structure of the excitonic states is fairly well-characterized, and the band-edge behavior of the biexciton is also fairly well-understood. But as we become increasingly capable of synthesizing confined materials which support efficient multiexciton emission[55,253] we can now study the dynamics and statistics of these high-order excited states much more easily than before.[46,52,145,150,151]

One experiment of interest for materials such as gradient-shell QD[253] is the measurement of triexciton quantum yield by $g^{(3)}$, and its associated dynamics by PNRL$^{(3)}$. Based on the literature report of $g^{(2)}$ and the accompanying spectral measurements it

seems likely that there will be significant three-photon signal, and the measurement of $g^{(3)}$ will confirm this hypothesis.

Next, we can measure the branching between the possible sources of triexciton emission. In Fisher et al.[151], triexciton emission was identified as the blue-shifted peak evident in transient photoluminescence measurements,[52] associated with the $1\,\mathrm{P_h}{-}1\mathrm{P_e}$ relaxation pathway. But does the triexciton always emit in this fashion, or does this relaxation pathway exist in parallel with the $1\,\mathrm{S_h}{-}1\mathrm{S_e}$ pathway? That is, does the triexciton always emit from the highest-lying excitonic state, or is there some probability that the relaxation occurs through the band-edge "biexciton"? These different possibilities are shown schematically in Figure 8-2.

To definitively answer this question, we can perform a spectrally-resolved $g^{(3)}$ measurement, on a setup with four detectors. In this microscope, we equip three of the detectors with band-pass filters which transmit $1\,\mathrm{S_h}{-}1\mathrm{S_e}$ emission (hereafter 1S), and one detector with a filter for $1\,\mathrm{P_h}{-}1\mathrm{P_e}$ (1P). This is akin to the method of Fisher et al.[151], where $g^{(2)}$ was measured for a 1P-1S correlation, but now we can measure the relative probabilities of detecting three 1S photons ($g^{(3)}_{(1\mathrm{S},1\mathrm{S},1\mathrm{S})}$) or one 1P and two 1S photons ($g^{(3)}_{(1\mathrm{P},1\mathrm{S},1\mathrm{S})}$). If the triexciton is a cooperative state and always emits through the 1P pathway, then $g^{(3)}_{(1\mathrm{S},1\mathrm{S},1\mathrm{S})} = 0$ and $g^{(3)}_{(1\mathrm{P},1\mathrm{S},1\mathrm{S})} = \gamma_3$. If the triexciton emission may arise from the recombination of band-edge carriers, then the two correlations will grow as the relative probabilities of relaxation through either pathway and the quantum yields of each pathway.

We can model the statistics of this spectrally-resolved emission by accounting for all possible triexciton relaxation pathways. To begin with, we will assume that the two-exciton state which remains after triexciton relaxation is identical to a biexciton produced by two successive excitations, and that the pair of photons emitted by the biexciton cascade will pass through the 1S filter. In the absence of state-specific filters $\gamma_3$ may be measured through $g^{(3)}_0$ (see Chapter 6). With state-specific resolution we now have $\gamma_3 = f_{1\mathrm{P}}\gamma_{3,1\mathrm{P}} + f_{1\mathrm{S}}\gamma_{3,1\mathrm{S}}$, where $f$ is the probability that relaxation occurs through the specified pathway and $\gamma_{3,x}$ is the probability of emission during relaxation through the specified pathway.

Treating excitation up to the triexciton, we obtain the following expressions for the correlation rates for each detector:

$$\mathrm{G}_{1,1\mathrm{S}} = \chi_1\gamma_1 + \chi_2\left(\gamma_2+\gamma_1\right) + \chi_3\left(f_{1\mathrm{S}}\gamma_{3,1\mathrm{S}} + \gamma_2 + \gamma_1\right) \tag{8.10}$$

$$\mathrm{G}_{2,(1\mathrm{S},1\mathrm{S})}/2 = \chi_2\gamma_2\gamma_1 + \chi_3\left(f_{1\mathrm{S}}\gamma_{3,1\mathrm{S}}\left(\gamma_2+\gamma_1\right) + \gamma_2\gamma_1\right) \tag{8.11}$$

$$\mathrm{G}_{3,(1\mathrm{S},1\mathrm{S},1\mathrm{S})}/6 = \chi_3 f_{1\mathrm{S}}\gamma_{3,1\mathrm{P}}\gamma_2\gamma_1 \tag{8.12}$$

$$\mathrm{G}_{1,(1\mathrm{P},1\mathrm{S},1\mathrm{S})}/6 = \chi_3 f_{1\mathrm{P}}\gamma_{3,1\mathrm{P}}\gamma_2\gamma_1 \tag{8.13}$$

In the limit of low excitation flux, we obtain the following equivalent $g_0^{(3)}$ expressions:

$$g^{(3)}_{(1\mathrm{P},1\mathrm{S},1\mathrm{S})} = \frac{\mathrm{G}_{1,(1\mathrm{P},1\mathrm{S},1\mathrm{S})}}{\mathrm{G}_{2,(1\mathrm{S},1\mathrm{S})}\mathrm{G}_{1,1\mathrm{S}}} \underset{\langle n\rangle\to 0}{=} \frac{f_{1\mathrm{P}}\gamma_{3,1\mathrm{P}}}{\gamma_1} \tag{8.14}$$

$$g^{(3)}_{(1\mathrm{S},1\mathrm{S},1\mathrm{S})} = \frac{\mathrm{G}_{1,(1\mathrm{S},1\mathrm{S},1\mathrm{S})}}{\mathrm{G}_{2,(1\mathrm{S},1\mathrm{S})}\mathrm{G}_{1,1\mathrm{S}}} \underset{\langle n\rangle\to 0}{=} \frac{f_{1\mathrm{S}}\gamma_{3,1\mathrm{S}}}{\gamma_1} \tag{8.15}$$

This result demonstrates the potential of correlation-based measurements in single-molecule spectroscopy: given an optical phenomenon and a set of conditions which uniquely describe that event, we can apply appropriate post-selection to isolate emission from specific states and measure the statistics or dynamics of the phenomenon.

# Appendix A

# Notes on Designing Single-Molecule Microscopes

The design and implementation of single-molecule microscopes is generally passed down through the generations by the inheritance of existing apparatus. Sometimes designs suitable for one type of measurement are co-opted for other measurements, and it is important for the experimenter to be able to understand what is important to preserve, and what is less important.

In this chapter, we discuss the design criteria and artifacts which were most relevant to the work performed for this thesis. This chapter is not intended to be comprehensive, but instead to document problems which are known, can be solved, and may or may not be common knowledge. All of these issues are discussed in detail in one form or another elsewhere; references are provided where possible. This chapter serves as a guide to the practical aspects of these various phenomena, and a starting point to addressing them experimentally.

## A.1 Optical Elements

### A.1.1 Filters

There are two major classes of color filters: colored glass, and dielectric.

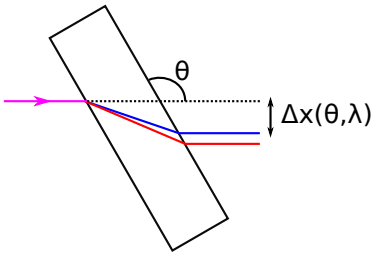


Figure A-1: Lateral chromatic aberration.

Colored glass filters are used for long-pass or band-pass applications and are typically composed of nanocrystals in a silica or other matrix. These tend to be relatively inexpensive but do fluoresce under illumination, and if placed near a detector can overwhelm other signals. They are typically used for ensemble measurements, where this emission is not as significant.

Dielectric filters are composed films of various layers of dielectric materials, designed to interfere constructively or destructively for various wavelengths. These are available for short-, long-, and band-pass applications, and are designed for specific angles of incidence; deviation from the design angle modulates their effective properties. These are the most common filters used in single-molecule experiments, due to their optimal transmission properties and lack of fluorescence.

All dielectric materials can exhibit "ghosting," in which the incident beam will reflect and out-couple several times, yielding several parallel beams. For this reason, many dielectric filters carry anti-reflection coatings to suppress the extra reflections. Some devices actually exploit these reflections, for example in Fabry-Perot interferometers.

### Chromatic Aberration

Color filters are sometimes used at an angle, for example as a dichroic filter for separating excitation and emission. This introduces a lateral displacement of a transmitted beam which is well-described by Snell's law, as a function of the dielectric constant and the thickness of the optic. Due to the wavelength-dependence of the index of refraction of a dielectric, this lateral displacement is also wavelength-dependent. This

chromaticity is especially relevant for fiber-coupling applications, where the target for detection is relatively small (e.g. 9 µm) and exquisitely sensitive to the precise angle and mode of light.

### A.1.2 Focusing Optics

In a microscope, we tend to use focusing optics for several purposes: excitation and emission of samples, spatial filtering of light through a pinhole, coupling to and from fiber optic cables, and focusing onto detectors. This is typically achieved using refractive lenses or curved mirrors. Each of these has benefits and drawbacks, which we discuss here.

Reflective optics are best for broadband throughput of light, since they tend not to introduce wavelength-dependent effects beyond variations in reflectivity. These include off-axis parabolic mirrors, spherical dielectric mirrors, and reflective microscope objectives, all of which are generally available in any number of shapes and sizes. The drawback to off-axis and spherical mirrors in particular is that they introduce significant constraints for alignment, due to the fact that their exact position and angle affect their imaging quality. In contrast, reflective objectives are simple to align using standard on-axis methods but suffer from occlusion due to the suspended second mirror in the center, which leads to a relatively low throughput of light.

Refractive optics are best for narrow-band applications, and are relatively inexpensive. These are available in an astounding variety of shapes, sizes, coatings, and corrections for every conceivable application, and as a result they are the most common focusing optic. However, for broadband applications they suffer from chromatic aberration induced by the variable index of refraction of glass and other materials.[254,255] Essentially, any lens will be designed for some focal length at some wavelength, and deviation from that wavelength will modulate the effective focal length. This variation can be compensated by pairing lenses with compensating indices of refraction, but ultimately the corrections are only effective for specific ranges of wavelengths.

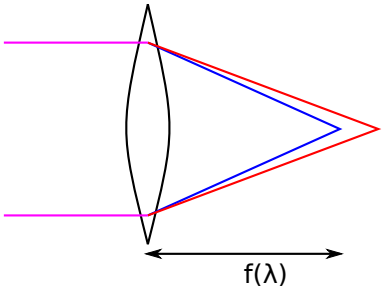


Figure A-2: Focal-length chromatic aberration.

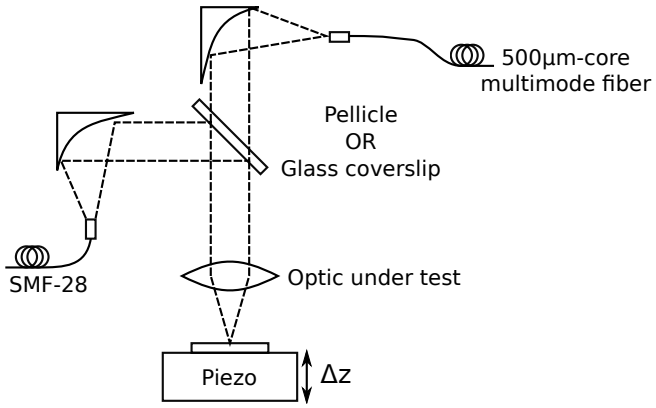


Figure A-3: The microscope setup used for chromatic aberration measurements. For excitation, we couple the light from an incandescent bulb into a 75 µm-core multimode fiber, then mate this with an SMF-28 patch cable. The off-axis parabolic mirrors are aluminum or gold, and the mirrors are silver. The beamsplitter was initially a pellicle, but these exhibit massive wavelength-variation in the reflected spectrum and so we used a glass coverslip for later measurements. A silver mirror is mounted to a three-axis piezo stage (Mad City Labs; Nano-3D200). The back-reflected light is collected into a large-core multimode fiber and sent to a visible spectrometer (Ocean Optics; HR2000) or SWIR spectrometer (Princeton Instruments; OMA V).

### Focal-Length Chromatic Aberration

In confocal microscopy, the goal of alignment is to overlap the excitation and focal volumes, to achieve maximal excitation fluence at the focus while collecting as much emitted light as possible. For narrow ranges of wavelengths this is relatively simple, but for broadband applications the optics may limit the effective transmitted spectrum due to chromatic aberration. As shown in Figure A-2, broadband collimated light will focus at different distances when passed through a lens. Conversely, a point source at a given distance will yield varying degrees of divergence when imaged using

the lens, and unless this dispersion is compensated for the measured spectrum will be inaccurate.

Unfortunately, custom optics for an emerging application can be prohibitively expensive, but in many cases it is actually sufficient to use readily-available and inexpensive optics. For example, when constructing the SWIR microscope used by Correa et al.[43], the authors used an inexpensive Nikon objective designed for visible light, and compensated the excitation source to more effectively overlap with the emission volume. However, one important question remains: is the measured emission affected by the chromaticity near the emission spectrum? If we have access to the specifications for an objective, this can be modeled reasonably well, but in many cases vendors are not willing to part with such information.

To measure the chromaticity of our objectives, we constructed the setup shown in Figure A-3. In this setup, the objective under test is position orthogonal to the optical path in front of a mirror, and the distance between these optics is varied. At each relative displacement we measure the transmission spectrum of a broadband source, and at the focal length for a given wavelength we observe maximum back-reflection. With this measurement of the focal length as a function of wavelength we can correctly overlap the excitation and emission volumes, and determine the effective transfer function for the optic. Note that this measurement does not yield the absolute transmission spectrum, only the relative spectrum.

For the objective used in our SWIR single-molecule measurements,[43,45] we obtained the chromatic aberration in Figure A-4. For this objective, there is a $\approx 13\,\mu m$ displacement between the typical 633 nm excitation and $\approx 1300\,nm$ emission. To compensate for this displacement, we install the sample, optimize back-refection of the excitation source (detected on a shear plate interferometer), and move the sample $13\,\mu m$ further from the objective. Next we install a compensating lens upstream of the objective, and finally optimize its position relative to the objective such that the back-reflection through the lens is collimated.

As for the effective transmission spectrum, we find a roughly 200 nm 3 dB bandwidth at 1300 nm, which is slightly smaller than the true effective spectrum since we

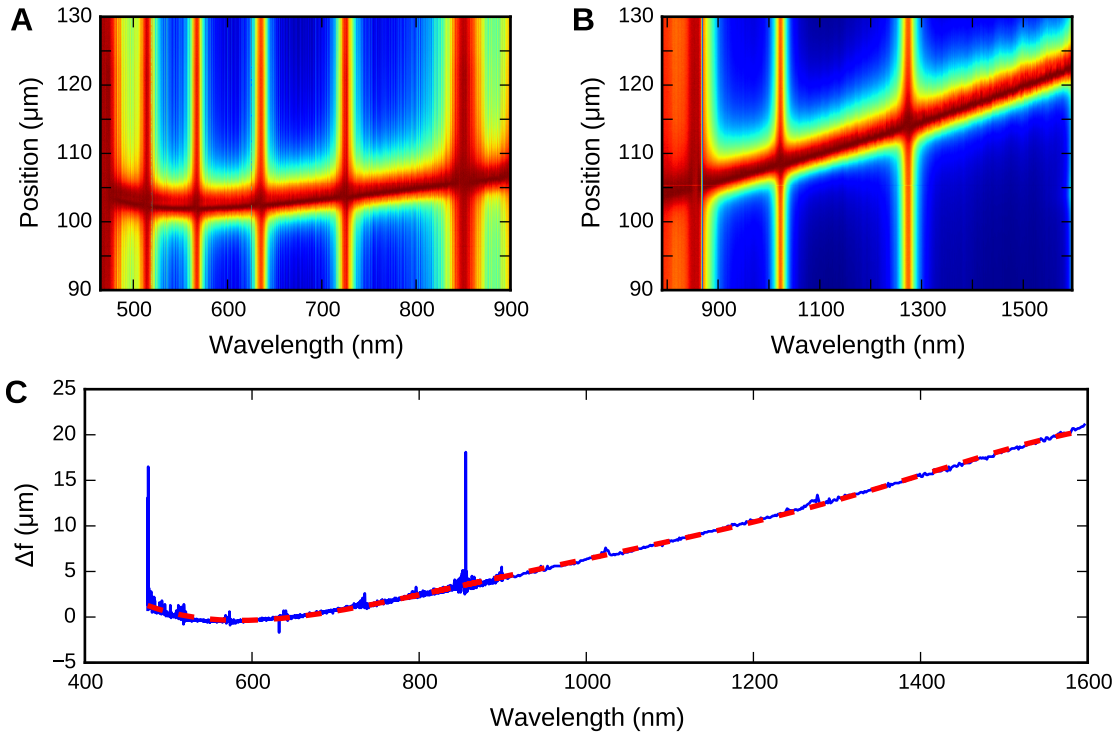


Figure A-4: Focal-length chromaticity of the Nikon 100x oil-immersion objective used for SWIR single-molecule microscopy at Lincoln Laboratory ($f = 170\,\mu\text{m}$). **A**, **B** Back-reflection data for the visible and SWIR spectra, respectively, normalized to the position of maximum intensity for each wavelength. For the SWIR measurement a LP850 nm emission filter was used to suppress wavelength-doubling. The vertical stipes are caused by the wavelength-dependent reflection of the pellicle beamsplitter used in this experiment. **C** The position of maximum back-reflection, which is the effective focal length for each wavelength. The displacement is measured relative to the effective focal length at 633 nm, and the dashed red line is the fit to the dispersion: $\Delta f\,(x = \lambda - 633\,\text{nm}) = -0.1651 + 8.182 \times 10^{-3}x + 7.107 \times 10^{-5}x^2 + 1.992 \times 10^{-7}x^3 + 2.49 \times 10^{-10}x^4 - 1.08 \times 10^{-13}x^5$.

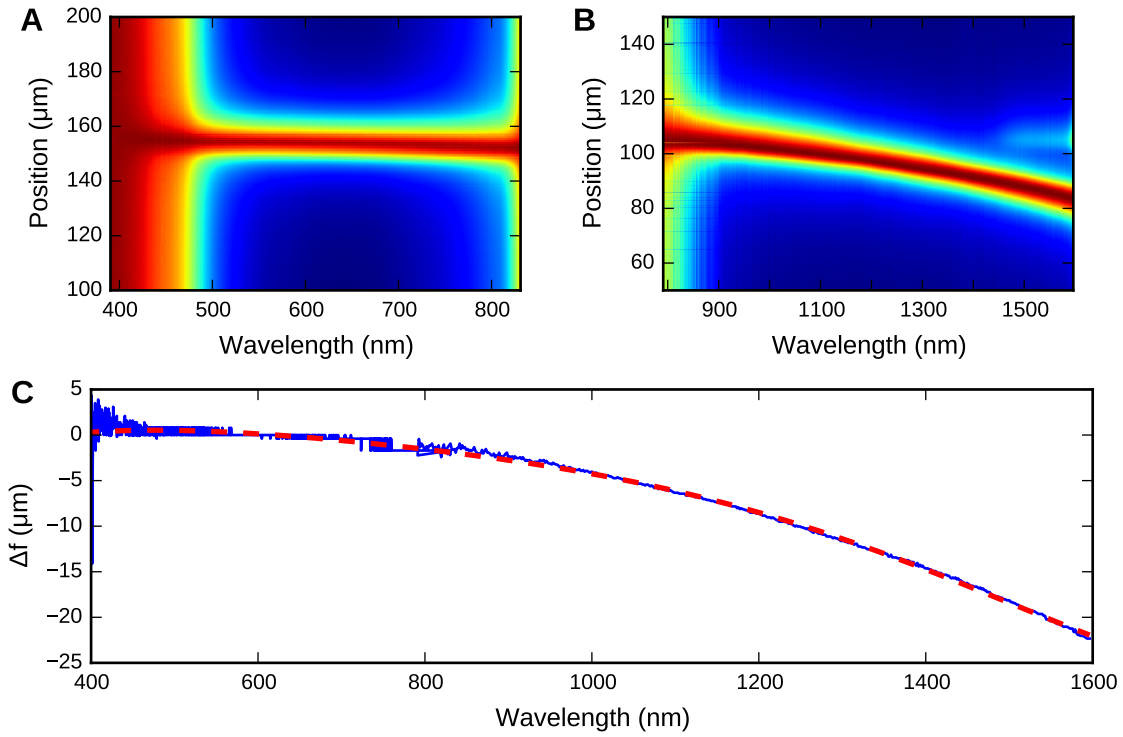


Figure A-5: Focal-length chromaticity of the Nikon Plan Apo IR 60x λS water-immersion objective used for SWIR microscopy at MIT ($f = 170\,\mu\text{m}$). **A**, **B** Back-reflection data for the visible and SWIR spectra, respectively, normalized to the position of maximum intensity for each wavelength. The secondary feature around 1600 nm in the SWIR measurement arises due to wavelength-doubling of $\approx 800\,\text{nm}$ light. **C** The position of maximum back-reflection, which is the effective focal length for each wavelength. The displacement is measured relative to the effective focal length at 633 nm, and the dashed red line is the fit to the dispersion: $\Delta f\,(x = \lambda - 633\,\text{nm}) = -7.703 \times 10^{-2} - 6.848 \times 10^{-2}x - 1.416 \times 10^{-5}x^2 + 2.064 \times 10^{-8}x^3 - 5.397 \times 10^{-11}x^4 + 3.121 \times 10^{-14}x^5$.

have passed through the objective twice. This effective bandwidth is larger than our typical emission spectrum, so the throughput should be of reasonable fidelity.

We also measured the chromatic aberration of a Nikon Plan Apo IR 60x $\lambda$S water-immersion objective (Figure A-5), akin to the 40x one used for SWIR bio-microscopy. This objective features corrections suitable for two-photon microscopy, such that its dispersion is relatively flat for 400–1000 nm, but these corrections fall off dramatically as we reach longer wavelengths.

Ultimately, the objectives characterized here had sufficient throughput for our experiments, even outside their design spectrum. Without knowing these properties, however, we would have been plagued with a lingering doubt about the fidelity of our optics, which should never be a concern in single-molecule microscopy: the sample is predisposed to yielding confusing and unexpected information, so there is no reason to complicate matters by permitting your optics to do so as well.

## A.2 Detectors

In the ideal single-molecule experiment, we would be able to determine the precise state of the molecule over time. In reality we can only obtain limited information about the state based on its emission wavelength, timing, and rate, and as such we employ various detection technologies to optimally achieve resolution of one or more of these properties.

### A.2.1 Single-Photon Detectors

For measurements in which we wish to achieve maximal temporal resolution, single-photon detectors are the best option. These devices are based one of several avalanche processes,[89] which transform the current or other detectable parameter generated by the arrival of a photon into a macroscopic electronic signal which may be timed with appropriate hardware.

In our laboratory, we have access to Si and InGaAs single-photon avalanche photodiodes (SPAD), and superconducting nanowire single-photon detectors (SNSPD[90]).

These detectors exhibit a variety of artifacts,[256,257] some of which are described here. For a more complete understanding of the physics, see the excellent thesis of Fishburn[258].

### Sensitivity to Focus

For Excelitas (formerly Perkin-Elmer) single-photon counting modules (SPCM), the most common SPAD in our laboratory, the responsivity of the device varies with the spatial mode and position of the incident light.[259] This is a direct consequence of the use of a planar device geometry,[258] such that the transit time of the photogenerated carriers varies with the distance between the excitation region and the electrodes. This is mitigated the by use of a stacked geometry,[258] as found in Micro Photon Devices PDM modules.

Practically speaking, as a laser is scanned across the center of the active area of an SPCM it is not unusual to find a modulation of $\approx 10\,\%$ in count rate and a shift of the instrument response function from $\approx 200\,\mathrm{ps}$ to $\approx 300\,\mathrm{ps}$. As a result, for measurements of emission lifetime it is critical to ensure that the emission is focused appropriately and stably onto the detector, and it is not worthwhile to try to measure lifetimes on the order of the IRF with these detectors. The PDM modules are far easier to work with when measuring relatively fast lifetimes, but are a bit less sensitive.

### Afterpulsing

When a detection event is registered, there are a number of processes which can trigger some later false detection event. This is known as afterpulsing, and manifests as a strong signal in the autocorrelation of counts from a single detection channel.

For SPAD these events are largely the result of long-lived trapped carriers. Typical Si SPAD have afterpulsing probabilities of $\approx 0.1$–$1\,\%$ depending on the exact device and dead time, with some dependence on the excitation wavelength and detection rate. For InGaAs SPAD this rate is significantly higher, leading to dead times on the order of $10\,\mu\mathrm{s}$.

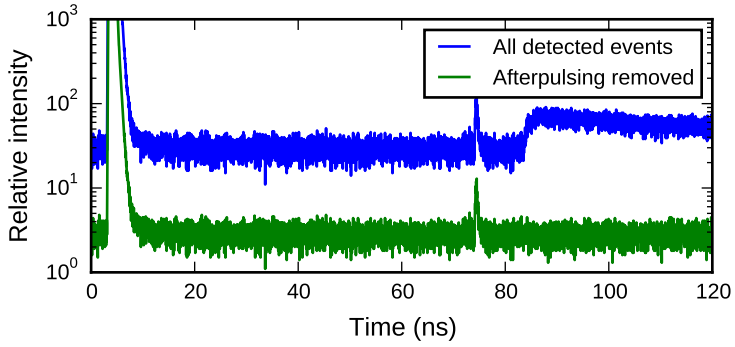


Figure A-6: The measured lifetime of all detected arrival events (blue) and the measured lifetime of the same events with afterpulsing removed (green). The two lifetimes are offset by a factor of 10 for clarity, and the afterpulsing accounts for 211283 of 65968422 recorded events (0.3%). The peak around 75 ns is an optical reflection of about −40 dB maximum intensity relative to the primary laser signal.

Interestingly, for PMTs one of the largest sources of afterpulsing results from the ejected electrons ionizing a helium atom, which then collides with the electrode and yields another detection event.[260]

Afterpulsing may be removed from photon arrival-time data with high fidelity by applying a temporal filter (time gating). To demonstrate this, we sent light from a 532 nm pulsed diode laser (2.5 MHz) through a microscope and detected it with several Si SPAD, using a HydraHarp to record the arrival times in t3 mode. Calculating the lifetime of these photons yields the blue curve of Figure A-6, where the peak around 85 ns arises from afterpulsing. To suppress afterpulsing, we instead calculate the lifetime for only first detection event per pulse on each channel, yielding the green curve of Figure A-6 (see Section 3.2.3 for the algorithm). This provides data limited only by the dark counts (the background) and any stray reflections in the setup (the peak around 75 ns).

### SPAD Cross-Talk

When an avalanche is triggered in an SPAD, some number of photons may be emitted; for a Si SPAD, these appear to be $\approx 800$ nm. For a setup with a single detector this emission is not generally relevant, but in setups with two or more detectors aligned to a

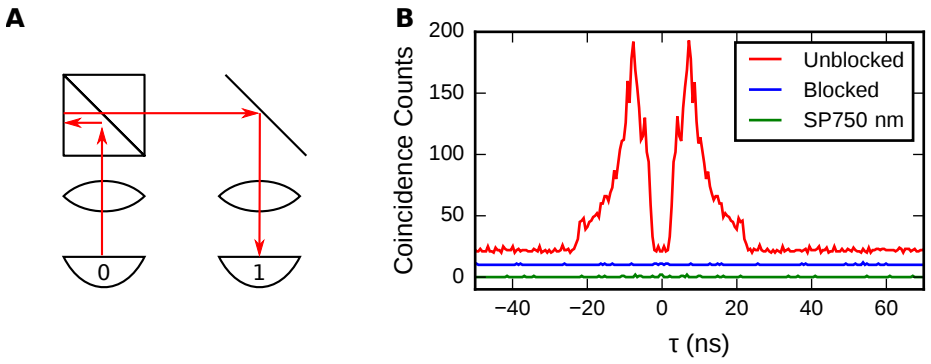


Figure A-7: Examples of the effects of cross-talk. **A** A typical two-detector scheme used for measuring $g^{(2)}$, with a potential cross-talk path drawn in red. In our visible-light setup, the internal reflection drawn here is enhanced due to the mismatch between the anti-reflection coating and the detector emission wavelength. **B** After aligning the detectors to incoming signal, we turn on the detectors and measure coincidence counts ($\propto g^{(2)}$) for several hours and obtain the red curve. After blocking the optical path between the detectors with an opaque object (blue curve) or a SP750 nm filter (green curve), we suppress the cross-talk. Curves are offset for clarity.

single incoming signal, photons emitted by one detector may be detected on the other. This cross-talk manifests in a $g^{(2)}$ as a pair of sharp peaks at delays corresponding to the optical distance between the two detectors (Figure A-7). This can be effectively removed by filtering light $> 750$ nm between the detectors, for example with a "cold" mirror. We have never measured the cross-talk properties for the InGaAs detector because we only have one, but for future experiments in which two are used it is essential to account for this artifact at short relative delays. See Fishburn[258] for the properties of similar devices.

### SNSPD Thermal Artifacts

If the detector is not cooled sufficiently or the detector is normal (not superconducting) for too long, the temporary resistance of the nanowire will heat the nearby substrate. For multi-element detectors fabricated in close proximity this can yield false detection events. These have structure similar to that seen for SPAD, except that the physically-neighboring elements exhibit a stronger correlation than next-nearest or further neighbors. This is suppressed by operating the detectors under

conditions which minimize the reset time, i.e. the time the filaments spend in the resistive state. As the cryostat ages and the operating temperature rises, it is also common to see 1 Hz noise as a result of the compressor frequency: as the substrate heats between pumping cycles, the dark count rate increases.

# Appendix B

# Miscellaneous Data

Over the course of this thesis, there were several projects which never came to fruition, and a few one-off experiments which were not published. In this Appendix, we document some results which are complete but are unlikely to otherwise be published.

## B.1 The Emission Lifetime of $Cd_3As_2$

While working with Daniel Harris and Oliver Bruns, we were interested in comparing the brightness of various nanocrystal materials and organic dyes, as a way of assessing whether a particular system would be of interest. During this process, Dan realized that we had never measured the emission lifetime of $Cd_3As_2$, and so we used the SNSPD microscope to do so (see Figure B-1). This sample had an emission lifetime of 180 ns.

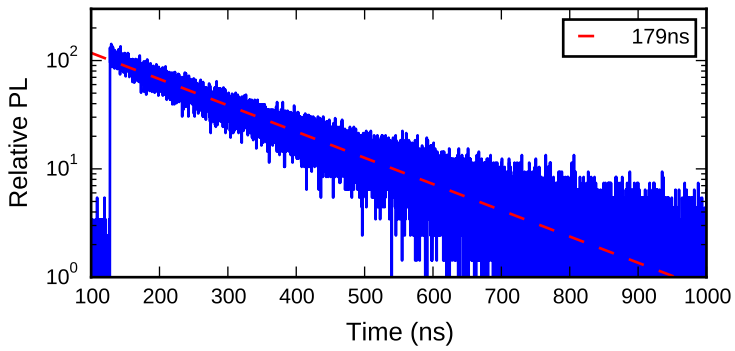


Figure B-1: Emission lifetime of a sample of $Cd_3As_2$ crystals, provided by Dan Harris. The sample was prepared on a glass substrate, excited using a 633 nm diode laser, and detected using an SNSPD. The fit to a single exponential gives a lifetime of 180 ns.

# Bibliography


[1] Murray, C. B.; Norris, D. J.; Bawendi, M. G. Synthesis and characterization of nearly monodisperse CdE (E=S, Se, Te) semiconductor nanocrystallites. *J. Am. Chem. Soc.* **1993**, *115*, 8706–8715.

[2] Chen, O.; Wei, H.; Maurice, A.; Bawendi, M.; Reiss, P. Pure colors from core–shell quantum dots. *MRS Bull.* **2013**, *38*, 696–702.

[3] Lhuillier, E.; Keuleyan, S.; Liu, H.; Guyot-Sionnest, P. Mid-IR Colloidal Nanocrystals. *Chem. Mater.* **2013**, *25*, 1272–1282.

[4] Bigioni, T. P.; Whetten, R. L.; Dag, O. Near-Infrared Luminescence from Small Gold Nanocrystals. *J. Phys. Chem. B* **2000**, *104*, 6983–6986.

[5] Link, S.; Beeby, A.; FitzGerald, S.; El-Sayed, M. A.; Schaaff, T. G.; Whetten, R. L. Visible to Infrared Luminescence from a 28-Atom Gold Cluster. *J. Phys. Chem. B* **2002**, *106*, 3410–3415.

[6] Zheng, J.; Petty, J. T.; Dickson, R. M. High Quantum Yield Blue Emission from Water-Soluble $Au_8$ Nanodots. *J. Am. Chem. Soc.* **2003**, *125*, 7780–7781.

[7] Zheng, J.; Zhang, C.; Dickson, R. M. Highly Fluorescent, Water-Soluble, Size-Tunable Gold Quantum Dots. *Phys. Rev. Lett.* **2004**, *93*, 077402.

[8] Zheng, J.; Nicovich, P. R.; Dickson, R. M. Highly Fluorescent Noble-Metal Quantum Dots. *Annu. Rev. Phys. Chem.* **2007**, *58*, 409–431.

[9] Lin, C.-A. J.; Yang, T.-Y.; Lee, C.-H.; Huang, S. H.; Sperling, R. A.; Zanella, M.; Li, J. K.; Shen, J.-L.; Wang, H.-H.; Yeh, H.-I.; Parak, W. J.; Chang, W. H. Synthesis, Characterization, and Bioconjugation of Fluorescent Gold Nanoclusters toward Biological Labeling Applications. *ACS Nano* **2009**, *3*, 395–401.

[10] Andolina, C. M.; Dewar, A. C.; Smith, A. M.; Marbella, L. E.; Hartmann, M. J.; Millstone, J. E. Photoluminescent Gold–Copper Nanoparticle Alloys with Composition-Tunable Near-Infrared Emission. *J. Am. Chem. Soc.* **2013**, *135*, 5266–5269.

[11] Marbella, L. E.; Andolina, C. M.; Smith, A. M.; Hartmann, M. J.; Dewar, A. C.; Johnston, K. A.; Daly, O. H.; Millstone, J. E. Gold-Cobalt Nanoparticle Alloys

Exhibiting Tunable Compositions, Near-Infrared Emission, and High $T_2$ Relaxivity. *Adv. Funct. Mater.* **2014**, *24*, 6532–6539.

[12] Anderson, N. C.; Owen, J. S. Soluble, Chloride-Terminated CdSe Nanocrystals: Ligand Exchange Monitored by $^{1}H$ and $^{31}P$ NMR Spectroscopy. *Chem. Mater.* **2013**, *25*, 69–76.

[13] Gao, Y.; Peng, X. Photogenerated Excitons in Plain Core CdSe Nanocrystals with Unity Radiative Decay in Single Channel: The Effects of Surface and Ligands. *J. Am. Chem. Soc.* **2015**, *137*, 4230–4235.

[14] Dabbousi, B. O.; Rodriguez-Viejo, J.; Mikulec, F. V.; Heine, J. R.; Mattoussi, H.; Ober, R.; Jensen, K. F.; Bawendi, M. G. (CdSe)ZnS Core-Shell Quantum Dots: Synthesis and Characterization of a Size Series of Highly Luminescent Nanocrystallites. *J. Phys. Chem. B* **1997**, *101*, 9463–9475.

[15] Owen, J. S.; Park, J.; Trudeau, P.-E.; Alivisatos, A. P. Reaction Chemistry and Ligand Exchange at Cadmium–Selenide Nanocrystal Surfaces. *J. Am. Chem. Soc.* **2008**, *130*, 12279–12281.

[16] Somorjai, G. A.; Li, Y. In *Introduction to Surface Chemistry and Catalysis*; 2nd,, Ed.; John Wiley & Sons, Inc., 2010.

[17] Cossairt, B. M.; Owen, J. S. CdSe Clusters: At the Interface of Small Molecules and Quantum Dots. *Chem. Mater.* **2011**, *23*, 3114–3119.

[18] Cossairt, B. M.; Juhas, P.; Billinge, S. J. L.; Owen, J. S. Tuning the Surface Structure and Optical Properties of CdSe Clusters Using Coordination Chemistry. *J. Phys. Chem. Lett.* **2011**, *2*, 3075–3080.

[19] Anderson, N. C.; Hendricks, M. P.; Choi, J. J.; Owen, J. S. Ligand Exchange and the Stoichiometry of Metal Chalcogenide Nanocrystals: Spectroscopic Observation of Facile Metal-Carboxylate Displacement and Binding. *J. Am. Chem. Soc.* **2013**, *135*, 18536–18548.

[20] Wolcott, A.; Schiros, T.; Trusheim, M. E.; Chen, E. H.; Nordlund, D.; Diaz, R. E.; Gaathon, O.; Englund, D.; Owen, J. S. Surface Structure of Aerobically Oxidized Diamond Nanocrystals. *J. Phys. Chem. C* **2014**, *118*, 26695–26702.

[21] Hwang, G. W. Surface Trap Passivation and Characterization of Lead Sulfide Quantum Dots for Optical and Electrical Applications. Ph.D. thesis, Massachusetts Institute of Technology, 2015.

[22] Owen, J. The coordination chemistry of nanocrystal surfaces. *Science* **2015**, *347*, 615–616.

[23] LaMer, V. K.; Dinegar, R. H. Theory, Production and Mechanism of Formation of Monodispersed Hydrosols. *J. Am. Chem. Soc.* **1950**, *72*, 4847–4854.

[24] La Mer, V. K.; Dinegar, R. H. The Limiting Degrees of Supersaturation of the Sparingly Soluble Sulfates. *J. Am. Chem. Soc.* **1951**, *73*, 380–385.

[25] Harris, D. K.; Bawendi, M. G. Improved Precursor Chemistry for the Synthesis of III–V Quantum Dots. *J. Am. Chem. Soc.* **2012**, *134*, 20211–20213.

[26] Harris, D. K. Synthesis and Characterization of Infrared Quantum Dots. Ph.D. thesis, Massachusetts Institute of Technology, 2014.

[27] Park, J.; Joo, J.; Kwon, S. G.; Jang, Y.; Hyeon, T. Synthesis of monodisperse spherical nanocrystals. *Angew. Chem. Int. Ed.* **2007**, *46*, 4630–4660.

[28] Xia, Y.; Xiong, Y.; Lim, B.; Skrabalak, S. E. Shape-Controlled Synthesis of Metal Nanocrystals: Simple Chemistry Meets Complex Physics? *Angew. Chem. Int. Ed.* **2009**, *48*, 60–103.

[29] Li, H.; Brescia, R.; Krahne, R.; Bertoni, G.; Alcocer, M. J. P.; D'Andrea, C.; Scotognella, F.; Tassone, F.; Zanella, M.; De Giorgi, M.; Manna, L. Blue-UV-Emitting ZnSe(Dot)/ZnS(Rod) Core/Shell Nanocrystals Prepared from CdSe/CdS Nanocrystals by Sequential Cation Exchange. *ACS Nano* **2012**, *6*, 1637–1647.

[30] Beberwyck, B. J.; Surendranath, Y.; Alivisatos, A. P. Cation Exchange: A Versatile Tool for Nanomaterials Synthesis. *J. Phys. Chem. C* **2013**, *117*, 19759–19770.

[31] Son, D. H.; Hughes, S. M.; Yin, Y.; Alivisatos, A. Paul. Cation Exchange Reactions in Ionic Nanocrystals. *Science* **2004**, *306*, 1009–1012.

[32] Mirkin, C. A.; Letsinger, R. L.; Mucic, R. C.; Storhoff, J. J. A DNA-based method for rationally assembling nanoparticles into macroscopic materials. *Nature* **1996**, *382*, 607–609.

[33] Ferry, V. E.; Smith, J. M.; Alivisatos, A. P. Symmetry Breaking in Tetrahedral Chiral Plasmonic Nanoparticle Assemblies. *ACS Photonics* **2014**, *1*, 1189–1196.

[34] Nirmal, M.; Dabbousi, B. O.; Bawendi, M. G.; Macklin, J. J.; Trautman, J. K.; Harris, T. D.; Brus, L. E. Fluorescence intermittency in single cadmium selenide nanocrystals. *Nature* **1996**, *383*, 802–804.

[35] Kuno, M.; Fromm, D. P.; Hamann, H. F.; Gallagher, A.; Nesbitt, D. J. Nonexponential "blinking" kinetics of single CdSe quantum dots: A universal power law behavior. *J. Chem. Phys.* **2000**, *112*, 3117–3120.

[36] Kuno, M.; Fromm, D. P.; Hamann, H. F.; Gallagher, A.; Nesbitt, D. J. "On"/"off" fluorescence intermittency of single semiconductor quantum dots. *J. Chem. Phys.* **2001**, *115*, 1028–1040.

[37] Shimizu, K.; Neuhauser, R.; Leatherdale, C.; Empedocles, S.; Woo, K.; Bawendi, M. Blinking statistics in single semiconductor nanocrystal quantum dots. *Phys. Rev. B* **2001**, *63*, 205316.

[38] Bachir, A. I.; Durisic, N.; Hebert, B.; Grutter, P.; Wiseman, P. W. Characterization of blinking dynamics in quantum dot ensembles using image correlation spectroscopy. *J. Appl. Phys.* **2006**, *99*, 064503.

[39] Crouch, C. H.; Sauter, O.; Wu, X.; Purcell, R.; Querner, C.; Drndic, M.; Pelton, M. Facts and Artifacts in the Blinking Statistics of Semiconductor Nanocrystals. *Nano Lett.* **2010**, *10*, 1692–1698.

[40] Malko, A. V.; Park, Y.-S.; Sampat, S.; Galland, C.; Vela, J.; Chen, Y.; Hollingsworth, J. A.; Klimov, V. I.; Htoon, H. Pump-Intensity- and Shell-Thickness-Dependent Evolution of Photoluminescence Blinking in Individual Core/Shell CdSe/CdS Nanocrystals. *Nano Lett.* **2011**, *11*, 5213–5218.

[41] Galland, C.; Ghosh, Y.; Steinbrück, A.; Sykora, M.; Hollingsworth, J. A.; Klimov, V. I.; Htoon, H. Two types of luminescence blinking revealed by spectroelectrochemistry of single quantum dots. *Nature* **2011**, *479*, 203–207.

[42] Galland, C.; Ghosh, Y.; Steinbrück, A.; Hollingsworth, J. A.; Htoon, H.; Klimov, V. I. Lifetime blinking in nonblinking nanocrystal quantum dots. *Nat. Commun.* **2012**, *3*, 908–915.

[43] Correa, R. E.; Dauler, E. A.; Nair, G.; Pan, S. H.; Rosenberg, D.; Kerman, A. J.; Molnar, R. J.; Hu, X.; Marsili, F.; Anant, V.; Berggren, K. K.; Bawendi, M. G. Single Photon Counting from Individual Nanocrystals in the Infrared. *Nano Lett.* **2012**, *12*, 2953–2958.

[44] Galland, C.; Brovelli, S.; Bae, W. K.; Padilha, L. A.; Meinardi, F.; Klimov, V. I. Dynamic Hole Blockade Yields Two-Color Quantum and Classical Light from Dot-in-Bulk Nanocrystals. *Nano Lett.* **2013**, *13*, 321–328.

[45] Bischof, T. S.; Correa, R. E.; Rosenberg, D.; Dauler, E. A.; Bawendi, M. G. Measurement of Emission Lifetime Dynamics and Biexciton Emission Quantum Yield of Individual InAs Colloidal Nanocrystals. *Nano Lett.* **2014**, *14*, 6787–6791.

[46] Fisher, B. R.; Eisler, H.-J.; Stott, N. E.; Bawendi, M. G. Emission Intensity Dependence and Single-Exponential Behavior In Single Colloidal Quantum Dot Fluorescence Lifetimes. *J. Phys. Chem. B* **2004**, *108*, 143–148.

[47] Jha, P. P.; Guyot-Sionnest, P. Trion Decay in Colloidal Quantum Dots. *ACS Nano* **2009**, *3*, 1011–1015.

[48] Qin, W.; Guyot-Sionnest, P. Evidence for the Role of Holes in Blinking: Negative and Oxidized CdSe/CdS Dots. *ACS Nano* **2012**, *6*, 9125–9132.

[49] Qin, W.; Shah, R. A.; Guyot-Sionnest, P. CdSeS/ZnS Alloyed Nanocrystal Lifetime and Blinking Studies under Electrochemical Control. *ACS Nano* **2012**, *6*, 912–918.

[50] Wei, H.; Bruns, O. T.; Chen, O.; Bawendi, M. G. Compact zwitterion-coated iron oxide nanoparticles for in vitro and in vivo imaging. *Integr. Biol.* **2013**, *5*, 108–114.

[51] Beyler, A. P.; Marshall, L. F.; Cui, J.; Brokmann, X.; Bawendi, M. G. Direct Observation of Rapid Discrete Spectral Dynamics in Single Colloidal CdSe-CdS Core-Shell Quantum Dots. *Phys. Rev. Lett.* **2013**, *111*, 177401.

[52] Caruge, J.-M.; Chan, Y.; Sundar, V.; Eisler, H. J.; Bawendi, M. G. Transient photoluminescence and simultaneous amplified spontaneous emission from multiexciton states in CdSe quantum dots. *Phys. Rev. B* **2004**, *70*, 085316.

[53] Louyer, Y.; Biadala, L.; Trebbia, J.-B.; Fernée, M. J.; Tamarat, Ph.; Lounis, B. Efficient Biexciton Emission in Elongated CdSe/ZnS Nanocrystals. *Nano Lett.* **2011**, *11*, 4370–4375.

[54] Nair, G.; Zhao, J.; Bawendi, M. G. Biexciton Quantum Yield of Single Semiconductor Nanocrystals from Photon Statistics. *Nano Lett.* **2011**, *11*, 1136–1140.

[55] Park, Y.-S.; Ghosh, Y.; Chen, Y.; Piryatinski, A.; Xu, P.; Mack, N. H.; Wang, H.-L.; Klimov, V. I.; Hollingsworth, J. A.; Htoon, H. Super-Poissonian Statistics of Photon Emission from Single CdSe-CdS Core-Shell Nanocrystals Coupled to Metal Nanostructures. *Phys. Rev. Lett.* **2013**, *110*, 117401.

[56] Chung, I.; Bawendi, M. G. Relationship between single quantum-dot intermittency and fluorescence intensity decays from collections of dots. *Phys. Rev. B* **2004**, *70*, 165304.

[57] Chung, I.; Witkoskie, J. B.; Cao, J.; Bawendi, M. G. Description of the fluorescence intensity time trace of collections of CdSe nanocrystal quantum dots based on single quantum dot fluorescence blinking statistics. *Phys. Rev. E* **2006**, *73*, 011106.

[58] Jensen, R. A.; Coropceanu, I.; Chen, Y.; Bawendi, M. G. Thermal Recovery of Colloidal Quantum Dot Ensembles Following Photoinduced Dimming. *J. Phys. Chem. Lett.* **2015**, *6*, 2933–2937.

[59] Labeau, O.; Tamarat, P.; Lounis, B. Temperature Dependence of the Luminescence Lifetime of Single CdSe/ZnS Quantum Dots. *Phys. Rev. Lett.* **2003**, *90*, 257404.

[60] Oron, D.; Aharoni, A.; de Mello Donega, C.; van Rijssel, J.; Meijerink, A.; Banin, U. Universal Role of Discrete Acoustic Phonons in the Low-Temperature Optical Emission of Colloidal Quantum Dots. *Phys. Rev. Lett.* **2009**, *102*, 177402.

[61] Biadala, L.; Louyer, Y.; Tamarat, Ph.; Lounis, B. Band-Edge Exciton Fine Structure of Single CdSe Nanocrystals in External Magnetic Fields. *Phys. Rev. Lett.* **2010**, *105*, 157402.

[62] Fernée, M. J.; Tamarat, P.; Lounis, B. Spectroscopy of single nanocrystals. *Chem. Soc. Rev.* **2014**, *43*, 1311–1337.

[63] Cui, J.; Beyler, A. P.; Bischof, T. S.; Wilson, M. W. B.; Bawendi, M. G. Deconstructing the photon stream from single nanocrystals: from binning to correlation. *Chem. Soc. Rev.* **2014**, *43*, 1287–1310.

[64] Berciaud, S.; Cognet, L.; Lounis, B. Photothermal Absorption Spectroscopy of Individual Semiconductor Nanocrystals. *Nano Lett.* **2005**, *5*, 2160–2163.

[65] Vietmeyer, F.; McDonald, M. P.; Kuno, M. Single Nanowire Microscopy and Spectroscopy. *J. Phys. Chem. C* **2012**, *116*, 12379–12396.

[66] McDonald, M. P.; Vietmeyer, F.; Aleksiuk, D.; Kuno, M. Supercontinuum spatial modulation spectroscopy: Detection and noise limitations. *Rev. Sci. Instrum.* **2013**, *84*, 113104.

[67] Vietmeyer, F.; Chatterjee, R.; McDonald, M. P.; Kuno, M. Concerted single-nanowire absorption and emission spectroscopy: Explaining the origin of the size-dependent Stokes shift in single cadmium selenide nanowires. *Phys. Rev. B* **2015**, *91*, 085422.

[68] Jensen, R. A.; Huang, I-C.; Chen, O.; Choy, J.; Bischof, T. S.; Lončar, M.; Bawendi, M. G. Optical Trapping and Two-Photon Excitation of Colloidal Quantum Dots using Bowtie Apertures. *Submitted*

[69] Knuth, D. E. In *The Art of Computer Programming*, 2nd ed.; Varga, R. S., Harrison, M. A., Eds.; Addison-Wesley Publishing Company, Inc, 1968; Vol. 1.

[70] Ref. 69, p. 132.

[71] Brown, R. H.; Twiss, R. Q. Correlation between Photons in two Coherent Beams of Light. *Nature* **1956**, *177*, 27–29.

[72] Jechow, A.; Seefeldt, M.; Kurzke, H.; Heuer, A.; Menzel, R. Enhanced two-photon excited fluorescence from imaging agents using true thermal light. *Nature Photon.* **2013**, *7*, 973–976.

[73] Dixon, P. B.; Rosenberg, D.; Stelmakh, V.; Grein, M. E.; Bennink, R. S.; Dauler, E. A.; Kerman, A. J.; Molnar, R. J.; Wong, F. N. C. Heralding efficiency and correlated-mode coupling of near-IR fiber-coupled photon pairs. *Phys. Rev. A* **2014**, *90*, 043804.

[74] Sýkora, J.; Kaiser, K.; Gregor, I.; Bnigk, W.; Schmalzing, G.; Enderlein, J. Exploring Fluorescence Antibunching in Solution To Determine the Stoichiometry of Molecular Complexes. *Anal. Chem.* **2007**, *79*, 4040–4049.

[75] Beyler, A. P.; Bischof, T. S.; Cui, J.; Coropceanu, I.; Harris, D. K.; Bawendi, M. G. Sample-Averaged Biexciton Quantum Yield Measured by Solution-Phase Photon Correlation. *Nano Lett.* **2014**, *14*, 6792–6798.

[76] Basché, T.; Moerner, W. E.; Orrit, M.; Talon, H. Photon antibunching in the fluorescence of a single dye molecule trapped in a solid. *Phys. Rev. Lett.* **1992**, *69*, 1516–1519.

[77] Brunel, C.; Lounis, B.; Tamarat, P.; Orrit, M. Triggered Source of Single Photons based on Controlled Single Molecule Fluorescence. *Phys. Rev. Lett.* **1999**, *83*, 2722–2725.

[78] Lounis, B.; Bechtel, H.; Gerion, D.; Alivisatos, P.; Moerner, W. Photon antibunching in single CdSe/ZnS quantum dot fluorescence. *Chem. Phys. Lett.* **2000**, *329*, 399–404.

[79] Messin, G.; Hermier, J. P.; Giacobino, E.; Desbiolles, P.; Dahan, M. Bunching and antibunching in the fluorescence of semiconductor nanocrystals. *Opt. Lett.* **2001**, *26*, 1891–1893.

[80] Brokmann, X.; Giacobino, E.; Dahan, M.; Hermier, J. P. Highly efficient triggered emission of single photons by colloidal CdSe/ZnS nanocrystals. *Appl. Phys. Lett.* **2004**, *85*, 712–714.

[81] Santori, C.; Pelton, M.; Solomon, G.; Dale, Y.; Yamamoto, Y. Triggered Single Photons from a Quantum Dot. *Phys. Rev. Lett.* **2001**, *86*, 1502–1505.

[82] Santori, C. M. Generation of Nonclassical Light Using Semiconductor Quantum Dots. Ph.D. thesis, Stanford University, 2002.

[83] Schirhagl, R.; Chang, K.; Loretz, M.; Degen, C. L. Nitrogen-Vacancy Centers in Diamond: Nanoscale Sensors for Physics and Biology. *Annu. Rev. Phys. Chem.* **2014**, *65*, 83–105.

[84] Widmann, M.; Lee, S.-Y.; Rendler, T.; Son, N. T.; Fedder, H.; Paik, S.; Yang, L.-P.; Zhao, N.; Yang, S.; Booker, I.; Denisenko, A.; Jamali, M.; Momenzadeh, S. A.; Gerhardt, I.; Ohshima, T.; Gali, A.; Janzén, E.; Wrachtrup, J. Coherent control of single spins in silicon carbide at room temperature. *Nature Mater.* **2015**, *14*, 164–168.

[85] Kimble, H. J.; Dagenais, M.; Mandel, L. Photon Antibunching in Resonance Fluorescence. *Phys. Rev. Lett.* **1977**, *39*, 691–695.

[86] Gillespie, D. T. Exact stochastic simulation of coupled chemical reactions. *J. Phys. Chem.* **1977**, *81*, 2340–2361.

[87] Paul, H. Photon antibunching. *Rev. Mod. Phys.* **1982**, *54*, 1061–1102.

[88] Nair, G. P. Many-body processes in the photophysics of colloidal semiconductor nanocrystals. Ph.D. thesis, Massachusetts Institute of Technology, 2009.

[89] Eisaman, M. D.; Fan, J.; Migdall, A.; Polyakov, S. V. Invited Review Article: Single-photon sources and detectors. *Rev. Sci. Instrum.* **2011**, *82*, 071101.

[90] Dauler, E. A.; Kerman, A. J.; Robinson, B. S.; Yang, J. K.; Voronov, B.; Goltsman, G.; Hamilton, S. A.; Berggren, K. K. Photon-number-resolution with sub-30-ps timing using multi-element superconducting nanowire single photon detectors. *J. Mod. Opt.* **2009**, *56*, 364–373.

[91] Wahl, M.; Gregor, I.; Patting, M.; Enderlein, J. Fast calculation of fluorescence correlation data with asynchronous time-correlated single-photon counting. *Opt. Express* **2003**, *11*, 3583–3591.

[92] Laurence, T. A.; Fore, S.; Huser, T. Fast, flexible algorithm for calculating photon correlations. *Opt. Lett.* **2006**, *31*, 829–831.

[93] Magatti, D.; Ferri, F. Fast Multi-Tau Real-Time Software Correlator for Dynamic Light Scattering. *Appl. Opt.* **2001**, *40*, 4011–4021.

[94] Magatti, D.; Ferri, F. 25 ns software correlator for photon and fluorescence correlation spectroscopy. *Rev. Sci. Instrum.* **2003**, *74*, 1135–1144.

[95] Schaub, E. F2Cor: fast 2-stage correlation algorithm for FCS and DLS. *Opt. Express* **2012**, *20*, 2184–2195.

[96] ALV-GmbH, TechTalk - Multiple Tau Digital Correlation. `http://www.alvgmbh.de/tt_multitau/tt_multitau.html`, Accessed 2015-04-17.

[97] Park, Y.-S.; Malko, A. V.; Vela, J.; Chen, Y.; Ghosh, Y.; García-Santamaría, F.; Hollingsworth, J. A.; Klimov, V. I.; Htoon, H. Near-Unity Quantum Yields of Biexciton Emission from CdSe/CdS Nanocrystals Measured Using Single-Particle Spectroscopy. *Phys. Rev. Lett.* **2011**, *106*, 187401.

[98] Mangum, B. D.; Ghosh, Y.; Hollingsworth, J. A.; Htoon, H. Disentangling the effects of clustering and multi-exciton emission in second-order photon correlation experiments. *Opt. Express* **2013**, *21*, 7419–7426.

[99] Correa, R. E. Seeing The Invisible: Single Molecule Microscopy in the Shortwave Infrared. Ph.D. thesis, Massachusetts Institute of Technology, 2013.

[100] Kim, J. Y.; Voznyy, O.; Zhitomirsky, D.; Sargent, E. H. 25th Anniversary Article: Colloidal Quantum Dot Materials and Devices: A Quarter-Century of Advances. *Adv. Mater.* **2013**, *25*, 4986–5010.

[101] Talapin, D. V.; Lee, J.-S.; Kovalenko, M. V.; Shevchenko, E. V. Prospects of Colloidal Nanocrystals for Electronic and Optoelectronic Applications. *Chem. Rev.* **2010**, *110*, 389–458.

[102] Shirasaki, Y.; Supran, G. J.; Bawendi, M. G.; Bulović, V. Emergence of colloidal quantum-dot light-emitting technologies. *Nature Photon.* **2013**, *7*, 13–23.

[103] Mashford, B. S.; Stevenson, M.; Popovic, Z.; Hamilton, C.; Zhou, Z.; Breen, C.; Steckel, J.; Bulovic, V.; Bawendi, M.; Coe-Sullivan, S.; Kazlas, P. T. High-efficiency quantum-dot light-emitting devices with enhanced charge injection. *Nature Photon.* **2013**, *7*, 407–412.

[104] Alivisatos, P. The use of nanocrystals in biological detection. *Nat. Biotechnol.* **2004**, *22*, 47–52.

[105] Michalet, X.; Pinaud, F. F.; Bentolila, L. A.; Tsay, J. M.; Doose, S.; Li, J. J.; Sundaresan, G.; Wu, A. M.; Gambhir, S. S.; Weiss, S. Quantum Dots for Live Cells, in Vivo Imaging, and Diagnostics. *Science* **2005**, *307*, 538–544.

[106] Han, H.-S.; Martin, J. D.; Lee, J.; Harris, D. K.; Fukumura, D.; Jain, R. K.; Bawendi, M. Spatial Charge Configuration Regulates Nanoparticle Transport and Binding Behavior In Vivo. *Angew. Chem. Int. Ed.* **2013**, *52*, 1414–1419.

[107] Chen, O.; Zhao, J.; Chauhan, V. P.; Cui, J.; Wong, C.; Harris, D. K.; Wei, H.; Han, H.-S.; Fukumura, D.; Jain, R. K.; Bawendi, M. G. Compact high-quality CdSe-CdS core-shell nanocrystals with narrow emission linewidth-sandsuppressed blinking. *Nature Mater.* **2013**, *12*, 445–451.

[108] Chauhan, V. P.; Martin, J. D.; Liu, H.; Lacorre, D. A.; Jain, S. R.; Kozin, S. V.; Stylianopoulos, T.; Mousa, A. S.; Han, X.; Adstamongkonkul, P.; Popović, Z.; Huang, P.; Bawendi, M. G.; Boucher, Y.; Jain, R. K. Angiotensin inhibition enhances drug delivery and potentiates chemotherapy by decompressing tumour blood vessels. *Nat. Commun.* **2013**, *4*, 2516.

[109] Kramer, I. J.; Sargent, E. H. The Architecture of Colloidal Quantum Dot Solar Cells: Materials to Devices. *Chem. Rev.* **2014**, *114*, 863–882.

[110] Chuang, C.-H. M.; Brown, P. R.; Bulović, V.; Bawendi, M. G. Improved performance and stability in quantum dot solar cells through band alignment engineering. *Nature Mater.* **2014**, *13*, 796–801.

[111] Semonin, O. E.; Johnson, J. C.; Luther, J. M.; Midgett, A. G.; Nozik, A. J.; Beard, M. C. Absolute Photoluminescence Quantum Yields of IR-26 Dye, PbS, and PbSe Quantum Dots. *J. Phys. Chem. Lett.* **2010**, *1*, 2445–2450.

[112] Sallen, G.; Tribu, A.; Aichele, T.; André, R.; Besombes, L.; Bougerol, C.; Richard, M.; Tatarenko, S.; Kheng, K.; Poizat, J.-Ph. Subnanosecond Spectral Diffusion Measurement using Photon Correlation. *Nature Photon.* **2010**, *4*, 696–699.

[113] Peterson, J. J.; Krauss, T. D. Fluorescence Spectroscopy of Single Lead Sulfide Quantum Dots. *Nano Lett.* **2006**, *6*, 510–514.

[114] Rosenberg, D.; Kerman, A. J.; Molnar, R. J.; Dauler, E. A. High-speed and high-efficiency superconducting nanowire single photon detector array. *Opt. Express* **2013**, *21*, 1440–1447.

[115] Bludau, W.; Onton, A.; Heinke, W. Temperature dependence of the band gap of silicon. *J. Appl. Phys.* **1974**, *45*, 1846–1848.

[116] Kamplain, J.; Zhu, Z. Semiconductor nanocrystals and methods of preparation. US Patent PCT/US2011/063919, 2011.

[117] Frantsuzov, P.; Kuno, M.; Jankó, B.; Marcus, R. A. Universal emission intermittency in quantum dots, nanorods and nanowires. *Nature Phys.* **2008**, *4*, 519–522.

[118] Gómez, D. E.; van Embden, J.; Mulvaney, P.; Fernée, M. J.; Rubinsztein-Dunlop, H. Exciton-Trion Transitions in Single CdSe–CdS Core–Shell Nanocrystals. *ACS Nano* **2009**, *3*, 2281–2287.

[119] Spinicelli, P.; Buil, S.; Quélin, X.; Mahler, B.; Dubertret, B.; Hermier, J.-P. Bright and Grey States in CdSe-CdS Nanocrystals Exhibiting Strongly Reduced Blinking. *Phys. Rev. Lett.* **2009**, *102*, 136801.

[120] Park, Y.-S.; Bae, W. K.; Padilha, L. A.; Pietryga, J. M.; Klimov, V. I. Effect of the Core/Shell Interface on Auger Recombination Evaluated by Single-Quantum-Dot Spectroscopy. *Nano Lett.* **2014**, *14*, 396–402.

[121] Schaller, R. D.; Pietryga, J. M.; Klimov, V. I. Carrier Multiplication in InAs Nanocrystal Quantum Dots with an Onset Defined by the Energy Conservation Limit. *Nano Lett.* **2007**, *7*, 3469–3476.

[122] Ben-Lulu, M.; Mocatta, D.; Bonn, M.; Banin, U.; Ruhman, S. On the Absence of Detectable Carrier Multiplication in a Transient Absorption Study of InAs/CdSe/ZnSe Core/Shell1/Shell2 Quantum Dots. *Nano Lett.* **2008**, *8*, 1207–1211.

[123] Zhao, J.; Chen, O.; Strasfeld, D. B.; Bawendi, M. G. Biexciton Quantum Yield Heterogeneities in Single CdSe (CdS) Core (Shell) Nanocrystals and Its Correlation to Exciton Blinking. *Nano Lett.* **2012**, *12*, 4477–4483.

[124] Mangum, B. D.; Wang, F.; Dennis, A. M.; Gao, Y.; Gao, X.; Hollingsworth, J. A.; Htoon, H. Competition between Auger Recombination and Hot-Carrier Trapping in PL Intensity Fluctuations of Type II Nanocrystals. *Small* **2014**, *10*, 2892–2901.

[125] Yu, P.; Beard, M. C.; Ellingson, R. J.; Ferrere, S.; Curtis, C.; Drexler, J.; Luiszer, F.; Nozik, A. J. Absorption Cross-Section and Related Optical Properties of Colloidal InAs Quantum Dots. *J. Phys. Chem. B* **2005**, *109*, 7084–7087.

[126] Fernée, M. J.; Sinito, C.; Louyer, Y.; Tamarat, P.; Lounis, B. The ultimate limit to the emission linewidth of single nanocrystals. *Nanotechnology* **2013**, *24*, 465703.

[127] Fernée, M. J.; Sinito, C.; Louyer, Y.; Potzner, C.; Nguyen, T.-L.; Mulvaney, P.; Tamarat, P.; Lounis, B. Magneto-optical properties of trions in non-blinking charged nanocrystals reveal an acoustic phonon bottleneck. *Nat. Commun.* **2012**, *3*, 1287.

[128] Nirmal, M.; Murray, C. B.; Bawendi, M. G. Fluorescence-line narrowing in CdSe quantum dots: Surface localization of the photogenerated exciton. *Phys. Rev. B* **1994**, *50*, 2293–2300.

[129] Nirmal, M.; Norris, D. J.; Kuno, M.; Bawendi, M. G.; Efros, Al. L.; Rosen, M. Observation of the "Dark Exciton" in CdSe Quantum Dots. *Phys. Rev. Lett.* **1995**, *75*, 3728–3731.

[130] Liu, H.; Guyot-Sionnest, P. Photoluminescence Lifetime of Lead Selenide Colloidal Quantum Dots. *J. Phys. Chem. C* **2010**, *114*, 14860–14863.

[131] Fernée, M. J.; Louyer, Y.; Tamarat, P.; Lounis, B. Comment on "Spin-Flip Limited Exciton Dephasing in CdSe/ZnS Colloidal Quantum Dots". *Phys. Rev. Lett.* **2012**, *109*, 229701.

[132] Sinito, C.; Fernée, M. J.; Goupalov, S. V.; Mulvaney, P.; Tamarat, P.; Lounis, B. Tailoring the Exciton Fine Structure of Cadmium Selenide Nanocrystals with Shape Anisotropy and Magnetic Field. *ACS Nano* **2014**, *8*, 11651–11656.

[133] Bruns, O. T.; Bischof, T. S.; Harris, D. K.; Shi, Y.; Riedemann, L.; Reiberger, T.; Bartelt, A.; Jaworski, F. B.; Franke, D.; Wilson, M. W.; Chen, O.; Wei, H.; Hwang, G. W.; Montana, D.; Coropceanu, I.; Kloepper, J.; Heeren, J.; Fukumura, D.; Jensen, K. F.; Jain, R. K.; Bawendi, M. G. Next generation *in vivo* optical imaging with short-wave infrared quantum dots. *Submitted*

[134] Cerullo, G.; De Silvestri, S.; Banin, U. Size-dependent dynamics of coherent acoustic phonons in nanocrystal quantum dots. *Phys. Rev. B* **1999**, *60*, 1928–1932.

[135] Robel, I.; Shabaev, A.; Lee, D. C.; Schaller, R. D.; Pietryga, J. M.; Crooker, S. A.; L. Efros, A.; Klimov, V. I. Temperature and Magnetic-Field Dependence of Radiative Decay in Colloidal Germanium Quantum Dots. *Nano Lett.* **2015**, *15*, 2685–2692.

[136] Klimov, V. I.; Mikhailovsky, A. A.; Xu, S.; Malko, A.; Hollingsworth, J. A.; Leatherdale, C. A.; Eisler, H.-J.; Bawendi, M. G. Optical Gain and Stimulated Emission in Nanocrystal Quantum Dots. *Science* **2000**, *290*, 314–317.

[137] Klimov, V. I.; Mikhailovsky, A. A.; McBranch, D. W.; Leatherdale, C. A.; Bawendi, M. G. Quantization of Multiparticle Auger Rates in Semiconductor Quantum Dots. *Science* **2000**, *287*, 1011–1013.

[138] Klimov, V. I.; Ivanov, S. A.; Nanda, J.; Achermann, M.; Bezel, I.; McGuire, J. A.; Piryatinski, A. Single-exciton optical gain in semiconductor nanocrystals. *Nature* **2007**, *447*, 441–446.

[139] Dang, C.; Lee, J.; Breen, C.; Steckel, J. S.; Coe-Sullivan, S.; Nurmikko, A. Red, green and blue lasing enabled by single-exciton gain in colloidal quantum dot films. *Nature Nanotech.* **2012**, *7*, 335–339.

[140] Cihan, A. F.; Kelestemur, Y.; Guzelturk, B.; Yerli, O.; Kurum, U.; Yaglioglu, H. G.; Elmali, A.; Demir, H. V. Attractive versus Repulsive Excitonic Interactions of Colloidal Quantum Dots Control Blue- to Red-Shifting (and Non-shifting) Amplified Spontaneous Emission. *J. Phys. Chem. Lett.* **2013**, *4*, 4146–4152.

[141] Kelestemur, Y.; Cihan, A. F.; Guzelturk, B.; Demir, H. V. Type-tunable amplified spontaneous emission from core-seeded CdSe/CdS nanorods controlled by exciton-exciton interaction. *Nanoscale* **2014**, *6*, 8509–8514.

[142] She, C.; Fedin, I.; Dolzhnikov, D. S.; Demortière, A.; Schaller, R. D.; Pelton, M.; Talapin, D. V. Low-Threshold Stimulated Emission Using Colloidal Quantum Wells. *Nano Lett.* **2014**, *14*, 2772–2777.

[143] Müller, J.; Lupton, J. M.; Rogach, A. L.; Feldmann, J.; Talapin, D. V.; Weller, H. Monitoring Surface Charge Movement in Single Elongated Semiconductor Nanocrystals. *Phys. Rev. Lett.* **2004**, *93*, 167402.

[144] Müller, J.; Lupton, J. M.; Rogach, A. L.; Feldmann, J.; Talapin, D. V.; Weller, H. Air-induced fluorescence bursts from single semiconductor nanocrystals. *Appl. Phys. Lett.* **2004**, *85*, 381–383.

[145] Zhao, J.; Nair, G.; Fisher, B. R.; Bawendi, M. G. Challenge to the Charging Model of Semiconductor-Nanocrystal Fluorescence Intermittency from Off-State Quantum Yields and Multiexciton Blinking. *Phys. Rev. Lett.* **2010**, *104*, 157403.

[146] Louyer, Y.; Biadala, L.; Tamarat, Ph.; Lounis, B. Spectroscopy of neutral and charged exciton states in single CdSe/ZnS nanocrystals. *Appl. Phys. Lett.* **2010**, *96*, 203111.

[147] Javaux, C.; Mahler, B.; Dubertret, B.; Shabaev, A.; Rodina, A.; Efros, Al. L.; Yakovlev, D.; Liu, F.; Bayer, M.; Camps, G.; Biadala, L.; Buil, S.; Quelin, X.; Hermier, J.-P. Thermal activation of non-radiative Auger recombination in charged colloidal nanocrystals. *Nature Nanotech.* **2013**, *8*, 206–212.

[148] Park, Y.-S.; Bae, W. K.; Pietryga, J. M.; Klimov, V. I. Auger Recombination of Biexcitons and Negative and Positive Trions in Individual Quantum Dots. *ACS Nano* **2014**, *8*, 7288–7296.

[149] Canneson, D.; Mallek-Zouari, I.; Buil, S.; Quélin, X.; Javaux, C.; Dubertret, B.; Hermier, J.-P. Enhancing the fluorescence of individual thick shell CdSe/CdS nanocrystals by coupling to gold structures. *New J. Phys.* **2012**, *14*, 063035.

[150] Fisher, B. R. Time resolved fluorescence of CdSe nanocrystals using single molecule spectroscopy. Ph.D. thesis, Massachusetts Institute of Technology, 2005.

[151] Fisher, B.; Caruge, J. M.; Zehnder, D.; Bawendi, M. Room-Temperature Ordered Photon Emission from Multiexciton States in Single CdSe Core-Shell Nanocrystals. *Phys. Rev. Lett.* **2005**, *94*, 087403.

[152] Canneson, D.; Biadala, L.; Buil, S.; Quélin, X.; Javaux, C.; Dubertret, B.; Hermier, J.-P. Blinking suppression and biexcitonic emission in thick-shell CdSe/CdS nanocrystals at cryogenic temperature. *Phys. Rev. B* **2014**, *89*, 035303.

[153] Ithurria, S.; Tessier, M. D.; Mahler, B.; Lobo, R. P. S. M.; Dubertret, B.; Efros, Al. L. Colloidal nanoplatelets with two-dimensional electronic structure. *Nat. Mater.* **2011**, *10*, 936–941.

[154] Ithurria, S.; Talapin, D. V. Colloidal Atomic Layer Deposition (c-ALD) using Self-Limiting Reactions at Nanocrystal Surface Coupled to Phase Transfer between Polar and Nonpolar Media. *J. Am. Chem. Soc.* **2012**, *134*, 18585–18590.

[155] Stone, K. W.; Gundogdu, K.; Turner, D. B.; Li, X.; Cundiff, S. T.; Nelson, K. A. Two-Quantum 2D FT Electronic Spectroscopy of Biexcitons in GaAs Quantum Wells. *Science* **2009**, *324*, 1169–1173.

[156] Turner, D. B.; Nelson, K. A. Coherent measurements of high-order electronic correlations in quantum wells. *Nature* **2010**, *466*, 1089–1092.

[157] Achtstein, A. W.; Schliwa, A.; Prudnikau, A.; Hardzei, M.; Artemyev, M. V.; Thomsen, C.; Woggon, U. Electronic Structure and Exciton–Phonon Interaction in Two-Dimensional Colloidal CdSe Nanosheets. *Nano Lett.* **2012**, *12*, 3151–3157.

[158] Kunneman, L. T.; Schins, J. M.; Pedetti, S.; Heuclin, H.; Grozema, F. C.; Houtepen, A. J.; Dubertret, B.; Siebbeles, L. D. A. Nature and Decay Pathways of Photoexcited States in CdSe and CdSe/CdS Nanoplatelets. *Nano Lett.* **2014**, *14*, 7039–7045.

[159] Coropceanu, I.; Bawendi, M. G. Core/Shell Quantum Dot Based Luminescent Solar Concentrators with Reduced Reabsorption and Enhanced Efficiency. *Nano Lett.* **2014**, *14*, 4097–4101.

[160] Hong, G.; Robinson, J. T.; Zhang, Y.; Diao, S.; Antaris, A. L.; Wang, Q.; Dai, H. In?Vivo Fluorescence Imaging with $Ag_2S$ Quantum Dots in the Second Near-Infrared Region. *Angew. Chem. Int. Ed.* **2012**, *51*, 9818–9821.

[161] Zhang, Y.; Hong, G.; Zhang, Y.; Chen, G.; Li, F.; Dai, H.; Wang, Q. $Ag_2S$ Quantum Dot: A Bright and Biocompatible Fluorescent Nanoprobe in the Second Near-Infrared Window. *ACS Nano* **2012**, *6*, 3695–3702.

[162] Zhang, Y.; Liu, Y.; Li, C.; Chen, X.; Wang, Q. Controlled Synthesis of $Ag_2S$ Quantum Dots and Experimental Determination of the Exciton Bohr Radius. *J. Phys. Chem. C* **2014**, *118*, 4918–4923.

[163] Yarema, M.; Pichler, S.; Sytnyk, M.; Seyrkammer, R.; Lechner, R. T.; Fritz-Popovski, G.; Jarzab, D.; Szendrei, K.; Resel, R.; Korovyanko, O.; Loi, M. A.; Paris, O.; Hesser, G.; Heiss, W. Infrared Emitting and Photoconducting Colloidal Silver Chalcogenide Nanocrystal Quantum Dots from a Silylamide-Promoted Synthesis. *ACS Nano* **2011**, *5*, 3758–3765.

[164] Gu, Y.-P.; Cui, R.; Zhang, Z.-L.; Xie, Z.-X.; Pang, D.-W. Ultrasmall Near-Infrared $Ag_2Se$ Quantum Dots with Tunable Fluorescence for *in Vivo* Imaging. *J. Am. Chem. Soc.* **2012**, *134*, 79–82.

[165] Dong, B.; Li, C.; Chen, G.; Zhang, Y.; Zhang, Y.; Deng, M.; Wang, Q. Facile Synthesis of Highly Photoluminescent $Ag_2Se$ Quantum Dots as a New Fluorescent Probe in the Second Near-Infrared Window for in Vivo Imaging. *Chem. Mater.* **2013**, *25*, 2503–2509.

[166] Zhu, C.-N.; Jiang, P.; Zhang, Z.-L.; Zhu, D.-L.; Tian, Z.-Q.; Pang, D.-W. $Ag_2Se$ Quantum Dots with Tunable Emission in the Second Near-Infrared Window. *ACS Appl. Mater. Interfaces* **2013**, *5*, 1186–1189.

[167] Dresselhaus, M.; Dresselhaus, G.; Saito, R. Physics of carbon nanotubes. *Carbon* **1995**, *33*, 883–891.

[168] Welsher, K.; Liu, Z.; Sherlock, S. P.; Robinson, J. T.; Chen, Z.; Daranciang, D.; Dai, H. A route to brightly fluorescent carbon nanotubes for near-infrared imaging in mice. *Nature Nanotech.* **2009**, *4*, 773–780.

[169] Welsher, K.; Sherlock, S. P.; Dai, H. Deep-tissue anatomical imaging of mice using carbon nanotube fluorophores in the second near-infrared window. *Proc. Nat. Acad. Sci. U.S.A.* **2011**, *108*, 8943–8948.

[170] Yi, H.; Ghosh, D.; Ham, M.-H.; Qi, J.; Barone, P. W.; Strano, M. S.; Belcher, A. M. M13 Phage-Functionalized Single-Walled Carbon Nanotubes As Nanoprobes for Second Near-Infrared Window Fluorescence Imaging of Targeted Tumors. *Nano Lett.* **2012**, *12*, 1176–1183.

[171] Hong, G.; Lee, J. C.; Robinson, J. T.; Raaz, U.; Xie, L.; Huang, N. F.; Cooke, J. P.; Dai, H. Multifunctional *in vivo* vascular imaging using near-infrared II fluorescence. *Nat. Med.* **2012**, *18*, 1841–1846.

[172] Hong, G.; Diao, S.; Chang, J.; Antaris, A. L.; Chen, C.; Zhang, B.; Zhao, S.; Atochin, D. N.; Huang, P. L.; Andreasson, K. I.; Kuo, C. J.; Dai, H. Through-skull fluorescence imaging of the brain in a new near-infrared window. *Nature Photon.* **2014**, *8*, 723–730.

[173] Hong, G.; Zou, Y.; Antaris, A. L.; Diao, S.; Wu, D.; Cheng, K.; Zhang, X.; Chen, C.; Liu, B.; He, Y.; Wu, J. Z.; Yuan, J.; Zhang, B.; Tao, Z.; Fukunaga, C.; Dai, H. Ultrafast fluorescence imaging *in vivo* with conjugated polymer fluorophores in the second near-infrared window. *Nat. Commun.* **2014**, *5*, 4206.

[174] Harris, D. K.; Allen, P. M.; Han, H.-S.; Walker, B. J.; Lee, J.; Bawendi, M. G. Synthesis of Cadmium Arsenide Quantum Dots Luminescent in the Infrared. *J. Am. Chem. Soc.* **2011**, *133*, 4676–4679.

[175] Kovalenko, M. V.; Kaufmann, E.; Pachinger, D.; Roither, J.; Huber, M.; Stangl, J.; Hesser, G.; Schäffler, F.; Heiss, W. Colloidal HgTe Nanocrystals with Widely Tunable Narrow Band Gap Energies: From Telecommunications to Molecular Vibrations. *J. Am. Chem. Soc.* **2006**, *128*, 3516–3517.

[176] Keuleyan, S.; Lhuillier, E.; Guyot-Sionnest, P. Synthesis of Colloidal HgTe Quantum Dots for Narrow Mid-IR Emission and Detection. *J. Am. Chem. Soc.* **2011**, *133*, 16422–16424.

[177] Keuleyan, S.; Kohler, J.; Guyot-Sionnest, P. Photoluminescence of Mid-Infrared HgTe Colloidal Quantum Dots. *J. Phys. Chem. C* **2014**, *118*, 2749–2753.

[178] Kopainsky, B.; Qiu, P.; Kaiser, W.; Sens, B.; Drexhage, K. H. Lifetime, photostability, and chemical structure of IR heptamethine cyanine dyes absorbing beyond 1 µm. *Appl. Phys. B* **1982**, *29*, 15–18.

[179] Hatami, S.; Wurth, C.; Kaiser, M.; Leubner, S.; Gabriel, S.; Bahrig, L.; Lesnyak, V.; Pauli, J.; Gaponik, N.; Eychmüller, A.; Resch-Genger, U. Absolute photoluminescence quantum yields of IR26 and IR-emissive $Cd_{1-x}Hg_xTe$ and PbS quantum dots – method- and material-inherent challenges. *Nanoscale* **2015**, *7*, 133–143.

[180] Tao, Z.; Hong, G.; Shinji, C.; Chen, C.; Diao, S.; Antaris, A. L.; Zhang, B.; Zou, Y.; Dai, H. Biological Imaging Using Nanoparticles of Small Organic Molecules with Fluorescence Emission at Wavelengths Longer than 1000 nm. *Angew. Chem. Int. Ed.* **2013**, *52*, 13002–13006.

[181] Wise, F. W. Lead Salt Quantum Dots: the Limit of Strong Quantum Confinement. *Acc. Chem. Res.* **2000**, *33*, 773–780.

[182] Moreels, I.; Lambert, K.; Smeets, D.; De Muynck, D.; Nollet, T.; Martins, J. C.; Vanhaecke, F.; Vantomme, A.; Delerue, C.; Allan, G.; Hens, Z. Size-Dependent Optical Properties of Colloidal PbS Quantum Dots. *ACS Nano* **2009**, *3*, 3023–3030.

[183] Pietryga, J. M.; Schaller, R. D.; Werder, D.; Stewart, M. H.; Klimov, V. I.; Hollingsworth, J. A. Pushing the Band Gap Envelope: Mid-Infrared Emitting Colloidal PbSe Quantum Dots. *J. Am. Chem. Soc.* **2004**, *126*, 11752–11753.

[184] Murphy, J. E.; Beard, M. C.; Norman, A. G.; Ahrenkiel, S. P.; Johnson, J. C.; Yu, P.; Mi?i?, O. I.; Ellingson, R. J.; Nozik, A. J. PbTe Colloidal Nanocrystals: Synthesis, Characterization, and Multiple Exciton Generation. *J. Am. Chem. Soc.* **2006**, *128*, 3241–3247.

[185] Kumar, G. A.; Chen, C. W.; Ballato, J.; Riman, R. E. Optical Characterization of Infrared Emitting Rare-Earth-Doped Fluoride Nanocrystals and Their Transparent Nanocomposites. *Chem. Mater.* **2007**, *19*, 1523–1528.

[186] Naczynski, D. J.; Tan, M. C.; Zevon, M.; Wall, B.; Kohl, J.; Kulesa, A.; Chen, S.; Roth, C. M.; Riman, R. E.; Moghe, P. V. Rare-earth-doped biological composites as *in vivo* shortwave infrared reporters. *Nat. Commun.* **2013**, *4*, 2199.

[187] Gargas, D. J.; Chan, E. M.; Ostrowski, A. D.; Aloni, S.; Altoe, M. V. P.; Barnard, E. S.; Sanii, B.; Urban, J. J.; Milliron, D. J.; Cohen, B. E.; Schuck, P. J. Engineering bright sub-10-nm upconverting nanocrystals for single-molecule imaging. *Nature Nanotech.* **2014**, *9*, 300–305.

[188] Chan, E. M.; Levy, E. S.; Cohen, B. E. Rationally Designed Energy Transfer in Upconverting Nanoparticles. *Adv. Mater.* **2015**,

[189] Chan, E. M. Combinatorial approaches for developing upconverting nanomaterials: high-throughput screening, modeling, and applications. *Chem. Soc. Rev.* **2015**, *44*, 1653–1679.

[190] Mashiko, S.; Suzuki, N.; Koga, S.; Nakano, M.; Goto, T.; Ashino, T.; Mizumoto, I.; Inaba, H. Measurement of rate constants for quenching singlet oxygen with a Cypridina luciferin analog (2-methyl-6-[p-methoxyphenyl]-3,7-dihydroimidazo[1,2-a]pyrazin-3-one) and sodium azide. *J. Biolumin. Chemilumin.* **1991**, *6*, 69–72.

[191] Stürzl, N.; Lebedkin, S.; Kappes, M. M. Revisiting the Laser Dye Styryl-13 As a Reference Near-Infrared Fluorophore: Implications for the Photoluminescence Quantum Yields of Semiconducting Single-Walled Carbon Nanotubes. *J. Phys. Chem. A* **2009**, *113*, 10238–10240.

[192] Nakano, M. Detection of Active Oxygen Species in Biological Systems. *Cell. Mol. Neurobiol.* **1998**, *18*, 565–579.

[193] Seilmeier, A.; Kopainsky, B.; Kaiser, W. Infrared fluorescence and laser action of fast mode-locking dyes. *Appl. Phys.* **1980**, *22*, 355–359.

[194] Casalboni, M.; Matteis, F. D.; Prosposito, P.; Quatela, A.; Sarcinelli, F. Fluorescence efficiency of four infrared polymethine dyes. *Chem. Phys. Lett.* **2003**, *373*, 372–378.

[195] Lim, Y. T.; Kim, S.; Nakayama, A.; Stott, N. E.; Bawendi, M. G.; Frangioni, J. V. Selection of quantum dot wavelengths for biomedical assays and imaging. *Mol. Imaging* **2003**, *2*, 50–64.

[196] Hong, G.; Diao, S.; Antaris, A. L.; Dai, H. Carbon Nanomaterials for Biological Imaging and Nanomedicinal Therapy. *Chem. Rev.* ASAP.

[197] Cao, J.; Zhu, H.; Deng, D.; Xue, B.; Tang, L.; Mahounga, D.; Qian, Z.; Gu, Y. *In vivo* NIR imaging with PbS quantum dots entrapped in biodegradable micelles. *J. Biomed. Mater. Res. A* **2012**, *100A*, 958–968.

[198] Tsukasaki, Y.; Komatsuzaki, A.; Mori, Y.; Ma, Q.; Yoshioka, Y.; Jin, T. A short-wavelength infrared emitting multimodal probe for non-invasive visualization of phagocyte cell migration in living mice. *Chem. Commun.* **2014**, *50*, 14356–14359.

[199] Tsukasaki, Y.; Morimatsu, M.; Nishimura, G.; Sakata, T.; Yasuda, H.; Komatsuzaki, A.; Watanabe, T. M.; Jin, T. Synthesis and optical properties of emission-tunable PbS/CdS core-shell quantum dots for in vivo fluorescence imaging in the second near-infrared window. *RSC Adv.* **2014**, *4*, 41164–41171.

[200] Bawendi, M. G.; Harris, D. K.; Bruns, O. T.; Bischof, T. S. Short-wavelength infrared (SWIR) fluorescence in vivo and intravital imaging with semiconductor nanocrystals. 2015; WO Patent App. PCT/US2014/034988.

[201] Leatherdale, C. A. Photophysics of cadmium selenide quantum dot solids. Ph.D. thesis, Massachusetts Institute of Technology, 2000.

[202] Leatherdale, C. A.; Woo, W.-K.; Mikulec, F. V.; Bawendi, M. G. On the Absorption Cross Section of CdSe Nanocrystal Quantum Dots. *J. Phys. Chem. B* **2002**, *106*, 7619–7622.

[203] Hopt, A.; Neher, E. Highly Nonlinear Photodamage in Two-Photon Fluorescence Microscopy. *Biophys. J.* **2001**, *80*, 2029–2036.

[204] Helmchen, F.; Denk, W. Deep tissue two-photon microscopy. *Nat. Methods* **2005**, *2*, 932–940.

[205] Horton, N. G.; Wang, K.; Kobat, D.; Clark, C. G.; Wise, F. W.; Schaffer, C. B.; Xu, C. *In vivo* three-photon microscopy of subcortical structures within an intact mouse brain. *Nature Photon.* **2013**, *7*, 205–209.

[206] *American National Standard for Safe Use of Lasers (ANSI Z136.1–2007)*; Laser Institute of America, 2007.

[207] Rolling Shutters. `http://jasmcole.com/2014/10/12/rolling-shutters/`, Accessed 2015-04-30.

[208] Bruns, O. T.; Ittrich, H.; Peldschus, K.; Kaul, M. G.; Tromsdorf, U. I.; Lauterwasser, J.; Nikolic, M. S.; Mollwitz, B.; Merkel, M.; Bigall, N. C.; Sapra, S.; Reimer, R.; Hohenberg, H.; Weller, H.; Eychmüller, A.; Adam, G.; Beisiegel, U.; Heeren, J. Real-time magnetic resonance imaging and quantification of lipoprotein metabolism *in vivo* using nanocrystals. *Nature Nanotech.* **2009**, *4*, 193–201.

[209] Bartelt, A.; Bruns, O. T.; Reimer, R.; Hohenberg, H.; Ittrich, H.; Peldschus, K.; Kaul, M. G.; Tromsdorf, U. I.; Weller, H.; Waurisch, C.; Eychmüller, A.; Gordts, P. L. S. M.; Rinninger, F.; Bruegelmann, K.; Freund, B.; Nielsen, P.; Merkel, M.; Heeren, J. Brown adipose tissue activity controls triglyceride clearance. *Nat. Med.* **2011**, *17*, 200–205.

[210] Heeren, J.; Bruns, O. Nanocrystals, a New Tool to Study Lipoprotein Metabolism and Atherosclerosis. *Curr. Pharm. Biotechnol.* **2012**, *13*, 365–372.

[211] Fay, F.; Sanchez-Gaytan, B. L.; Cormode, D. P.; Skajaa, T.; Fisher, E. A.; Fayad, Z. A.; Mulder, W. J. M. Nanocrystal Core Lipoprotein Biomimetics for Imaging of Lipoproteins and Associated Diseases. *Curr. Cardiovasc. Imaging Rep.* **2013**, *6*, 45–54.

[212] Jung, C.; Kaul, M. G.; Bruns, O. T.; Dučić, T.; Freund, B.; Heine, M.; Reimer, R.; Meents, A.; Salmen, S. C.; Weller, H.; Nielsen, P.; Adam, G.; Heeren, J.; Ittrich, H. Intraperitoneal Injection Improves the Uptake of Nanoparticle-Labeled High-Density Lipoprotein to Atherosclerotic Plaques Compared With Intravenous Injection: A Multimodal Imaging Study in ApoE Knockout Mice. *Circ. Cardiovasc. Imaging* **2014**, *7*, 303–311.

[213] Knuth, N. D.; Remias, D. B.; Horowitz, J. F. Adding carbohydrate to a high-fat meal blunts postprandial lipemia in women and reduces meal-derived fatty acids in systemic circulation. *Appl. Physiol. Nutr. Metab.* **2008**, *33*, 315–325.

[214] Merkel, M.; Eckel, R. H.; Goldberg, I. J. Lipoprotein lipase: genetics, lipid uptake, and regulation. *J. Lipid Res.* **2002**, *43*, 1997–2006.

[215] Hultin, M.; Carneheim, C.; Rosenqvist, K.; Olivecrona, T. Intravenous lipid emulsions: removal mechanisms as compared to chylomicrons. *J. Lipid Res.* **1995**, *36*, 2174–2184.

[216] Varbo, A.; Benn, M.; Tybjærg-Hansen, A.; Jørgensen, A. B.; Frikke-Schmidt, R.; Nordestgaard, B. G. Remnant Cholesterol as a Causal Risk Factor for Ischemic Heart Disease. *J. Am. Coll. Cardiol.* **2013**, *61*, 427–436.

[217] Berbée, J. F. P.; Boon, M. R.; Khedoe, P. P. S. J.; Bartelt, A.; Schlein, C.; Worthmann, A.; Kooijman, S.; Hoeke, G.; Mol, I. M.; John, C.; Jung, C.; Vazirpanah, N.; Brouwers, L. P.; Gordts, P. L.; Esko, J. D.; Hiemstra, P. S.; Havekes, L. M.; Scheja, L.; Heeren, J.; Rensen, P. C. Brown fat activation reduces hypercholesterolaemia and protects from atherosclerosis development. *Nat. Commun.* **2015**, *6*, 6356.

[218] Kiourti, A.; Psathas, K. A.; Nikita, K. S. Implantable and ingestible medical devices with wireless telemetry functionalities: A review of current status and challenges. *Bioelectromagnetics* **2014**, *35*, 1–15.

[219] Ketterling, J.; Aristizabal, O. Prospective ECG-gated mouse cardiac imaging with a 34-MHz annular array transducer. *IEEE Trans. Ultrason. Ferroelectr. Freq. Control* **2009**, *56*, 1394–1404.

[220] Carmeliet, P.; Jain, R. K. Angiogenesis in cancer and other diseases. *Nature* **2000**, *407*, 249–257.

[221] Jain, R. K. Normalization of Tumor Vasculature: An Emerging Concept in Antiangiogenic Therapy. *Science* **2005**, *307*, 58–62.

[222] Kamoun, W. S.; Chae, S.-S.; Lacorre, D. A.; Tyrrell, J. A.; Mitre, M.; Gillissen, M. A.; Fukumura, D.; Jain, R. K.; Munn, L. L. Simultaneous measurement of RBC velocity, flux, hematocrit and shear rate in vascular networks. *Nat. Methods* **2010**, *7*, 655–660.

[223] Liu, G.; Chen, Z. Advances in Doppler OCT. *Chin. Opt. Lett.* **2013**, *11*, 011702.

[224] Leitgeb, R. A.; Werkmeister, R. M.; Blatter, C.; Schmetterer, L. Doppler Optical Coherence Tomography. *Prog. Retin. Eye Res.* **2014**, *41*, 26–43.

[225] Vakoc, B. J.; Lanning, R. M.; Tyrrell, J. A.; Padera, T. P.; Bartlett, L. A.; Stylianopoulos, T.; Munn, L. L.; Tearney, G. J.; Fukumura, D.; Jain, R. K.; Bouma, B. E. Three-dimensional microscopy of the tumor microenvironment in vivo using optical frequency domain imaging. *Nat. Med.* **2009**, *15*, 1219–1223.

[226] Rust, M. J.; Bates, M.; Zhuang, X. Sub-diffraction-limit imaging by stochastic optical reconstruction microscopy (STORM). *Nat. Methods* **2006**, *3*, 793–796.

[227] Adrian, R. J. Particle-Imaging Techniques for Experimental Fluid Mechanics. *Annu. Rev. Fluid Mech.* **1991**, *23*, 261–304.

[228] Adrian, R. Twenty years of particle image velocimetry. *Exp. Fluids* **2005**, *39*, 159–169.

[229] Schindelin, J.; Arganda-Carreras, I.; Frise, E.; Kaynig, V.; Longair, M.; Pietzsch, T.; Preibisch, S.; Rueden, C.; Saalfeld, S.; Schmid, B.; Tinevez, J.-Y.; White, D. J.; Hartenstein, V.; Eliceiri, K.; Tomancak, P.; Cardona, A. Fiji: an open-source platform for biological-image analysis. *Nat. Methods* **2012**, *9*, 676–682.

[230] Shi, Y.; Cheng, J. C.; Fox, R. O.; Olsen, M. G. Measurements of turbulence in a microscale multi-inlet vortex nanoprecipitation reactor. *J. Micromech. Microeng.* **2013**, *23*, 075005.

[231] Perazella, M. A. Current Status of Gadolinium Toxicity in Patients with Kidney Disease. *Clin. J. Am. Soc. Nephrol.* **2009**, *4*, 461–469.

[232] Wang, G.; Huang, T.; Murray, R. W.; Menard, L.; Nuzzo, R. G. Near-IR Luminescence of Monolayer-Protected Metal Clusters. *J. Am. Chem. Soc.* **2005**, *127*, 812–813.

[233] Negishi, Y.; Nobusada, K.; Tsukuda, T. Glutathione-Protected Gold Clusters Revisited: Bridging the Gap between Gold(I)–Thiolate Complexes and Thiolate-Protected Gold Nanocrystals. *J. Am. Chem. Soc.* **2005**, *127*, 5261–5270.

[234] Wu, Z.; Jin, R. On the Ligand's Role in the Fluorescence of Gold Nanoclusters. *Nano Lett.* **2010**, *10*, 2568–2573.

[235] Haruta, M.; Yamada, N.; Kobayashi, T.; Iijima, S. Gold catalysts prepared by coprecipitation for low-temperature oxidation of hydrogen and of carbon monoxide. *J. Catal.* **1989**, *115*, 301–309.

[236] Peyser, L. A.; Vinson, A. E.; Bartko, A. P.; Dickson, R. M. Photoactivated Fluorescence from Individual Silver Nanoclusters. *Science* **2001**, *291*, 103–106.

[237] Nair, G.; Bawendi, M. G. Carrier multiplication yields of CdSe and CdTe nanocrystals by transient photoluminescence spectroscopy. *Phys. Rev. B* **2007**, *76*, 081304.

[238] McGuire, J. A.; Joo, J.; Pietryga, J. M.; Schaller, R. D.; Klimov, V. I. New Aspects of Carrier Multiplication in Semiconductor Nanocrystals. *Acc. Chem. Res.* **2008**, *41*, 1810–1819.

[239] Nair, G.; Geyer, S. M.; Chang, L.-Y.; Bawendi, M. G. Carrier multiplication yields in PbS and PbSe nanocrystals measured by transient photoluminescence. *Phys. Rev. B* **2008**, *78*, 125325.

[240] Beard, M. C.; Midgett, A. G.; Hanna, M. C.; Luther, J. M.; Hughes, B. K.; Nozik, A. J. Comparing Multiple Exciton Generation in Quantum Dots To Impact Ionization in Bulk Semiconductors: Implications for Enhancement of Solar Energy Conversion. *Nano Lett.* **2010**, *10*, 3019–3027.

[241] Nair, G.; Chang, L.-Y.; Geyer, S. M.; Bawendi, M. G. Perspective on the Prospects of a Carrier Multiplication Nanocrystal Solar Cell. *Nano Lett.* **2011**, *11*, 2145–2151.

[242] Beard, M. C. Multiple Exciton Generation in Semiconductor Quantum Dots. *J. Phys. Chem. Lett.* **2011**, *2*, 1282–1288.

[243] Kambhampati, P. Hot Exciton Relaxation Dynamics in Semiconductor Quantum Dots: Radiationless Transitions on the Nanoscale. *J. Phys. Chem. C* **2011**, *115*, 22089–22109.

[244] Trinh, M. T.; Polak, L.; Schins, J. M.; Houtepen, A. J.; Vaxenburg, R.; Maikov, G. I.; Grinbom, G.; Midgett, A. G.; Luther, J. M.; Beard, M. C.; Nozik, A. J.; Bonn, M.; Lifshitz, E.; Siebbeles, L. D. A. Anomalous Independence of Multiple Exciton Generation on Different Group IV–VI Quantum Dot Architectures. *Nano Lett.* **2011**, *11*, 1623–1629.

[245] Stewart, J. T.; Padilha, L. A.; Qazilbash, M. M.; Pietryga, J. M.; Midgett, A. G.; Luther, J. M.; Beard, M. C.; Nozik, A. J.; Klimov, V. I. Comparison of Carrier Multiplication Yields in PbS and PbSe Nanocrystals: The Role of Competing Energy-Loss Processes. *Nano Lett.* **2012**, *12*, 622–628.

[246] Aerts, M.; Spoor, F. C. M.; Grozema, F. C.; Houtepen, A. J.; Schins, J. M.; Siebbeles, L. D. A. Cooling and Auger Recombination of Charges in PbSe Nanorods: Crossover from Cubic to Bimolecular Decay. *Nano Lett.* **2013**, *13*, 4380–4386.

[247] Beard, M. C.; Luther, J. M.; Semonin, O. E.; Nozik, A. J. Third Generation Photovoltaics based on Multiple Exciton Generation in Quantum Confined Semiconductors. *Acc. Chem. Res.* **2013**, *46*, 1252–1260.

[248] Midgett, A. G.; Luther, J. M.; Stewart, J. T.; Smith, D. K.; Padilha, L. A.; Klimov, V. I.; Nozik, A. J.; Beard, M. C. Size and Composition Dependent Multiple Exciton Generation Efficiency in PbS, PbSe, and $PbS_xSe_{1-x}$ Alloyed Quantum Dots. *Nano Lett.* **2013**, *13*, 3078–3085.

[249] Tielrooij, K. J.; Song, J. C. W.; Jensen, S. A.; Centeno, A.; Pesquera, A.; Zurutuza Elorza, A.; Bonn, M.; Levitov, L. S.; Koppens, F. H. L. Photoexcitation cascade and multiple hot-carrier generation in graphene. *Nature Phys.* **2013**, *9*, 248–252.

[250] Congreve, D. N.; Lee, J.; Thompson, N. J.; Hontz, E.; Yost, S. R.; Reusswig, P. D.; Bahlke, M. E.; Reineke, S.; Van Voorhis, T.; Baldo, M. A. External Quantum Efficiency Above 100 % in a Singlet-Exciton-Fission–Based Organic Photovoltaic Cell. *Science* **2013**, *340*, 334–337.

[251] Thompson, N. J.; Wilson, M. W. B.; Congreve, D. N.; Brown, P. R.; Scherer, J. M.; Bischof, T. S.; Wu, M.; Geva, N.; Welborn, M.; Voorhis, T. V.; Bulović, V.; Bawendi, M. G.; Baldo, M. Energy harvesting of non-emissive triplet excitons in tetracene by emissive PbS nanocrystals. *Nature Mater.* **2014**, *13*, 1039–1043.

[252] Semonin, O. E.; Luther, J. M.; Choi, S.; Chen, H.-Y.; Gao, J.; Nozik, A. J.; Beard, M. C. Peak External Photocurrent Quantum Efficiency Exceeding 100 % via MEG in a Quantum Dot Solar Cell. *Science* **2011**, *334*, 1530–1533.

[253] Nasilowski, M.; Spinicelli, P.; Patriarche, G.; Dubertret, B. Gradient CdSe/CdS Quantum Dots with Room Temperature Biexciton Unity Quantum Yield. *Nano Lett.* **2015**, *15*, 3953–3958.

[254] Sellmeier, Zur Erklärung der abnormen Farbenfolge im Spectrum einiger Substanzen. *Ann. Phys.* **1871**, *219*, 272–282.

[255] Polyanskiy, M. N. Refractive index database. `http://refractiveindex.info`, 2015; Accessed 2015-05-06.

[256] Hobel, M.; Ricka, J. Dead-time and afterpulsing correction in multiphoton timing with nonideal detectors. *Rev. Sci. Instrum.* **1994**, *65*, 2326–2336.

[257] Zhao, M.; Jin, L.; Chen, B.; Ding, Y.; Ma, H.; Chen, D. Afterpulsing and Its Correction in Fluorescence Correlation Spectroscopy Experiments. *Appl. Opt.* **2003**, *42*, 4031–4036.

[258] Fishburn, M. W. Fundamentals of CMOS Single-Photon Avalanche Diodes. Ph.D. thesis, Technische Universiteit Delft, 2012.

[259] Excelitas Technologies Corp., Single Photon Counting Modules (SPCM). `http://www.excelitas.com/Pages/Product/Single-Photon-Counting-Modules-SPCM.aspx`, Accessed 2015-05-08.

[260] *Photomultiplier Tubes: Basics and Applications*, 3rd ed.; Hamamatsu Photonics K. K., 2007.